PLASMONIC AND METAMATERIAL BASED TERAHERTZ DEVICES SUCH AS SENSORS AND MODULATORS

A

Thesis submitted

in Partial Fulfilment of the Requirements

for the Degree of

Doctor of Philosophy

by

KM Dhriti

Department of Physics
Indian Institute of Technology Guwahati
Guwahati - 781039, Assam, India
July 2022

Dedicated To My Beloved Parents.

Certificate

This is to certify that the thesis entitled "**Plasmonic and Metamaterial Based Terahertz Devices such as Sensors and Modulators**", submitted by **KM Dhriti** (176121006), a research scholar in the *Department of Physics, Indian Institute of Technology Guwahati*, for the award of the degree of **Doctor of Philosophy**, is a record of an original research work carried out by her under my supervision and guidance. The thesis has fulfilled all requirements as per the regulations of the institute and in my opinion has reached the standard needed for submission. The results embodied in this thesis have not been submitted to any other University or Institute for the award of any degree or diploma.

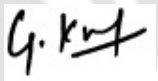

Date: July 21, 2022

Place: Guwahati

Dr. Gagan Kumar

Dept. of Physics,

Indian Institute of Technology Guwahati,

Guwahati - 781039, Assam, India.

Acknowledgement

First and foremost, I feel privileged to express my deepest and most sincere gratitude to my supervisor Dr. Gagan Kumar, for his excellent guidance throughout my research. His kindness, dedication, hard work and attention to detail has been a great inspiration to me. My heartfelt thanks to him for the unlimited support and patience he has shown me. I sincerely thank him for the effort he gave in scrutinizing every manuscript I presented to him and offering critical comments.

I am also very thankful to my doctoral committee members Dr. Kanhaiya Pandey, and Dr. Uday Narayan Maiti for sparing their precious time out of their busy schedule to evaluate my progress and enrich this work with their valuable suggestions and feedbacks. My sincere gratitude goes to Dr. Debabrata Sikdar for his constructive suggestions during the collaborative works.

I would also like to thank the Head of the Department and other faculty members for their kind help in carrying out this work. I am also grateful to all the members of the research and technical staff of the department, without whose help I could not have completed this thesis.

Thanks go out to all my labmates, batchmates, and seniors, Rakesh, Angana, Bhairov, Bhagwat, Ipsita, Madhurima, Pragya, Devender, Devabrat, Dr. Monika, Dr. Maidul, Dr. Jagan, and Nagendra. They have always been around to provide useful suggestions, companionship and created a fun-filled research environment. They all contributed directly or indirectly to this thesis. I want to also mention Dr. Jyotiprasad for his sincere help and guidance as a senior and his useful life advices. Apart from these people I would also like to thank Mr. Ashish for his help and support in my works. I have no words to express my thanks to some friends of our morning badminton group especially, Prajna, Juhi Di, and Sashmita Di. They helped me a lot in releasing the work pressure and channelizing it into a positive direction.

There are few people, whom I want to thank from bottom of my heart Reena,

Sourav, Sushmita, Sugandha, and Krishna, for their immense mental support through out my Ph.D. journey.

I take this opportunity to sincerely acknowledge the financial support from Ministry of Human Resources and Development (MHRD), Government of India during my Ph.D.

Last but not the least, I want to mention that I am highly grateful to my grandparents Mr. Laxman Maurya and Lt. Tetari Devi, for their sacrifices and love. I would like to thank my parents, Mr. Deovrat Maurya and Mrs. Meera Maurya, for their support and inspiration throughout my entire life. I would also like to thank my dearest siblings Pratibha, Smriti, Sanskriti and Rishi. I thank all the people who have been in direct or indirect association with me for my research work and have helped me in even the slightest possible manner.

(KM Dhriti)

Abstract

Despite considerable interest in the terahertz (THz) frequency range of the electromagnetic spectrum, the technological developments in terms of devices such as high-speed modulators and highly sensitive sensors are lagging, which are essential to cater to the need of the increasing population. The artificially designed plasmonics and metamaterial structures have the potential to realize such devices through careful arrangements of its constituents. They strongly interact with terahertz radiation and manipulate them in the desired fashion to realize photonic devices for THz applications, ultimately filling the technological gap in this region. In this thesis, the primary focus has been to investigate terahertz plasmonic and metamaterial structures for applications in highly sensitive sensors and high-speed modulators.

We propose a planar plasmonic terahertz waveguide comprising of one-dimensional array of periodically arranged subwavelength scale pyramidal corrugations. The waveguide supports highly confined modes along with the corrugated pattern. We investigate the refractive index sensor capability of the terahertz surface plasmon modes supported by the waveguide. We also analyze the dispersion properties and quality factors of the fundamental as well as higher-order modes of the waveguide and examine the significance in thin film sensing at terahertz frequencies.

In terahertz plasmonic waveguide, we also investigate near field coupling between modes of the waveguide comprising asymmetric resonators placed

in close proximity. The waveguide is designed to support surface plasmon polaritons (SPPs) at two distinct terahertz frequencies, which are near to each other. This is accomplished by carefully designing the unit cell comprising of two resonators with slightly different sizes. The resonators in the form of rectangular apertures are placed along the transverse direction in the near field regime. The role of near field coupling between resonators and their potential in modulating terahertz is comprehensively discussed.

We further investigate a double slot waveguide configuration to explore the actively tunable plasmon induced transparency (PIT) effect in the terahertz regime. One of the slot structures is filled with a dielectric material of certain refractive index which causes a slight shift in its resonance frequency as compared to the unfilled slot. The two slightly different frequencies results in PIT effect due to the destructive interference of the modes. The electric field profiles clearly indicate the emergence of the PIT effect. The observed transparency window is found to varying with the change in refractive index of the dielectric material, which promises an active and tunable control of the effect without changing the physical dimensions. Further, we examine the possibility of switching the transparency effect by incorporating a thin silicon layer between the grooves, by varying its conductivity.

The potential of metamaterials in building modulators has been widely explored in last few years. The broadband modulation has been a challenging task at terahertz frequencies. We address this limitation by designing a tunable broadband metamaterial absorber comprising frustum shaped dielectric (SiO_2) structures on top of a one-dimensional period array of graphene nanoribbons over the ultrathin metal-backed dielectric. The excitation of plasmons in graphene nanoribbons combined with resonance induced by the graphene-dielectric-metal cavity leads to nearly perfect broadband absorption for the TM polarized radiation. The modulation of the absorption

spectrum has been examined by changing graphene conductivity with the help of its Fermi energy. The figure of merit of our design indicates that it can be very promising to outperform some of the recently reported tunable metamaterial absorbers.

Contents

List of Figures

List of Tables

List of Publications

Journal Publications

1. **KM Dhriti**, et al. "Plasmon-induced transparency in an air–dielectric grooved parallel-plate terahertz waveguide." JOSA B 38.4 (2021): 1290-1296.
2. **KM Dhriti**, Maidul Islam, and Gagan Kumar. "Terahertz surface plasmon propagation in a near field coupled asymmetric resonators based planar waveguide." Journal of Optics 22.12 (2020): 125003.
3. Islam, Maidul, **KM Dhriti** et al. "Tunable control of electromagnetically induced transparency effect in a double slot terahertz waveguide." Optics Communications 483 (2021): 126632.
4. **KM Dhriti**, Amir Ahmad, and Gagan Kumar. "Planar plasmonic terahertz waveguide based upon one dimensional array of pyramidal corrugations and refractive index sensing." IEEE Photonics Journal 12.6 (2020): 1-10.
5. **KM Dhriti**, Ashish Kumar Chowdhary, Bhagwat Singh Chouhan, Debabrata Sikdar, and Gagan Kumar, "Tunable Terahertz Absorption Modulation in Graphene Nanoribbon-assisted Dielectric Metamaterial" (under review in *Journal of Physics D: Applied Physics*).
6. Islam, Maidul, Bhairov Kumar Bhowmik, **KM Dhriti**, Amir Ahmad, and Gagan Kumar "Thin Film Sensing characteristics in terahertz Metawaveguide structure" under preparation.

Conference Publications

1. Maidul, **KM Dhriti**, and Gagan Kumar, “Thin Film Sensing in Terahertz Plasmonic Waveguide”, WRAP 2017 conference proceedings in IEEE Xplroe.
2. **KM Dhriti** and Gagan Kumar “Refractive index sensor based upon a planar plasmonics terahertz waveguide” in Photonics 2018.
3. **KM Dhriti** and Gagan Kumar, “Study of resonant modes for sensing in a multimode planar plasmonic terahertz waveguide”, WRAP 2019 conference proceedings in IEEE Xplroe.
4. Bhargav, **KM Dhriti**, Angana and Gagan Kumar, “Refractive Index sensing using plasmonic mode in a periodically corrugated waveguide at terahertz frequencies”, WRAP 2019 conference proceedings in IEEE Xplroe.
5. Nidhi, P.C. Agarwal, **KM Dhriti**, Sukhdeep Kaur and T.S. Gill, “Self-Focusing of Quadruple Gaussian Laser Beam in Relativistic Plasma using Moment Theory Approach”, WRAP 2019 conference proceedings in IEEE Xplroe.
6. **KM Dhriti**, Maidul and Gagan Kumar, “Slow light effect in corrugated parallel plate terahertz plasmonic waveguide refractive index sensor” submitted in *WRAP 2022*.
7. Bhagwat Singh Chouhan, **KM Dhriti**, Ashish Kumar Chowdhary, Bhagwat Singh Chouhan, Debabrata Sikdar, and Gagan Kumar "Modulating broadband terahertz in a graphene assisted dielectric metamaterial" submitted in *WRAP 2022*.

1

Introduction

Contents

1.1 Terahertz Frequency Spectrum

The THz frequency range is referred to 300 GHz to the 10 THz frequency range, which lies between the microwave and infrared frequencies. The wavelength corresponding to this range lies between 100 μm to 1000 μm. It is additionally known as sub-millimeter, far infrared, and near millimeter waves. The THz range is undeveloped compared to other parts of the electromagnetic spectrum. Although the infrared and the microwave region has been studied quite extensively in literature, the THz region did not get the attention. Thus, despite lying in between those two well developed region of EM spectrum, THz region is still under development. Fig. 1.1 shows the

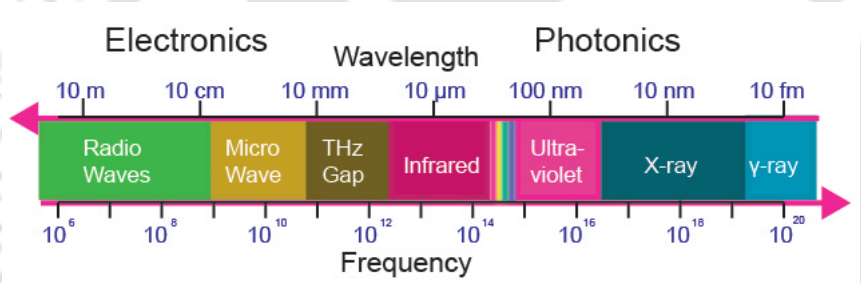

Figure 1.1: THz radiation in the electromagnetic spectrum.

electromagnetic spectrum and THz gap. Until as of late, the THz waves were only utilized in high-resolution spectroscopy and remote sensing applications [1–3]. Over the past decades, the THz frequency band has received much attention due to its unique properties suitable for several applications. Some of the essential properties and related applications of the THz radiation are given as:

• It has a longer wavelength than that of the visible and infrared radiation, providing better resolution in security monitoring. This property makes them appropriate for imaging and sensing applications [4].

• The THz waves are transparent to most dielectric materials such as plastic, paper, wood, and clothes, so they can be used to track the defects hidden inside bulky materials that are transparent to THz in several applications [5, 6].

• The THz radiation exhibits a nonionizing character because of its low energies; e.g.,

at 1 THz, the radiated signal has a photon energy of 4.1 meV. Thus, it can be advantageous in imaging the biological tissues in the distinction to the X-ray radiation [7].

• The energy of the rotational modes of numerous particles such as DNA, proteins, and explosives coincide with the energy of the THz frequencies, which let THz devices recognize materials due to their particular fingerprints with the THz range [8, 9].

• Many interesting materials have unique spectral absorption in the terahertz range. This material property is useful in the spectroscopy of materials using terahertz radiation which can be identified [10].

• Due to extraordinary water retention, THz waves can give data of hydration state and show the water condition of the tissue [11].

1.1.1 THz generation and detection

In the initial phase of the investigation in the THz region, the generation of THz was considered exceptionally difficult [12]. With the improvement of nano-engineering devices, it was conceivable to fabricate distinctive sorts of THz generation sources. These sources are either independently based on the microwave and the optical frequency generation techniques or combined with both methods [13]. A few THz radiation sources are commercially accessible and can be broadly partitioned into three categories: Electronic sources, Optical Sources, and Optoelectronic sources. A brief discussion about different kinds of sources are given below:

• The electronic sources are purely based on microwave techniques including vacuum electronic and solid-state electronic sources [14]. The working principle of vacuum electronic sources is based on the interaction between the electron beam and the electromagnetic fields, which include backward wave oscillator (BWOs) [15], synchrotrons [16], and traveling wave tubes (TWTs) [17]. These usually bulky sources radiate high power THz waves, and the radiated frequency is below 1 THz [18]. Solid-state electronic sources include diodes and multipliers, which use the principle of negative differential resistance to generate THz radiation and a diode chain to multiply the frequency in the THz range, respectively. The sources include Gunn diodes [19], high

frequency transistor [20], frequency multipliers [21], and resonant tunneling diodes (RTDs) [22].

• The optical sources are divided into lasers based and nonlinear crystal-based THz sources. The THz lasers had been constructed using the semiconductor materials inclusive of Germanium and Silicon and are primarily based on the population inversion underneath the conditions of optical pumping of the defects. The primary advantage of this type of laser is the ability to tune over various wavelengths by changing bandgap of the material, making it easier to generate different wavelengths from the same materials [23]. The generation of THz using nonlinear crystals, i.e., optical rectification, is one of the general techniques that use crystals with high secondary susceptibility to downconvert the optical power of lasers. In optical rectification technology, all possible different frequencies of spectrally broad pulses are generated with the aid of a femtosecond (fs) laser source [24].

• The optoelectronic sources are made by combining the microwave and the optical frequency generation techniques and based on the photoconductive principle in the semiconductor materials. It consists of a voltage biased antenna structure imprinted on the photoconductive semiconductor material wherein fs lasers are used as an excitation source for the antenna structure via way of means of generating an ultrafast converting current pulse. This rapidly changing current pulse stimulates the antenna to emit THz waves. Based on the excitation of the laser, these sources can be divided into two categories: Continuous wave (CW) THz source (narrowband): Photomixing Antenna (PMA), and Pulsed THz source (broadband): Photoconductive Antenna (PCA). The PCA system requires a single fs pulsed laser source to generate the THz radiation, whereas the PMA system requires two CW lasers having a slight difference in the operating optical frequency (the difference should be in the THz frequency range) [25].

For detecting THz frequency, several detectors are commercially available, which can measure both the broadband as well as the narrowband signals. These THz detectors have been broadly divided into coherent and incoherent detection techniques [26].

• The incoming THz signals are reduced to the frequency signal without losing the phase and amplitude information with the coherent detection system. The most commonly used coherent techniques are optoelectronic THz detectors and electro-optic (EO) sampling techniques. The optoelectronic systems, PMAs, and PCAs can also be used to detect the THz signal where the antenna is not biased, whereas a bias voltage is required in the source system. The incoming THz signals generate an electric field over the electrode gap area of the antenna. The photo carriers generated by the fs laser are accelerated and induce a photo-curing agent. The generated current can be further analyzed using the Fourier transform [26]. The electro-optic sampling technique relies on the principle of linear electro-optic (EO) effect conjointly referred to as the Pockel effect in a nonlinear crystal. The Pockel effect creates birefringence in a nonlinear crystal, which changes the polarization of the probe beam and determines the amplitude of the THz signals during the measurement [27].

• In the incoherent or direct THz detection, the incoming signal is targeted to the detector using focused optics such as lenses and mirrors. The detected signal is then amplified for additional processing [26]. Pyroelectric detectors, bolometers, and Golay cells are some wide used incoherent THz detectors.

1.1.2 Applications of THz radiations

As mentioned before, this frequency range has found a rapidly growing number of applications in different fields due to its unique properties beneficial for those fields. Some applications of THz radiations in various vital areas are as follows:

• *Pharmaceutical Applications*: Because of the unique response or spectral signature of various drugs or medicines at THz frequencies, it can be used for drug detection and characterization [28]. THz imaging and spectroscopy are more valuable in measuring medicate coating thickness [29], observing the coating preparation [30], measuring tablet density and hardness, disintegration profile [31], and chemical mapping [32] of drugs.

• *Security Applications*: THz can be exceptionally valuable for security applications due

to its longer wavelength than the visible and infrared radiation. THz can differentiate covered-up objects underneath numerous sorts of clothing because of the transparency of dielectric materials. It can be used in the scanning, surveillance, and detection of hidden objects. Besides, it has the potential to offer information of the hidden objects such as shape, size, and material used [33].

• *Biomedical Applications*: Since THz waves are inherently nonionizing due to their low photon energies, this can be advantageous for analyzing biological tissue. THz can penetrate several millimeters into tissues with low water content without being damaged. It can be used to detect typical and different types of cancer cells based on various percentages of water content. Therefore, terahertz imaging is utilized in the dental [10], the digestive system [34], recognizing illness or tumor [35], corpuscle analysis [36], and bone analysis [37].

• *Manufacturing Applications*: THz can be used to produce drugs, medical products, diapers, and polymers [38]. In the pharmaceutical and cosmetic industries, packaging materials are commonly made of paper, polyethylene, and plastics, fully transparent to THz. This allows the THz to spot the missing items within the packaging or quality checking of manufactured products.

• *Communication Applications*: The THz may deliver high-speed communication by combining a vast bandwidth with a high-speed spectrum. The attenuation of THz waves is exceptionally high because of the presence of water vapors in the atmosphere, which makes remote communication with THz waves a challenge. Depending on the link properties, THz communication can be used in local wireless networks in smart offices, wireless personal area networks in innovative home systems, near field communication such as download kiosks, wireless connections in data centers, and device communication [39–41].

Terahertz-based studies not only serve to see basic material parameters but are also necessary for the characterization of materials in numerous applications. Apart from the applications mentioned above, THz radiation can manipulate and control quantum

mechanical states in the matter. THz technology applied to the material can powerfully impact the subsequent areas of science: Quantum optics, Quantum-information science, Fundamental properties of semiconductor nanostructures, Fundamental limits of electronic devices, Coherent control and nonlinear THz spectroscopies, High THz electric field physics and nonlinear quantum dynamics, Subwavelength THz spectroscopy [41]. The advent of subwavelength THz spectroscopy impacted the entire field of optics and photonics by offering the possibility to control the light-matter interaction [42, 43] effectively. It deals with the generation, control, and use of light with structures having dimensions smaller than the wavelength of incident light. These artificially designed subwavelength structures enable interaction with the THz radiation leading to the realization of the many devices and ultimately filling the technological void in this regime. Due to their precise shape, geometry, size, and arrangement can manipulate electromagnetic waves by blocking, absorbing, and enhancing waves to achieve benefits in a practical scenario. These devices could be significant in variety of applications like sensors, optical filters, imaging, modulators and next generation photonic components.

1.2 Plasmonics

Plasmonics is an emerging area of science and technology where subwavelength structures can control the propagation of light. Because of the evanescent nature of plasmonics, it has been discovered that the electromagnetic field is confined within the subwavelength scale with minimal energy loss, resulting in a massive field enhancement. Such crucial properties of plasmonics introduced flourishing applications of plasmonic waveguides, photonic devices, sensing purposes, control switches, and modulators. Plasmonics deals with surface plasmon (SP) propagation and its applications.

1.2.1 Surface plasmon

Surface plasmons are waves that propagate along the surface of a conductor, usually a metal. These are essentially light waves that are confined on the surface because of their interaction with the free electrons of the conductor. In this interaction, the free

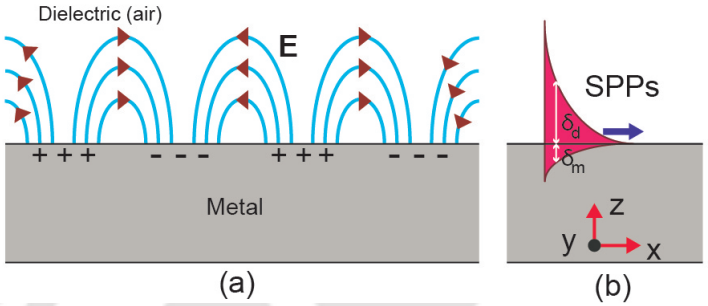

Figure 1.2: (a) Schematic illustration of electromagnetic wave and surface charges at the interface between the metal and the dielectric material (b) the local electric field component is enhanced near the surface and decay exponentially with distance in a direction normal to the interface.

electrons respond together by oscillating in resonance with the light wave. The resonant interaction among the surface charge oscillation and the electromagnetic field of light constitutes the SP and gives rise to its unique properties. The SPs used to concentrate light in subwavelength structures stem from metal's different (relative) permittivities and the surrounding non-conducting media. The concentration of light leads to an electric field enhancement, which helps manipulate light matter interactions and boost nonlinear phenomena. Properties of surface plasmons vary with the structure of metal's surface based on their interaction with light, which allows the development of new types of photonic devices. This can lead to miniaturized photonic circuits with length scales, much smaller than those currently achieved. Surface plasmons are getting explored for their potential in subwavelength optics, data storage, light generation, microscopy, and bio-photonics. Recent research on the surface plasmon at the THz frequency found that THz SPs exist at various configuration with different propagation behaviors. Depending upon propagation conditions and their dispersion relation, THz surface plasmons can exist on the bare metal surface [42], coated metal

surface [43], planar Goubau lines [44], textured metal surface [45], doped semiconductor or superconductors, and graphene surfaces [46,47]. Flat bare metal surfaces are the easiest and most common support for SPs. The propagation of the surface plasmon polaritons on the metal surface and its typical mode profile is shown in Fig. 1.2. SPs at the interface between a metal and a dielectric material have a combined electromagnetic wave and surface charge character, as shown in Fig 1.2(a). They are transverse magnetic in nature (H is in the y-direction), and the generation of surface charge requires an electric field normal to the surface. This combined character also leads to a field component perpendicular to the surface with maximum amplitude at the interface and decaying exponentially with distance away from it (see Fig. 1.2(b)). The field in this perpendicular direction is evanescent, reflecting the bound, non-radiative nature of SPs and preventing power from propagating away from the surface. In the dielectric medium above the metal, the decay length of the field, δ_d is of the order of half the wavelength of light involved [45], whereas the decay length into the metal, δ_m is determined by the skin depth. The dispersion relation of the surface plasmon polaritons on a single metal-dielectric interface can be obtained by solving Maxwell's equations in both the media and applying appropriate boundary conditions [48]. The dispersion relation of the surface Plasmon polaritons on a single metal-dielectric interface is given by [45]

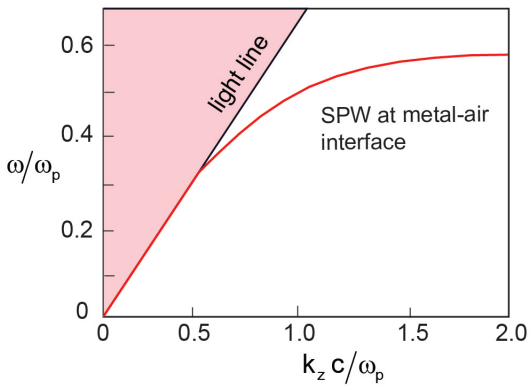

Figure 1.3: Dispersion for a Surface plasmon polaritons propagating at the metal-dielectric interface. The dotted line represents light line.

$$k_{sp} = \frac{\omega}{c}\sqrt{\frac{\epsilon_1\epsilon(\omega)}{\epsilon_1 + \epsilon(\omega)}}, \tag{1.1}$$

where, k_{sp} is the wave-vector of surface plasmon polaritons. ϵ_1 is the dielectric permittivity and $\epsilon(\omega)$ is the effective permittivity of metal. The dispersion curve for an SP mode shows a momentum mismatch between the light mode and SP modes, with the SP mode dispersion relation lying beyond the light line, i.e., it has higher momentum (k_{sp}) than a free space photon (k_0) of the same frequency (see Fig. 1.3). The distinction in momentum prevents the excitation of plasmons from being excited when light from the air hits the metal surface. This momentum mismatch should be compensated to couple light mode into a surface plasmon mode. The decay rates of wave amplitude in metal (α_m) and dielectric (α_1) can be written as

$$\alpha_1 = \frac{\omega\epsilon_1/c}{\sqrt{-[\epsilon_1 + \epsilon(\omega)]}} \tag{1.2}$$

$$\alpha_m = \frac{\omega/c}{\sqrt{-[\epsilon_1 + \epsilon(\omega)]/\epsilon(\omega)^2}} \tag{1.3}$$

At low frequency, ω varies linearly with k_{sp} as depicted in Fig 1.3. In this case, $\alpha_1 << \alpha_m$, which indicates that the wave is localised in a thin layer of thickness α_m^{-1} in the conductor. Though, it extends to larger width α_1^{-1} in the dielectric. As k_{sp} increases, ω increases less linearly and aymptotically approaches to the cut off frequency. Near this cut off frequency, the surface plasma wave is strongly localised near the interface.

1.2.2 Excitation of surface plasmons at the THz frequency

The surface plasmons can be excited over the metal-dielectric interface using Kretschmann's and Otto's techniques in the optical and near-infrared regimes. However, at THz frequencies, metal behaves like a perfect conductor. Therefore, one cannot attain the desired skin depth into the metal films, which prohibits the excitation of surface plasmons. To address this issue, Pendry and his colleagues have theoretically generalized and developed a method for periodically structured, fully conductive surfaces. This allows you to design the dispersion of supported surface modes at almost any low fre-

quency [49]. These supported modes are confined near the surface and the structure on a much smaller scale than the probing radiation wavelength. A schematic diagram of their design is shown in the Fig. 1.4 (a). For a semi-infinite perfect conductor whose hole thickness is infinite, having periodicity and length 'a', the dispersion relation can be calculated as [49]

$$k_{||}^2 c^2 = \omega^2 + \frac{1}{\omega_{cut-off}^2 - \omega^2} \frac{64 a^4 \omega^4}{\pi^4 d^4}, \tag{1.4}$$

where,

$$\omega_{cut-off} = \frac{\pi c}{a\sqrt{\epsilon_h \mu_h}}, \tag{1.5}$$

$k_{||}$ is the wave vector along the metal surface, c is the free space light velocity, d is the distance between each hole, a is the length of these square apertures and ϵ_h, μ_h are the permittivity and permeability of any material that may be filling the holes. The dispersion relation is shown in Fig. 1.4 (b). From Eq. 1.2, it is clear that $k_{||}$ can be modified freely from the geometry of the structure and is a real number greater than the wave vector of the vacuum, which indicates a well-confined field as well as an infinite propagation length. $k_{||}$ shows a dramatic frequency-dependent characteristic and deviates increasingly from the wave vector in free space with increasing frequency, indicating both a lower phase velocity and a group velocity at higher frequencies. A

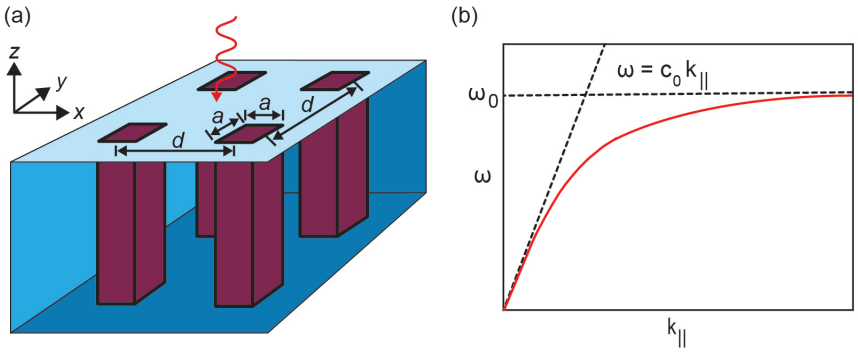

Figure 1.4: (a) Depicts schematic of the two-dimensional array of rectangular apertures (b) Shows dispersion relation of surface plasmon mode supported by the periodic array of rectangular apertures. From [49]. Reprinted with permission from AAAS.

smaller side length results in a smaller $k_{||}$ and weaker confinement, which mutates to the case of planar bare metal surfaces when the side length approaches zero. A similar

trend also occurs when the thickness of the hole decreases. Such a technical feature of the textured surface equips with a powerful platform for manipulating SPs in the THz range. Williams et al. took a measure of the rate of SPs confinement on a structured copper surface. The penetration depth of the measured intensity was in the order of magnitude of the wavelength. Therefore, the calculable intensity propagation length was about 5 cm around the band edge [45]. In addition to hollow apertures in metals, pillar structures, grooves, and flat structures can also support THz SPs [50, 51]. In particular, it has been shown that flat metal structures support SPs in TE mode [52].

1.2.3 Plasmonic structures for THz guided wave applications

Plasmonic waveguides with subwavelength dimensions are useful to transmit plasmonic signals from one point to different within the plasmonic photonics. In THz, patterned plasmonic waveguide in metal results the excitation of the THz surface plasmons. In the literature, we find various plasmon structures having extreme confinement, such as metal wires, metal slots, V-shaped grooves, and wedges. These plasmonic waveguides have been investigated for their potential in different applications such as slow light devices, high speed communication, filters, etc. This has kindled a lot of interest in developing plasmonic waveguide components that can operate at terahertz frequencies [53–55]. One of the advantages of propagation of surface plasma waves at THz frequencies along corrugated surfaces is their strong coupling to the interface and control on their dispersive properties depending upon geometrical parameters of the waveguide structures. Several research studies have been published examining the role of corrugations supporting terahertz surface plasmons. Ye et al. examined the propagation characteristics of a terahertz plasmonic waveguide with folded stub array by increasing the length of the folded stubs, which gives strong terahertz field confinement [56]. Guo et al. experimentally examined strongly confined terahertz propagation in a coplanar strip-line plasmonic waveguide, which promises ultra-wideband filter applications [57]. More recently, Yuan et al. designed a plasmonic waveguide composed of periodic metallic rectangular pillars and examined the

guided wave properties of waveguide devices such as S-bend and Y-splitter [58]. Owing to low loss and strong confinement features of terahertz surface fields, plasmonic guided wave devices can lead to several applications, including sensing, slow light phenomena, nano-imaging, nanoscale photonic components, etc [59–61]. Recently, Ma et al. reported highly sensitive refractive index sensing of liquids by measuring a frequency shift in the waveguide transmission spectrum of the terahertz surface plasmons polaritons [62]. Ferraro et al. examined a compact terahertz waveguide comprising rectangular strip and patches on a thin film to explore a narrowband terahertz plasmonic filter [63]. Due to the strong confinement of terahertz surface plasmon polaritons (SPPs), plasmonic waveguides have been shown to provide super-resolution focusing on imaging technology and detection systems [64, 65].

1.2.4 Design, fabrication and characterization

A one-dimensional plasmonic waveguide basically consists of three steps: numerical design, fabrication, and characterization. Here is a brief description of these steps.

1.2.4.1 Numerical design

Optimal THz plasmon waveguide design is extremely important for lower loss and highly confined terahertz mode propagation. This could be important in a large number of applications in the THz range. Commercially available electromagnetic numerical simulation packages can be used for design purposes. In our research work, we used commercial simulation software CST Microwave Studio (in Fig. 1.5). This is an electromagnetic 3D numerical simulation tool with the choices of each tetrahedral and hexahedral formed meshing. The mesh size is chosen to be adequate for accomplishing high accuracy of results in the case of THz plasmonic waveguides. The perfectly matched layer boundary condition has been selected in order to avoid reflections that can disturb the actual surface fields. The waveguides are excited to employ a broadband terahertz cycle at the one end of the waveguides through a waveguide port. An isolated waveguide port is utilized to detect terahertz surface plasmon polaritons. The

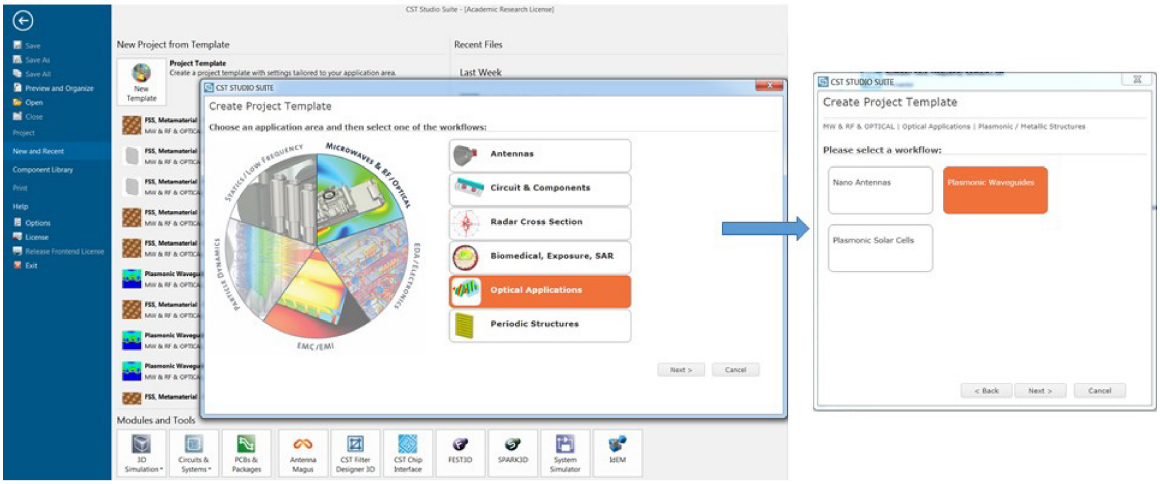

Figure 1.5: CST Microwave Studio Simulation Software Home Page.

waveguide material is assumed to be a perfect electrical conductor due to the high conductivity of metals at THz frequencies. In electric and magnetic field boundary conditions, we use an electric field normal to the surface and a magnetic field along the surface, however perpendicular to the direction of propagation. The time domain signal is collected at the detection waveguide port and transformed into a frequency domain waveform using Fast Fourier Transform (FFT). The waveguide geometry is simulated for the y-polarized incident wave under open boundary conditions in all planes. In order to examine, dispersion properties of the modes supported by the periodically patterned waveguides, we have used the Finite Element Eigenmode solver of the CST numerical simulation package. We numerically model a structure as a unit cell under the periodic boundary condition in the direction of propagation. The phase is varied from 0 to 180 degrees in order to extract dispersion properties of the terahertz modes supported by the waveguide.

1.2.4.2 Fabrication

We would like to highlight that fabrication of the proposed plasmonic waveguide could be accomplished via laser micromachining in metals or cleanroom fabrication techniques on a single crystalline silicon wafer. For thin metal sheet, laser micromachining techniques may be used to make apertures, and then, another planar metal

film can be glued on its back using the conducting epoxy [66]. In semiconductors, one may use heavily doped silicon of carrier concentration, $n \geq 10^{19}\ cm^{-3}$, which behaves like perfect conductor at terahertz frequencies. The surface of the silicon can be coated with a silicon dioxide (SiO_2) layer of 1-2 μm thickness, grown by the technique of low-pressure chemical vapor deposition (LPCVD). The surface can be patterned with periodic structures via photolithography. In the next step, appropriately designed silicon can be etched in a mixture of potassium hydroxide, water, and isopropanol in the ratio of 60:30:10 to make a pyramidal aperture. To fabricate a pyramidal groove, a silicon wafer can be stick on the bottom of the pyramidal aperture. The fabrication of plasmonic waveguides in silicon has been reported in the references [66] and [67]. To fabricate rectangular apertures, one can use the photolithography technique followed by deep reactive ion etching (DRIE) [68]. Several approaches, such as THz-time domain spectroscopy (THz-TDS) and incoherent techniques, are available to measure the terahertz radiation. For the waveguide measurements, one can use the THz-TDS system. [69].

1.2.4.3 Terahertz time domain spectroscopy (THz-TDS)

The fabricated samples of THz plasmonic waveguides can be characterized using the THz-TDS technique. A schematic of the THz-TDS setup to measure transmission properties of samples in the transmission modes and waveguide configuration is depicted in Fig.1.6. In this setup, a beam from a femtosecond (fs) laser system is divided into two beams using a beam-splitter: probe and pump beams. The pump beam generates THz pulses by optical rectification in ZnTe crystals, while the probe beam is used to scan and obtain the pulse profile. For plasmonic terahertz waveguide measurements, the coupling of terahertz waveforms from free space to the waveguide geometry is very important. The incident terahertz waves can be coupled in through a broad and flat circular or rectangular groove. The incident THz beam is linearly polarized within the direction perpendicular to the structures, whereas the magnetic field is parallel to the grooves. The THz field can be detected by electro-optical scanning, in

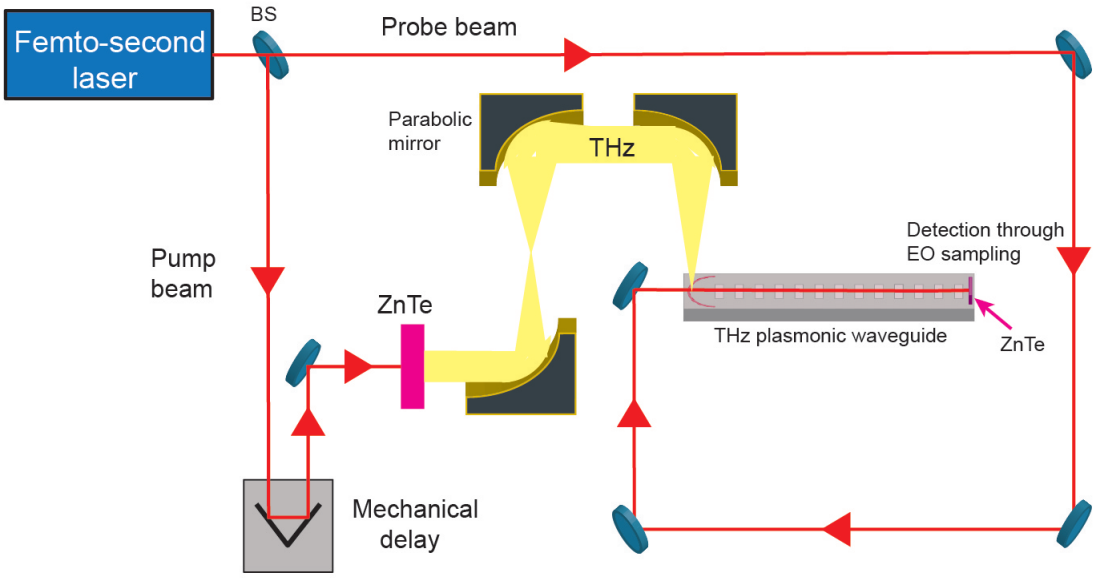

Figure 1.6: Schematic of the terahertz time domain spectroscopy setup.

which the probe pulse is modulated with the polariton field of the THz surface plasmon. A mechanical delay stage is used to provide a time delay between the THz pulse and the probe pulse. The THz waveform can be obtained by scanning this time delay. To increase the sensitivity, the pump beam is modulated by an optical chopper. This pulse information acquired in the time domain is transformed to the frequency domain with a Fourier transform from which spectral data can be obtained. Since the spectroscopic measurements through this technique are carried out by recording the THz waveform in the time domain, this technique is called THz-time-domain spectroscopy (THz-TDS). In a pulsed THz system, the probe pulse samples the THz pulse and records its electric field as a function of time. The THz field in the frequency domain is a complex value consisting of amplitude and phase information.

1.3 Important concepts of plasmonics in context of thesis

1.3.1 Thin-film sensing via surface plasmons

THz sensing using plasmonic metamaterial structures can be performed either in transmission, reflection, or waveguide configuration. In the reflection and transmission configurations, there is little interaction between the analyte and the incident elec-

tromagnetic wave, limiting their sensing capability. However, in waveguide configuration, the incident wave, once coupled to the waveguide structure, interacts with the analyte attached to the constituent structures for several orders of wavelengths. Several waveguide geometries have been investigated for their sensing capability in the last decade [70–73]. In this context, Ma et al. have reported highly sensitive refractive index sensing of liquids by measuring a frequency shift in the waveguide transmission spectrum of the terahertz surface plasmons [62]. In this study, resonant plasmonic frequencies are shown to be intensely dependent on the refractive indices and thicknesses of analytes attached to the planar waveguide. They have successfully identified granular analytes of different quantities by measuring shifts in the resonant dips. In another study, Hanham et al. designed and fabricated a corrugated metal surface comprising a linear array of subwavelength grooves [74] and investigated the resonance shift of the fundamental mode by filling grooves with various fluids. Highly confined terahertz surface plasmons enhance the light-matter interactions and hence the sensitivity to identify an analyte in the vicinity. You et al. have also reported a hybrid terahertz plasmonic waveguide for sensing an analyte by measuring a shift in the resonance dip concerning the analytes of different quantities [75]. Recently, Islam et al. reported a comparative study of the sensing ability of a plasmonic waveguide with different shaped structures [76]. The sensitivity and figure of merit of the fundamental mode are compared for the rectangular and V-shaped grooves.

Intuitively, a subwavelength structure of a plasmonic waveguide can be thought of as a lumped circuit element having components as inductance (L), capacitance (C), and mutual inductance (M). When the THz radiation is coupled to the plasmonic structure, it causes the excitation of oscillating current inside the structure, thus producing an inductance L. With the alteration of currents, the charge accumulates in some areas of the groove, leading to the creation of an effective capacitance C. In transmission line theory, plasmonic and metamaterial structures have resonant characteristics determined purely by their inductance (L) and capacitance (C) values. As waves prop-

agate along with the corrugated pattern, they experience scattering, dispersion, and diffraction losses, which explain the broad resonance in numerical simulations. Using the transmission line LC circuit model, we have been able to validate and understand numerical observations in the case of the plasmonic waveguide as refractive index sensors. We assume that a unit cell consists of two corrugations interconnected by the mutual inductance M. The intrinsic impedance (Z_0) of the circuit can be calculated from the dimension of the plasmonic geometry. The circuit impedance (Z_s) is dependent upon the circuit that represents the corrugated structure. By solving the conventional form of the transmission equation, one can determine the transmission amplitude ($t(\omega)$) corresponding to the intrinsic and circuit impedances,

$$t(\omega) = \frac{2Z_S}{Z_0 + Z_S}, \tag{1.6}$$

1.3.2 Near field coupling between resonators

Although considerable attention has been given to study terahertz plasmonic waveguides in recent years, these studies have primarily used a single corrugated structure as a unit cell. When two corrugated structures are close enough to each other, they interact via magnetic and electric field lines, giving rise to novel phenomena and exciting applications that may not exist in a conventional plasmonic waveguide. The proximity field arrangement of structures brings about various effects such as mode hybridization effect, induced absorption, broadband modulation, and electromagnetically induced transparency (EIT). In general, the near-field coupling is important when the distance between the corrugations is much smaller than the excitation wavelength (λ) and much smaller than the dimensions of the structure. Such mutual coupling plays a vital role in changing the overall behavior of the plasmonic waveguide. In this regard, various symmetrically shaped corrugated structures for the propagation of surface plasmons and their consequences in different applications have been investigated. However, research investigating the role of asymmetric resonators in the propagation of surface plasmons is minimal. Zhang et al. numerically

investigated a semiconductor-insulator-semiconductor (SIS) terahertz waveguide to explore plasmon-induced transparency and slow-light phenomena analyzing the near field coupling of two asymmetric stub resonators [58]. Additionally, Fano resonances in terahertz waveguides have been shown to exhibit strong confinement along with the ultra-sharp asymmetric line shape. It originates from the coherent coupling and destructive interference between a discrete state and a continuum state. The discrete state results from the geometrical parameters of the waveguide constituents, while the continuum band comes from the incident signal. Fano resonances possess a very high slope in spectra along with strong dispersion. Therefore, they are significant in various applications, such as ultra-high sensitive sensors, light field enhancement, optical storage, etc. [77–80]. Despite the considerable interest in intense Fano interferences, none of the studies have reported near-field coupling of resonances in the planar plasmonic terahertz waveguides to the best of our knowledge. It may be noted that the asymmetry in resonators can provide an extra degree of freedom to tune the dispersion properties of surface plasmons when placed nearby. A strong near-field coupling between the resonances from the asymmetric resonators can lead to the interference of the support modes. This results in several applications such as electromagnetically induced transparency, anomalous absorption, slow light effect, etc. This can be managed by controlling the near-field coupling of the resonances without changing the physical parameters. The near-field coupling of resonances and their manipulation in the planar configuration can be vital in designing plasmonic waveguides for on-chip communication devices. Therefore, there is a strong need to advance research exploring the near-field coupling between the asymmetric resonators and understanding the underlying coupling mechanism.

A system of two resonators in close proximity can be described by a three-level atomic system with two plasmonic modes at slightly different frequencies. They are coupled in a near field configuration via a strong electric field profile. Since the two resonators are simultaneously excited directly by the incident terahertz, they can be

termed the bright resonators. By resolving the coupled Lorentz oscillator system according to two radiation resonance modes, one can calculate the transmission amplitude and validate the numerical results.

1.3.3 Plasmon Induced Transparency (PIT)

Electromagnetically induced transparency (EIT) is a three level quantum mechanical phenomena in which destructive interference between the two optical signals lead to strong dispersion and causes transmission in an otherwise absorptive medium. This effect has many potential applications in optical filtering, storage devices, and sensing technologies. Over the past decade, metamaterial (MM) and waveguide structures have been associated to explore EIT phenomenon. MMs have been found to mimic EIT through careful arrangements of the structures. In the context of waveguide structures, the EIT phenomenon has been widely reported based upon the excitation of localized plasmon resonances through structures composed of two metallic components of different dimensions. The two metallic components or resonators act either as two bright modes or as bright and dark modes. Generally, coupling of bright-dark modes or bright-bright modes are the key to realize EIT like behavior. It has been observed that the bright mode is the one that couples strongly with the incident excitation field while the dark mode weakly couples with the incident electric field. For EIT effect, both modes should have nearby resonant frequencies and the interference effect of these modes gives a narrow transparency region. Around the transparency window, there is an abrupt change in dispersion over a narrow spectral range that can be used where a sharp and pronounced spectral response is highly desired. It has attracted a lot of attention because of its potential usage in various fields such as nonlinearities, optical data storage, modulations, ultrahigh sensors, and slow-light application. The EIT effect has been realized in multiple configurations, including coupled-resonator systems [81], gratings [82], and waveguides [83]. In waveguide configurations, Xu et al. have experimentally observed a Si microring resonator coupled to a parallel waveguide to realize a transparency window by constructive interference [84]. Recently, PIT,

an analog of EIT, has drawn more attention due to its promising on-chip applications. This effect is caused by localized plasmons (usually bright mode) on the surface of the metamaterial. It is excited by incident electromagnetic radiation and undergoes destructive interference with another mode (bright or dark mode) of approximately the same frequency resulting from the metamaterial constituent placed in closed proximity. In this context, Zhao et al. have demonstrated the PIT effect in a subwavelength metal structure waveguide consisting of metallic cut wires and double-gap split-ring resonators [85]. The investigations so far in this area have focused on passively tuning the PIT response. Modulation of the PIT effect, despite being significant, has not been examined so far, to the best of our knowledge. There is a strong need to pursue research in this direction.

A modelling approach based on coupled harmonic oscillator systems can be used to understand the underlying concept of the PIT. The equations of motion can be written for this coupled system, in which both resonators are driven by the external force. Here incident terahertz wave acts as the driving force for both resonators. After solving the differential equation, one can calculate the transmission amplitude for the system.

1.4 Metamaterials

Apart from plasmonics, metamaterial structures have also been implemented for their potential in various THz device applications. Metamaterials are composed of periodically arranged artificial structures consisting of metal-dielectric-metal or all-dielectric layers with subwavelength sizes. As expected, the effective media parameters of such a structure are strongly dependent on the material properties and geometries used in the design of the unit cell and their specific periodic arrangement. Many metamaterial unit cells designed to operate at terahertz frequencies are made of metal (gold, silver, copper, etc.) and dielectric materials (silicon, polymer, polyimide, etc.) on a dielectric substrate. These structures can efficiently manipulate electromagnetic responses that are not present in nature. This is excellent news for researchers

working in the THz frequency range, mainly due to the introduction of metamaterials that can be engineered to have the desired properties of THz radiation. Metamaterials have opened up new and promising avenues to manipulate THz radiation by controlling constructed structures artificially. It guarantees many applications such as THz sources, lenses, switches, modulators, cloaking devices, filters, and detectors [86–88].

1.4.1 Dielectric metamaterials

Recently, it has been found that dielectric metamaterials (DMs) composed of dielectric microstructures can offer the possibility to achieve properties similar to their metallic counterparts but with significantly lower absorption loss and fabrication complexity. Furthermore, their intense magnetic and electric Mie resonance can be applied for realizing near-zero refractive index, perfect absorbance, electromagnetically induced transparency, DC magnetic cloak, and silicon colloid nanocavities [89–93]. Fig.1.7 shows the some of dielectric metamaterial geometries recently reported n literature. Fig.1.7 (a and b) depicts two asymmetric dielectric resonator with image of fabricated sample where geometry has the ability to exhibit the EIT phenomena. In Fig.1.7 (c and d), metamterial with dielectric rings and cylindrical disk is shown. This configuration was used to demonstrate the sensing features. Among these various THz devices, an absorber that can capture wave energy efficiently is of vital importance. Metamaterial absorbers have attracted particular attention because of their ability to modulate arbitrary frequency and amplitude by independently designing their geometry.

1.4.2 THz metamaterial absorber

Recently, the artificially designed material absorber called “metamaterial absorber” has attracted much attention because of its excellent optical and electromagnetic properties. A typical metamaterial absorber consists of a three-layer structure with a sub-wavelength metal sub-wavelength structure array, a dielectric spacer, and a metal reflector. Nearly a single absorption characteristic is usually achieved by the ohmic and dielectric losses of the device, leaving no transmission and reflection of the incident

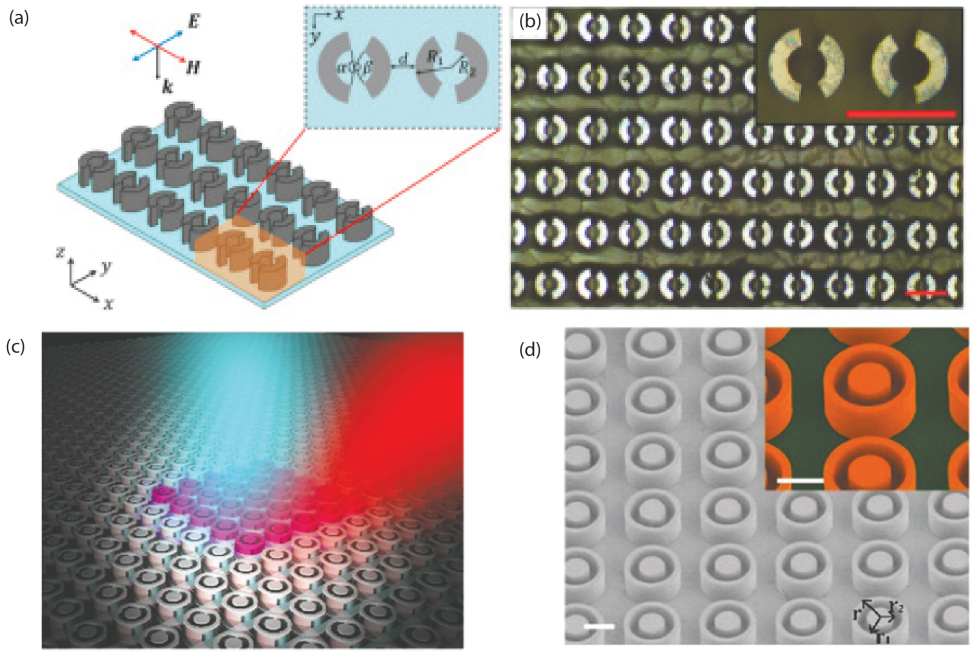

Figure 1.7: Some terahertz dielectric metamterial geometries and their application in different areas(a) Schematic of the all-dielectric metamaterial composed of two asymmetric split ring resonators with EIT effect (Reprinted with permission from [89]) (b)Microscopic image of the fabricated samples. (c) All-Dielectric metamaterial absorber as sensor (Adapted with permission from [94])(d) SEM image of the fabricated sample

wave. Several geometrical configurations have been employed over a wide range of the electromagnetic spectrum. For instance, periodic arrays, split-ring resonators, circular rings, and multilayer structures have been reported at frequencies ranging from microwave to near-infrared. The terahertz range has attracted increasing attention due to the growing number of practical applications in spectroscopy, imaging, communication, astronomy, etc. Recently, multiband terahertz absorbers are getting more and more attention. In this context, Kearney et al. proposed a multiband absorber consisting of aluminum (Al) squares of various sizes, SiO_x spacers, and a periodic arrangement of Al ground plane for THz sensors. Appasani et al. demonstrated a multiband terahertz absorber with a split square ring resonator. While Wang et al. proposed a quad-band terahertz absorber formed by an asymmetric resonator and a six-band terahertz absorber using a dual-layer stacked resonance structure. The electromagnetic properties of these metamaterial absorbers can be explained by effective parameters

such as effective permittivity and effective permeability. Due to their exotic properties, metamaterial absorbers have many valuable applications in modulators, sensors, imaging, cloaking devices, and photodetectors [95–98].

1.4.3 Design, fabrication and characterization of THz metamaterials

1.4.3.1 Numerical design

To design metamaterial structures and study their response to incident electromagnetic radiation, we use the same software package for electromagnetic simulation as the plasmon waveguide. We optimized our design parameters before getting into the complex and expensive fabrication process. For metamaterial structures in the transmission configuration, the unit cell boundary condition is chosen to take into account a unit of the constituent of the metamaterial, i.e., a meta-molecule. This leads to a planar metamaterial geometry of an infinite number of unit cell structures. Similar to the plasmonic structures, two waveguide ports are used for the excitation signal and the detection of transmitted THz radiation in the frequency domain.

1.4.3.2 Fabrication

These designed metamaterials can be fabricated using the photolithography or electron beam lithography (EBL) technique. In photolithography, the first photoresist is coated with the silicon substrate. After that, metamaterial structures are patterned using the appropriately designed masks and illuminating the substrate with and ultraviolet light followed by the development process. Then, a thin metal layer is vapor-deposited using the electron-beam (e-beam) or thermal evaporator. Finally, the metamaterials structures are obtained after the lift-off process, during which residual photoresist is removed.

1.4.3.3 Terahertz time domain spectroscopy (THz-TDS)

The fabricated metamaterial samples can be characterized using the THz-TDS technique discussed in the previous section through Fig. 1.6. To study the transmission response, the metamaterial samples can be placed between the parabolic mirrors of

the experimental setup.

1.4.4 Absorption modulation

As described in the previous section, terahertz technology holds promise for many applications such as imaging, spectroscopy, and communications. These applications increase the need for THz modulators with high modulation depth, wide operating bandwidth, and high modulation speed [99–101]. Manipulating THz light to achieve high modulation depth and broadband response in one device is a significant challenge. Dynamic modulation of metamaterial absorbers enables signal modulators, switches, and spatial light modulators. Many modulation mechanisms have been proposed to control the intensity and resonant frequency of the MM electromagnetic response, including optical excitation, mechanical actuation, thermal or electrical control [102, 103, 103–105]. In this regard, several metamaterial configurations have been reported citing their potential as terahertz narrow and broadband absorbers. Recently, Zhu et al. have investigated a broadband metamaterial absorber consisting of a metal-dielectric multilayered pyramid-shaped geometry [106]. They experimentally demonstrated the ultra-wideband absorption response when the lateral width of the layers was gradually increased. Wang et al. have numerically demonstrated the six-band tunable metamaterial absorber composed of two alternating stacks of metal-dielectric layer [107]. They showed a spectral shift in absorption when structural dimensions of the geometry were varied. These studies have primarily focused on passively modulating the absorption characteristic. However, actively tunable absorption modulation needs attention owing to its applications in actively tunable terahertz devices. Unlike traditional metamaterial absorbers, graphene or semi-metal-based tunable can work at tunable frequencies without refactoring. The conductivity of graphene can be modulated by controlling the doping and the external bias voltage. In recent years, graphene structures have been used to effectively modulate the terahertz absorption response by exploiting surface plasmons at terahertz frequencies [108]. In this context, Xu et al. examined a dielectric slab over a metallic ground plane covered by a graphene sheet.

They reported improved absorption bandwidth concerning increased biased voltage for orthogonal polarizations owing to the excitation of surface plasmons [109].

1.5 Motivation of thesis work

The plasmonic and metamaterial structures are prevalent because of several applications in the different areas, as mentioned in the above sections. From the preceding discussion, it has been realized that there is still a need for efficient plasmonic waveguides and metamaterial devices for THz application. As discussed, Terahertz sensing technology using plasmon waveguide is important for label-free index sensing of the analyte and is focused on excitation in the fundamental mode for this. However, depending on the shape and size of the structure, the plasmon waveguide can also lead to higher-order modes, which can have a decisive impact on the detection of the analyte. High-quality factor-mode excitation could lead to high-sensitivity detection with higher resolution and has not been studied in plasmonic waveguides that motivated my work. Further, very little work has been reported for resonators coupling in the context of plasmonic waveguides. This near-field coupling of resonators can provide an extra degree of freedom to tune the dispersion properties of surface plasmons when placed in close proximity. Therefore, we have tried to understand the coupling aspect in our study. Additionally, the PIT effect has been investigated through different configurations in recent years. In this regard, metal structures in the form of ridges, grooves, or holes of slightly different dimensions are widely used to explore the PIT phenomenon. In order to tune the PIT response, the dimensions of the structures are varied, which is a cumbersome process and limits its potential for active device construction. In this work, we addressed this challenge so that we could change the response to the PIT effect without changing the physical dimensions of the structure. In addition, there is great interest in developing terahertz absorbers and modulators in this rapidly growing field of study. Several metamaterial configurations have been reported citing their potential as a narrow and wide absorber in the terahertz range.

These studies mainly focus on the passive modulation of absorption characteristics. Therefore, actively tunable absorption modulation needs attention owing to its applications in actively tunable terahertz devices. In my last work, we have explored the possibility of tuning the broadband absorption.

1.6 Plan of thesis

In our thesis work, the primary focus has been to investigate terahertz plasmonic and metamaterial structures for applications in sensors and modulators. Plasmonic waveguides evoke both fundamental and higher-order modes that depend on the shape and size of their structures, which can be important for analyte detection. Due to the longer interaction of the terahertz modes with the groove pattern of the waveguide, it can detect an analyte with higher sensitivity. Therefore, the sensing capabilities of plasmonic waveguides are investigated, taking pyramidal groove patterns into account. In addition, the propagation of terahertz surface plasmons was studied by pattering the metals with asymmetrical rectangular apertures in close proximity. Two resonators address this aspect of near-field coupling with slightly different sizes. Next, electromagnetically induced transparency phenomena in waveguide structures were investigated, where the transparency effect can be controlled as a function of the shape and size of its components. In the case of terahertz metamaterials, a tunable metamaterial absorber based on an array of graphene nanoribbons is being investigated. The study could make it feasible to design the metamaterial absorber for acquiring better absorption characteristics. The whole thesis has been divided into seven chapters. The organization of this thesis chapters are as follows:

Chapter 1 gives a general introduction of the THz waves, sources, detectors, and their applications in the different areas. We discussed THz plasmonics, the generation of surface plasmons at THz frequencies, and the applications of the THz plasmonic waveguide. In this chapter, we illustrated the numerical design, fabrication, and characterization of THz plasmon and metamaterial structures. This chapter also describes

the vital idea of this thesis work. Moreover, it additionally summarizes the thesis contribution and presents a quick outline of the thesis organization.

Chapter 2 investigates the sensing capabilities of a planar plasmonic waveguide comprising of periodically arranged pyramidal corrugations. This designed THz plasmonic waveguide supports highly confined terahertz modes and offers a much longer interaction between the analyte and the terahertz radiation. The dispersion properties of the fundamental and higher-order modes of the waveguide were examined to ensure the plasmonic properties of the waveguide. The waveguide transmission spectra for different lengths of the corrugations have been investigated. We validate the numerical results by employing a semi-analytical transmission line model to our waveguide geometry. We thoroughly analyze the various waveguide sensing parameters such as quality factor, the figure of merit, frequency shift, and sensitivity.

Chapter 3 deliberates the near field coupling of a surface plasma wave in a planar THz plasmonic waveguide comprising a 1D-array of periodically arranged asymmetrical rectangular apertures positioned along the transverse direction. The structures are assumed to be periodically patterned rectangular apertures in a thin sheet of metal and ensure the plasmonic response of the waveguide. The unit cell of the waveguide geometry comprises two subwavelength scale rectangular apertures with different lengths adjacent to each other along the transverse direction. We have investigated the near field coupling of surface plasmons from the asymmetric size resonances via the excitation of each aperture simultaneously. The findings are supported by a theoretical model based on the three-level plasmonic system.

Chapter 4 discusses the plasmon induced transparency (PIT) effect and its modulation in the terahertz guided systems. The waveguide geometry is composed of two slots in parallel slabs in the transverse direction. A particular gap is maintained between the slabs for terahertz transverse magnetic mode propagation. One rectangular slot is filled with a dielectric material, and the other one is empty. We examined the corresponding transmission amplitude and the change of phase value of the transmit-

ted terahertz signal. Further, we have calculated group index values corresponding to the phase values. Also, a theoretical model based on coupled harmonic oscillator has been devised to explain the PIT effect of the waveguide to validate the numerical findings. The refractive index of the dielectric material is varied to observe the tunable control of the PIT effect. A comprehensive picture of modulation of the effect with the refractive index is presented through the contour plot.

Chapter 5 explores the tunability and switching of the induced transparency window in an air dielectric grooved parallel plate terahertz waveguide. The structure consists of two parallel pyramidal grooved patterned metal blocks that maintain a particular gap. One of the two pyramidal grooves is filled with a dielectric material of varying refractive index to study the modulation of the PIT window; the other one remains empty. We examine the terahertz transmission characteristics where these two pyramidal grooves support resonant modes at two different frequencies adjacent to each other. The strong coupling between modes causes the PIT effect in the proposed configuration. We have verified the PIT effect with the help of a three-level plasmonic model. To achieve modulation of the PIT effect, we varied the refractive index of the dielectric material filled in one of the grooves. We have further demonstrated that the resonance and PIT effect can be tuned by varying the conductivity of the Si sheet placed between the grooves.

Chapter 6 examines the tunable terahertz absorption modulation in graphene-based dielectric metamaterial. The unit cell of the metamaterial absorber consists of a stack of four layers. From top to bottom, they are: SiO_2 layer of frustum-shaped geometry, a periodic array of graphene nanoribbons, the SiO_2 spacer layer, and a layer of a gold metallic reflector, respectively. All the layers are stacked together to form a unit cell of the metamaterial absorber. Broadband absorption modulation is observed for various values of the chemical potential of graphene nanoribbons. We examined the effect of each layer on the performance of the proposed configuration. We have first investigated the role of free-standing graphene nanoribbons on broadband absorption

and combined it with the SiO_2 dielectric spacer and gold metallic ground plane. We employ the theoretical approach based on effective medium theory and transfer matrix method to verify the numerical findings. Electric field distribution has also been studied to understand the role of both dielectric layers, which reveals their importance in broadband absorption.

Chapter 7 presents the final comment based on the work presented in the previous chapters. All the objectives have been reviewed, and also the findings have been highlighted. In addition, future papers have been outlined to expand the research reported therein.

2

Thin film sensing in terahertz plasmonic waveguide

Contents

This chapter describes the sensing capabilities of planar plasmonic terahertz waveguides which are found to support fundamental and higher order resonances. We compare them in terms of their quality factor, figure of merit (FoM) and sensitivity to further understand.

2.1 Introduction

In recent years, terahertz sensor technology using plasmonic waveguides has become increasingly important in label-free refractive index sensing of analytes, with a major focus on fundamental mode excitation. However, plasmonic waveguides also result in higher order modes depending upon the shape and size of its structures, which can be crucial for sensing analytes. Further, the role of high quality factor modes is important to sensing a substance, which has not been looked upon in plasmonic waveguides designed for sensor applications to the best of our knowledge. The excitation of high quality factor modes can results in highly sensitive detection with greater resolution. In this work, we have tried to address these issues by designing a plasmonic waveguide capable of supporting multiple resonances. The fundamental and higher-order resonances are compared in terms of their Q-factor so as to have check on the quality of the modes and further to establish their sensing potential. The higher-order mode in plasmonic waveguides could be very significant in developing the highly sensitive refractive index sensors because of the high-quality factor. Here, we consider inverted pyramidal grooves to examine the sensitivity of analyte in plane waveguide configuration. The waveguide with pyramidal corrugations could be very advantageous in sensing analytes with better sensitivity because of its ability to strongly confine the electric field of the mode as well as filling the analyte quantity more effectively owing to its shape [110, 111]. The strong confinement to the surface is highly desirable for sensing applications as the analyte at the surface extensively interacts with the surface wave on the order of several wavelengths. As compared to previous investigations of sensing capabilities of plasmonic waveguide reported in the

literature [115–117], we have observed that our design promises higher sensitivity for the 2^{nd} order mode compared to the fundamental mode.

We study the sensing capability of a planar plasmonic terahertz waveguide consisting of an array of pyramidal grooves in one dimension. The chapter has been organized as follows: First, we numerically calculated the dispersion properties of the proposed plasmonic waveguide and examine frequency-domain THz waveguide transmission response for different groove lengths. The contour and color plot is analysed to present a comprehensive picture of the change of resonant behaviour with the change in length of grooves. We have also examined the dispersion properties of the waveguide with grooves of different heights in this section. In order to understand numerical observations, in the next section, we present an equivalent semi-analytical transmission line model and calculate the resonance response of waveguide in conjunction with the numerically obtained results for different groove lengths. In order to check the quality of the modes, we examine the quality factors of fundamental and higher-order modes in the next section. Further, we investigate the sensing capability of the modes by filling them with a fixed amount of analyte of different refractive indices while measuring their corresponding frequency shifts. In the end we provide a discussion to our findings.

2.2 Design of THz waveguide with inverted pyramidal corrugations

We design one-dimensional plasmonic waveguide using periodically arranged subwavelength scale corrugations in the form of pyramidal grooves on a thin sheet of metal. The schematic of the proposed plasmonic waveguide geometry is shown in Fig.2.1. The grooves parameters are chosen to be, length (s) = 0.5 mm, depth (d) = 0.5 mm, and periodicity (p) = 0.25 mm remain fix throughout the study. The grooves are pyramidal in shape with a narrow gap at the top. The upper and lower widths of the groves are chosen to be a_1 = 0.05 mm and $a_2 = 0.15$ mm respectively. The length of the grooves is varied for calculating dispersion relations and the terahertz waveguide

transmission.

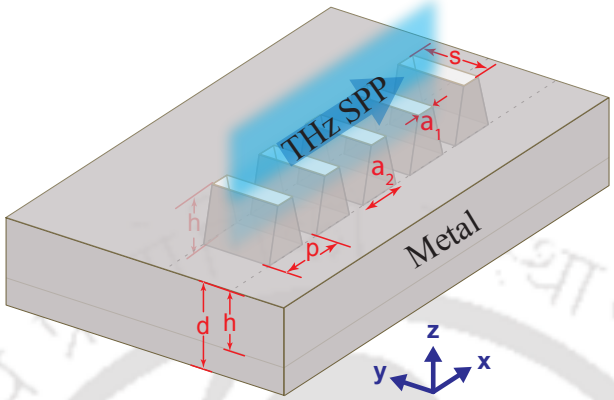

Figure 2.1: Waveguide Schematic: 3-Dimensional view of the waveguide comprising one dimensional array of periodic corrugations.

2.3 Dispersion characteristics of the waveguide

The dispersion relation of the fundamental and higher-order mode supported by the proposed plasmonic waveguide is obtained by numerical simulation. The numerical simulations have been performed using the finite element time domain and the Eigen mode solver of the CST Microwave Studio simulation software. The waveguide structure is simulated under periodic boundary conditions along the direction of light propagation and absorbing layers condition in the transverse direction. We have assumed metal to be a perfect electrical conductor (PEC) owing to its high conductivity at terahertz frequencies. The simulation assumes a tetrahedral grid of size $\lambda/10$ that indicates the sub-wavelength range. The results of the dispersion relations for two different lengths of the grooves are shown in Fig.2.2(a). The dispersion relations of fundamental mode for s = 600 μm and s = 500 μm are represented by solid red and green traces, respectively, however the 2^{nd} order mode dispersion properties are represented by dotted blue and orange traces, respectively. The black line indicates the light line. From the plots, it may be noticed that the frequency monotonically increases in the beginning with the wavenumber, however it saturates at the boundary of 1^{st}

Brillouin zone. For the case of groove length s = 500 µm, dispersion curve of fundamental and higher order mode saturates at 0.31 THz and 0.49 THz, respectively. These saturation frequency values correspond to zero group velocities and cutoff frequencies. As the groove length increases, the dispersion curves of both modes shift away from the light line and saturate at lower frequency values. While for s = 600 µm, the cut off frequency of fundamental and higher mode are 0.27 THz and 0.47 THz, respectively. Further, we calculated the dispersion relations of fundamental and higher-order

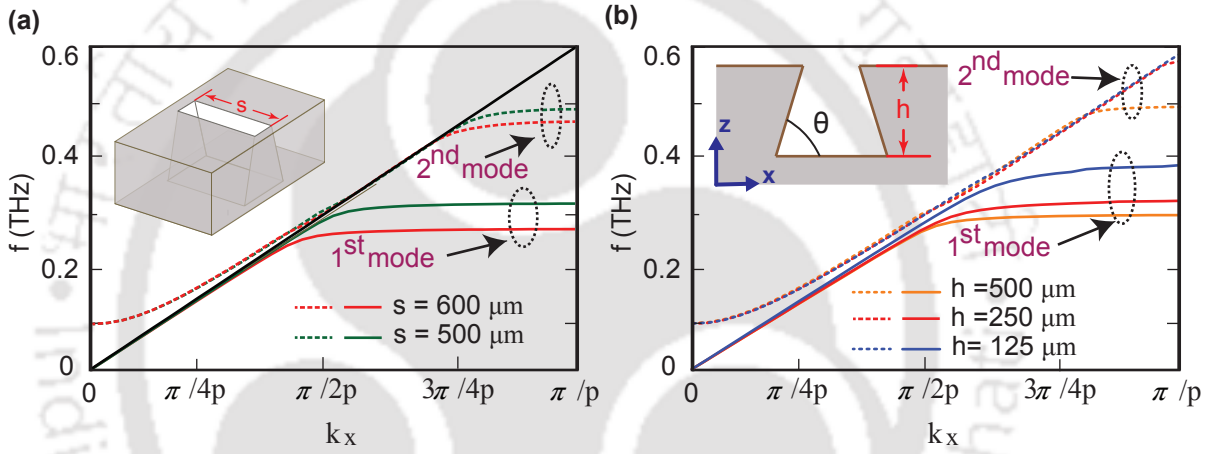

Figure 2.2: Numerically calculated dispersion properties of the fundamental and higher order modes in the proposed plasmonic waveguide having a) different transverse length of the pyramidal grooves i.e. s = 600 µm and s = 500 µm. b) different depth grooves i.e. h = 500 µm, $h/2$ = 250 µm, $h/4$ = 125 µm.

modes for different groove depths. Fig.2.2(b) shows dispersion curves for three different depth of grooves (h) that is related to the slanted angle (θ) as $\theta = tan^{-1}\left(\frac{h}{a_2/2}\right)$. For this study we have varied the groove depth from h = 500 µm, $h/2$ = 250 µm, $h/4$ = 125 µm and fixed other parameters of the structure at a_1 = 50 µm, a_2 = 220 µm & s=500 µm. The dispersion relation of fundamental mode for h = 500 µm, h = 250 µm, and h = 125 µm are represented by solid orange, red, and blue traces respectively whereas dotted traces indicates the 2^{nd} order mode for the same. We note that as the depth of pyramidal grooves increased, the dispersion curve saturates at lower frequency value. This saturation frequency value depends upon the dimensions of the pyramidal grooves and can be verified from the cavity Eigen frequency equation [112–114].

2.4 Plasmonic waveguide transmission

2.4.1 Numerical analysis

To analyse the waveguide transmission, we excite the waveguide with a discrete source of single-cycle terahertz waveform at its one end. Our umerical study assumes a waveguide with a length of 4 cm. The signal once coupled to the corrugated structures, it propagates along with one-dimensional waveguide pattern and finally detected at the other end. The detected time-domain signal is converted into the frequency domain spectra using Fast Fourier Transform (FFT). For our simulation, we used the finite element time domain solver of CST microwave simulation software. It is important to highlight that the proposed waveguide can be fabricated via conventional photolithography technique by using a highly doped silicon substrate while taking advantage of its crystalline structure. The corrugations of the waveguide depend on the crystal orientation of the silicon substrate. To make pyramidal grooves, one can use a crystalline silicon wafer of (100) orientation with dopant concentration, $n \geq 10^{19} cm^{-3}$ which behaves like a perfect conductor at terahertz frequencies. Using low-pressure chemical vapor deposition (LPCVD) technique, the silicon dioxide layer can be grown on the silicon surface and further, patterns can be made via photolithography technique [118,119]. In the next step, appropriately patterned silicon can be etched in a mixture of potassium hydroxide, water, and isopropanol in the ratio of 60:30:10 to make inverted pyramidal apertures [120]. For the fabrication of groove, a silicon wafer can be glued on the back of the pyramidal apertures using a conducting epoxy. For characterization, one can use the technique of terahertz time-domain spectroscopy (THz-TDS) [121]. We have first calculated terahertz waveguide transmission for different lengths of the pyramidal structures. The results are shown in Fig.2.3(a) the black traces represent terahertz frequency domain spectra for the case of s=600 μm. It is apparent from the spectra that it exhibits two resonant modes with anti-resonance frequencies of fundamental and 2^{nd} order mode appearing at 0.27 THz

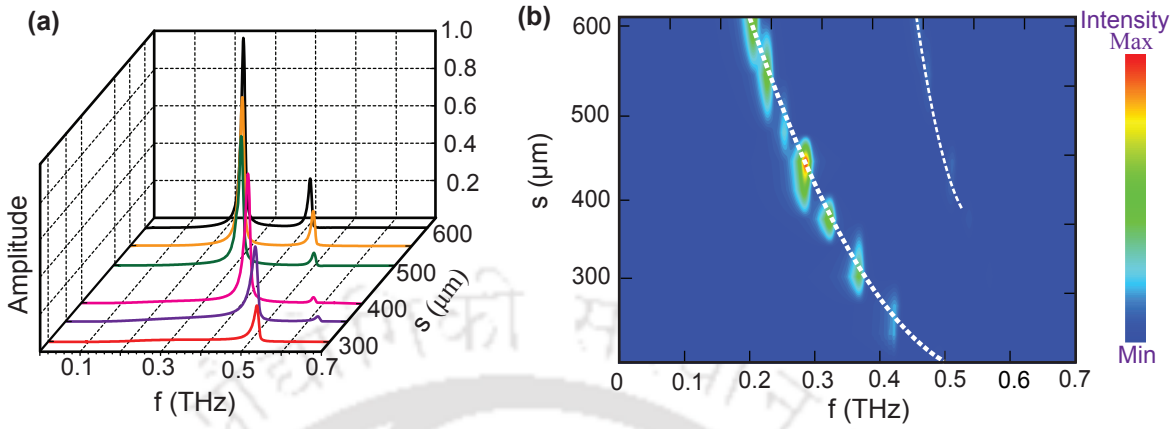

Figure 2.3: a) Numerically simulated frequency domain terahertz waveguide transmission for the plasmonic waveguides having pyramidal structure with different groove length i.e. s=600 μm, 550 μm, 500 μm, 450 μm, 400 μm, 350 μm and 300 μm; b) Contour plot of numerically simulated THz transmittance for different values of s.

and 0.47 THz, respectively. These anti-resonant frequencies can be verified from the cavity Eigen frequency equation. The anti-resonance frequencies result from the interference of discrete and continuum spectrums and significant to terahertz waveguide transmission. As the length of the grooves is decreased, the anti-resonant frequencies of the modes get blue shifted. For s=500 μm, the frequencies of the fundamental and 2^{nd} order modes turns out to be 0.31 THz and 0.49 THz respectively. In our study, we have varied groove lengths as, s = 600 μm, 500 μm, 400 μm, and 300 μm and a blue shift trend in the anti-resonance frequencies is apparent from the figure. In order to present a comprehensive picture of this variation, in Fig.2.3(b) we have shown the contour color plot of the terahertz waveguide transmission. The decrease in groove length (s) causes the transmission curve to blue shift and saturate it to a higher anti-resonance frequency. A blue shift in the resonant behavior of the fundamental and 2^{nd} order mode is apparent. Further, we observe a decrease in the amplitude of the resonances with the decrease in the groove width. This happens due to the lower field trapping capability of the smaller groove lengths. As we decrease the groove length to s=300 μm , we observe only the fundamental resonance, however 2^{nd} order modes completely vanish. From the contour figure it is clear that confinement of the electric

field is changing with the length of the pyramidal grooves. In Fig.2.3(b), the first dotted trace is showing the fundamental mode and the second trace is showing the higher order mode. For the higher order mode, on decreasing the value of the groove length (s) electric field confinement is also reducing.

2.4.2 Semi-analytical approach

In order to validate numerical finding and develop more physical insight into transmission response of the proposed plasmonic waveguide, we employ an equivalent semi-analytical transmission line model. The details of this approach in the context of plasmonic structures can be followed from the reference [122]. This analysis assumes that the metal carrier density is very high and the pyramidal grooves behave like an RLC circuit in the transmission line approximation.The circuit model of a unit cell is

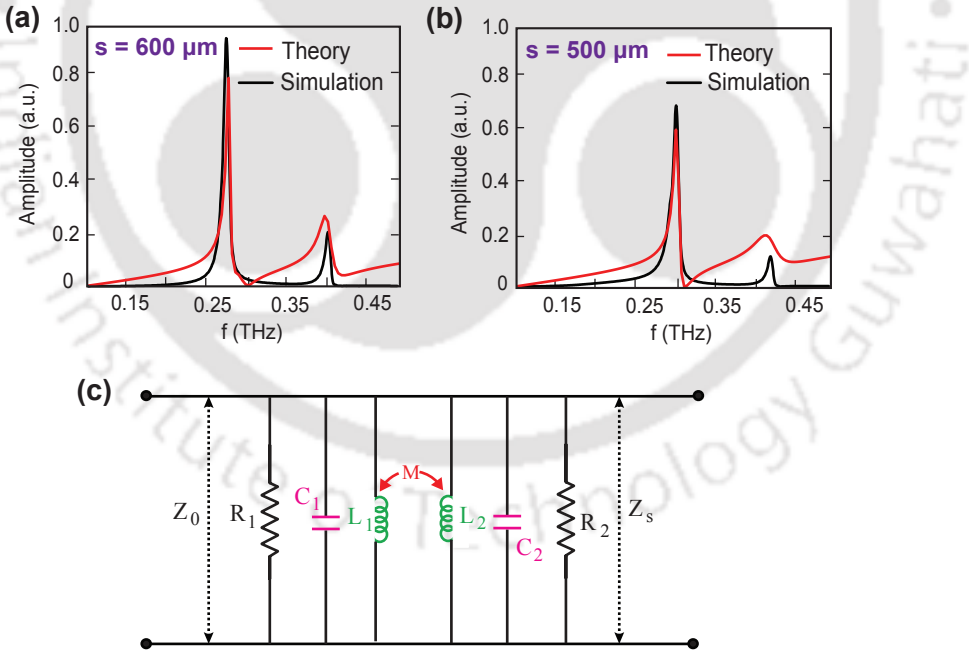

Figure 2.4: a) Waveguide transmission from transmission line theory(TL) for groove length s= 600 μm; b) Waveguide transmission from transmission line theory(TL) for groove length s= 500 μm; c) Schematic of TL-RLC circuit model. The circuit components R_1, L_1, C_1 represents the resistance,inductance and capacitance related to 1^{st} order resonance and R_2, L_2, C_2 represents the same related to higher order resonance. M is the mutual inductance responsible for coupling between resonance. Z_1 and Z_2 are impedances due to two circuits respectively. Whereas Z_0 and Z_s represent the impedances of free space and silicon substrate respectively.

represented by two RLC circuits, where R_1, L_1, and C_1 correspond to the 1^{st} resonance

and R_2, L_2, and C_2 correspond to the 2^{nd} resonance. These two resonances are coupled through the mutual inductance M. The circuit model of a unit cell under the transmission line theory is shown in Fig.2.4. The intrinsic impedance (Z_0) of this circuit can be given as

$$Z_0 = \frac{120\pi}{\sqrt{\varepsilon_i}\left[\frac{w}{d} + 1.393 + 0.667ln\left(\frac{w}{d} + 1.444\right)\right]} \tag{2.1}$$

The impedance of this circuit model Z_s can be written as

$$Z_s = \frac{Z_1 Z_2 + \omega^2 M^2}{[Z_1 + Z_2 - 2j\omega M]} \tag{2.2}$$

Where ω and M represents angular frequency and mutual inductance respectively. Z_1 and Z_2 correspond to the impedances due to 1^{st} and 2^{nd} LC circuits respectively. These impedances can be given as

$$Z_1 = \frac{L_1/C_1}{j\left(\omega L_1 - \frac{1}{\omega C_1}\right)} \quad , \quad Z_2 = \frac{L_2/C_2}{j\left(\omega L_2 - \frac{1}{\omega C_2}\right)} \tag{2.3}$$

The normalized transmission coefficient $t(\omega)$, of this transmission line-RLC circuit model will follow the normal form as

$$t(\omega) = \frac{2Z_s}{Z_0 + Z_s} \tag{2.4}$$

Where Z_0 and Z_s are the impedances of the substrate and free space, respectively. We have used Eq.2.4 to calculate the waveguide transmission and predict anti-resonance frequencies of resonant modes. Using this model, we calculated terahertz transmission for the case of s=600 µm, 500 µm and predicted that the anti-resonance frequencies matches with numerical findings for certain specific values of inductance, capacitance and resistance, which are given in Table 2.1. The values of R, L, C, and M are obtained by fitting the transmission amplitude with the simulations. Here mutual inductance value is $96\ fH$ and turns out to be fixed, indicating that coupling between two consecutive grooves is the same. In Fig.2.4(a & b), one can note that the transmission calculated from the transmission line model and the transmission obtained by numerical simulation have different line widths. The width of the resonance in a numerical simulation

Parameters	s=600 μm	s=500 μm
Resistance,R_1 (Ω)	4.0	2.9
Inductance, L_1 (fH)	60.5	38.1
Capacitance, C_1 (pF)	5.8	5.65
Resistance,R_2 (Ω)	0.5	0.3
Inductance, L_2 (fH)	12.0	9.9
Capacitance, C_2 (pF)	15.5	11.0

Table 2.1: Different parameters used in TL-RLC circuit for pyramidal corrugation.

can be attributed to the scattering, diffraction, and dispersion loss experienced by the wave as it propagates along with the corrugated pattern. These losses have a significant effect on signal loss and thus on the width of the spectrum. Losses due to these effects cannot be accurately included in the transmission line model. This model describes a simple yet useful semi-analytical approach to account for resonant behavior, with a focus primarily on anti-resonance frequencies. The anti-resonance frequency corresponds to a sharp drop on the high frequency side of each resonance. Interest in anti-resonance frequencies arises because they are related parameters, not frequencies associated with the resonance peak [123, 124].

Further, we examine the field profiles of the terahertz modes supported by the proposed pyramidal structured plasmonic THz waveguide configuration. The results are shown in Fig.2.5 for two different planes i.e. zy-plane and xy-plane. Fig.2.5(a & b) represent the field profile at the resonant frequencies of the fundamental mode i.e. 0.27 THz in zy-plane and xy-plane respectively, however Fig.2.5(c & d) represents the field profile of the 2^{nd} mode at 0.47 THz in the same plane. The structure exhibits strong confinement of all modes as it propagates along the waveguide. Fields are strongly confined at the resonant frequency and behaviour of the modes are apparent from the profile of modes.

2.5 Quality factor and sensor characteristics of the modes

Next, we examine the quality factor(Q) of the fundamental and higher-order modes of the proposed plasmonic waveguide. The quality factor is one of the very important

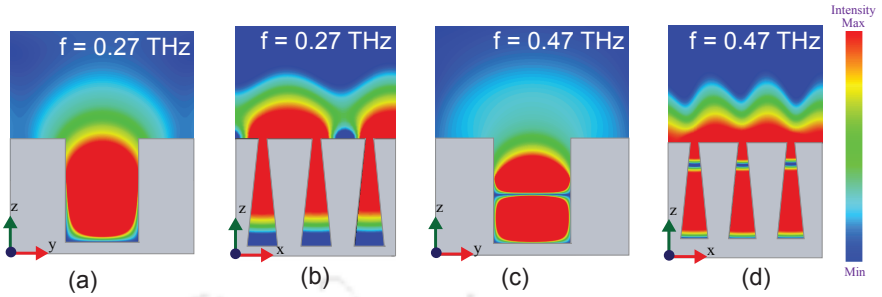

Figure 2.5: The field profiles of the pyramidal structured plasmonic waveguide for different THz modes i.e. a) Fundamental mode in zy -plane; b) Fundamental mode in zx-plane plane. It represents electric field profile in the pyramidal groove at resonance frequency 0.27 THz; c) 2^{nd} mode in zy-plane; d) 2^{nd} mode in zx-plane It represents electric field profile in the pyramidal groove at resonance frequency 0.47 THz.

parameters to analyse the quality of the modes and the narrowness of the resonance. The high Q-factor modes along with strong electric field confinement could be significant in the ultrasensitive sensing applications. The quality factor of a mode is defined as the ratio of resonance frequency (f_r) and its band width (Δf). The band width is basically the full width at half maxima of the resonance. We have calculated the quality factor for the fundamental and high order resonance of our waveguide for different transverse lengths (s) of the pyramidal grooves. The results have been shown

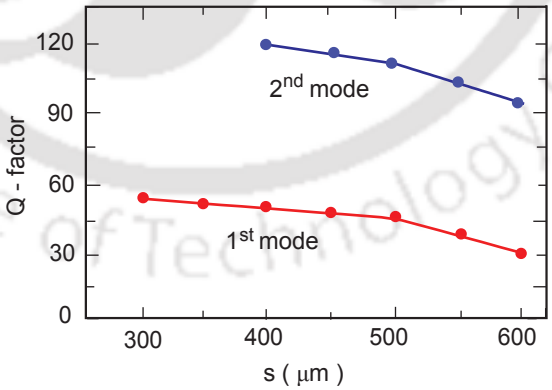

Figure 2.6: Numerically calculated Q-factor of the Fundamental mode and higher order modes of plasmonic waveguide having Pyramidal grooves.

in Fig.2.6. The red trace shows the quality factor for the fundamental mode, however blue trace represents for 2^{nd} order mode. It may be noted that the quality factor (Q) of the fundamental mode decreases as the length of pyramidal grooves is increased. For s = 300 μm, the Q-value is calculated to be 47.6, however it decreases to 33.8 as the

length of the groove is increased to s = 600 µm. A similar trend is observed in the case of 2^{nd} order mode. For 2^{nd} order mode, as the length of the groove is increased from s = 400 µm to s = 600 µm, the quality factor is decreases 120.4 to 95.2 value. Our numerical observations also reveal that the Q-value of the 2^{nd} order mode is higher as compared to the fundamental mode owing to its narrow line width.

In order to examine the refractive index sensing capability of the modes in the proposed plasmonic waveguide, we filled pyramidal grooves with the analytes of different refractive indices. We measured the frequency shift of the fundamental as well as 2^{nd} order mode with respect to the change in refractive index of the analyte. Precisely, we focused on a change in the anti-resonant frequency of the mode when grooves are filled with analyte with respect to the intrinsic anti-resonant frequencies (i.e. without any analyte). For our study, we varied refractive index values of the analyte as (n) = 1, 1.2, 1.4, 1.6, 2. The results of frequency shift versus refractive index are shown in Fig.2.7(a). When the refractive index of the analyte is increased, we observe a linear shift in the anti-resonance frequencies of the fundamental as well as 2^{nd} order mode. The shift in frequency is observed because of the interaction between the highly confined electric field of the modes at the surface and the analyte present there. Further, we

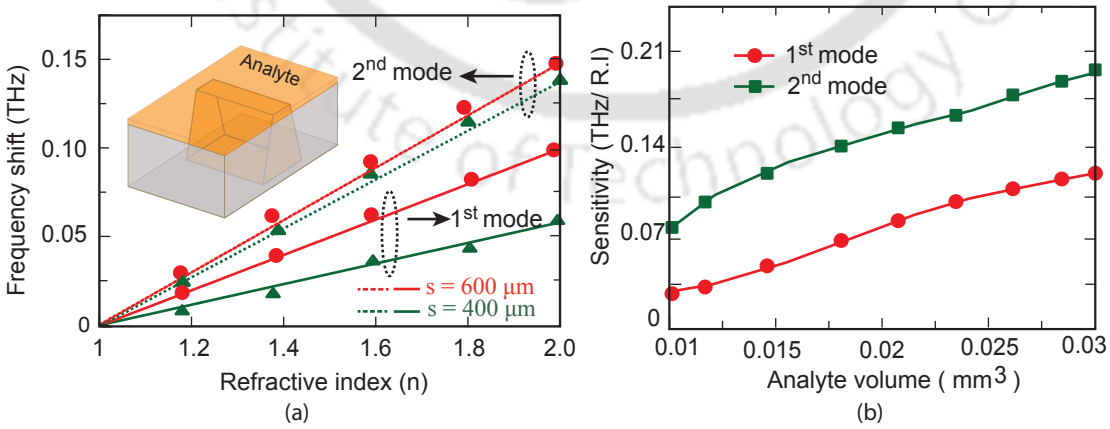

Figure 2.7: a) The variation of frequency shift of the fundamental mode & higher order mode versus refractive index of the polyimide substance for the plasmonic terahertz waveguides b) Numerically calculated variation of sensitivity versus quantity of the analyte filling the pyramidal grooves.

examine the sensitivity of the modes supported by our waveguide in order to compre-

hensively understand its sensing performance. The sensitivity is calculated by measuring frequency shift (Δf) with respect to the change in refractive index (Δn) for a given amount of analyte, and calculating the slope $(\frac{\Delta f}{\Delta n})$ of this variation. Fig.2.7(b) shows the plot of sensitivity of the modes versus volume of analyte filled in the grooves. We have varied refractive index as (n) = 1, 1.2, 1.4, 1.6, 2.0 to calculate correspond frequency shift for several different volumes of analytes for groove length (s) = 600 µm. From the results, it is clear that sensitivity increases with the analyte quantity and this follows for fundamental as well as higher order modes. It may be observed from the plot that the 2^{nd} order mode results in higher sensitivity compared to the lower order mode. For 0.03mm^3 of the analyte, the sensitivity for 2^{nd} modes is calculated to be $\frac{\Delta f}{\Delta n} = 0.19\ THz/RIU$, whereas for the same quantity of analyte, the sensitivity of 1^{st} order modes turns out to be $0.11\ THz/RIU$.

2.6 Discussions

In summary of this work, we have examined the sensing capability of a planar plasmonic terahertz waveguide comprising of subwavelength scale pyramidal shaped structures. We first examined dispersion relations of the fundamental and higher-order modes to ensure the plasmonic response of the proposed waveguide. The transmission response of the waveguide is examined for different transverse lengths of the corrugations. We observed that as the length of grooves is increased, the anti-resonant frequency of the fundamental and higher-order modes get red-shifted. We have further calculated the quality factors of the modes and examined their dependence on the transverse length of the structures. The quality factor decreases as the length is increased. For the same set of parameters, the quality factor is observed to be higher for 2^{nd} order mode compared to the fundamental mode. The high Q-factor modes are important to build highly sensitive refractive index sensors. The sensing capability of the fundamental and higher order modes is examined and compared by filling groves with materials of different refractive indices. As the refractive index of the analytes

is increased, the resonances are found to be red-shifted. For a fixed value of analyte and groove parameters, the shift is higher for 2^{nd} modes as compared to the 1^{st} mode. We further calculate the sensitivity of the modes for varying quantity of analyte. It is observed that the 2^{nd} order mode results in higher sensitivity compared to the lower order mode. For $0.03\ mm^3$ of the analyte, the sensitivity for 2^{nd} modes is calculated to be $0.19\ THz/RIU$, however for the same amount of analyte, it turns out to be 0.11 THz/RIU for the 1^{st} order mode. The present study not only compares the different mode's ability to sense analyte, but also depicts better sensing capability than the earlier demonstrate transmission and waveguide approaches. The study could be significant in the construction of sensors and selectively choosing a guided wave mode to achieve high sensitivity in thin film refractive index terahertz sensors.

3

Near field coupling between resonators in a THz plasmonic waveguide

Contents

This chapter describes the near-field coupling of surface plasmon waves from asymmetric resonators in a THz plasmonic waveguides. Here the asymmetric shape resonators are placed in close proximity and the waveguide transmission as well as electric field profiles are examined to understand the near field coupling behaviour.

3.1 Introduction

The plasmonic waveguide has the ability to support highly confined surface modes in a corrugated metal surfaces. This can be important in a variety of applications, from engineering to the medical field. At terahertz frequencies, one can build a highly efficient refractive index sensor by patterning the metal surface with periodic corrugations, as described in Chapter 2. In order to use plasmonic guided wave devices in real-world applications, it is required to explore more optimal designs including internal corrugations. Plasmonic waveguide resonators in near field configurations have a variety of effects such as mode hybridization, induced absorption, broadband modulation, and electromagnetically induced transparency (EIT). When two corrugated structures are close enough to each other, they interact via magnetic and electric field lines, giving rise to novel phenomena and exciting applications that may not exist in a traditional plasmonic waveguide. Further, near field coupling between asymmetric resonators can provide additional degrees of freedom for adjusting the dispersion characteristics of the surface plasmon. A strong near-field coupling between the resonances of an asymmetric resonator can lead to support mode interference. As a result, various applications are possible depending on the effects mentioned above. By controlling the near-field coupling of the resonances, such effects can be observed without changing the physical parameters. In the design of plasmonic waveguides for on-chip communication devices, near-field coupling of resonances and their manipulation in planar configurations can be important. Therefore, there is a strong need to investigate near-field coupling between asymmetric resonators and proceed with research to understand the underlying coupling mechanism.

In this work, we examine near field coupling of a surface plasma wave in a planar terahertz plasmonic waveguide comprising of a one-dimensional array of periodically arranged asymmetric rectangular apertures placed along the transverse direction. Through the excitation of both the apertures simultaneously, we study near field coupling of surface plasmons from the asymmetric size resonances. The chapter is organized as follows: First, we describe the proposed waveguide geometry and examine the dispersion properties of a rectangular aperture structure to ensure a plasmonic response. After that, we numerically investigate the transmission spectra for different types of apertures to explore near field coupling of surface plasmons in the proposed waveguide along with the electric field profiles. Further, we employ a theoretical model based on a three level plasmonic system to understand the coupling mechanism in conjunction with the proposed geometry. The coupling strength is examined by varying the gap between the asymmetric resonators and the resultant absorption window is modulated by changing the aperture dimensions. Finally, we summarize the results in the discussion.

3.2 Schematic of waveguide comprising asymmetric resonators

The schematic illustration of the proposed terahertz plasmonic waveguide is shown in Fig. 3.1. The waveguide is made up of periodically patterned rectangular apertures in a thin sheet of metal. The unit cell of the waveguide structure is considered to be comprising of two sub-wavelength scale rectangular apertures with different lengths placed adjacent to each other along the transverse direction. The different structure parameters of the waveguide geometry are shown in the magnified view of Fig. 1. The l_1 and l_2 are lengths of the aperture 1 (AP1) and aperture 2 (AP2), respectively. The w and h represent the width and depth of the apertures. The periodicity and gap between the apertures are represented by 'p' and 'g', respectively. The periodicity, width, and depth remain fixed in our entire analysis. The waveguide is excited with terahertz broadband signal at the one end and the terahertz surface plasmon polaritons prop-

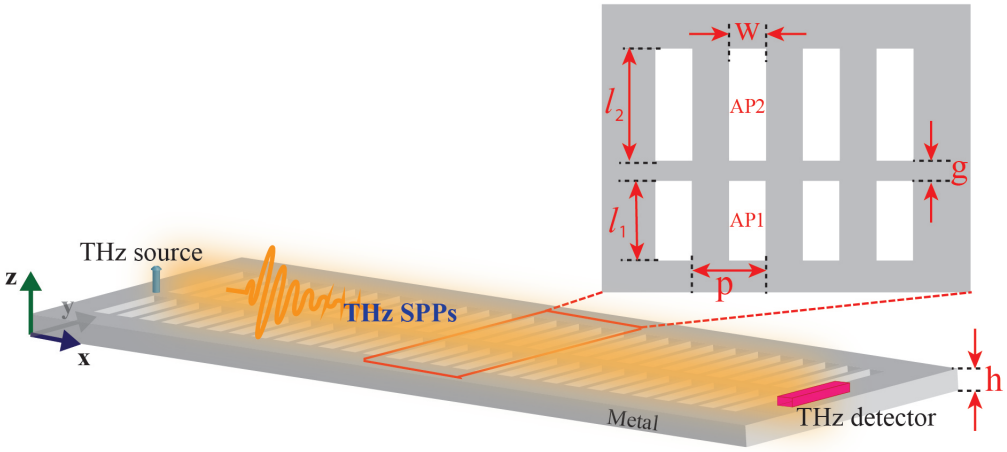

Figure 3.1: Schematic of planar plasmonic waveguide geometry: 3-D view of proposed waveguide design comprising of a one-dimensional array of periodically arranged perforated rectangular apertures. Each unit cell is comprised of two rectangular apertures placed adjacent to each other along the transverse direction. The geometrical parameters of the rectangular apertures are as follows: $w = 150\ \mu m$, $p = 250\ \mu m$, $h = 500\ \mu m$, $g = 50\ \mu m$, $l_1 = 500\ \mu m$ and $l_2 = 550\ \mu m$.

agating along the corrugated pattern are detected at the other end of the waveguide. The proposed terahertz planar plasmonic waveguide can be fabricated as discussed in previous Chapter 2. The fabricated samples can be characterized using the technique of terahertz time-domain spectroscopy. In this setup, a femtosecond laser with a repetition rate of 80 MHz, and temporal pulse duration of 100 fs may be used as the optical source in the experiment. The optical radiation is divided into 80:20 for use as the optical pump and probe beams, respectively. The optical pump beam is used to generate terahertz waveforms via a Lt-GaAs based photoconductive emitter. The terahertz waveforms produced by the emitter are collimated and collected via the parabolic mirrors and is normally incident onto the coupler. The coupler couples the incident broadband terahertz pulses to the waveguide pattern. The information-carrying signals i.e. THz surface plasmon polaritons (SPPs) are detected by the terahertz receiver i.e. a ZnTe followed by a differential detection scheme [125]. It helps to minimize the background noise signal. The transient current through photodetector is amplified and measured using a lock-in amplifier. The data of the lock-in amplifier can be recorded on the computer via a Labview program. The efficient coupling of free-space terahertz waveform to the corrugated pattern is very crucial in experiments. For coupling, one

may use a semi-circular or few micron dip rectangular groove. These techniques have been previously used by Kumar et. al. [118, 119]] in experimental realization. The metal behaves as perfect conductors at terahertz frequencies, and therefore material losses can be considered to be negligible. However, the terahertz surface plasmons experience scattering and diffraction losses as they propagate along the waveguide.

3.3 Dispersion properties of the waveguide

To ensure the plasmonic response of the proposed planar waveguide geometry comprising apertures, we first numerically examine the dispersion properties of fundamental guided mode supported by the waveguide corresponding to aperture of different lengths. We used the technique of finite element Eigenmode solver in commercially available Computer Simulation Technology (CST) microwave studio software. To calculate dispersion relations, the periodic boundary condition is assumed along the direction of propagation and absorbing layers are considered along the transverse direction. We have assumed metal to be a perfect electrical conductor (PEC) owing to its high conductivity at terahertz frequencies. The dispersion relations for rectangular aperture of lengths (l) = 500 μm, 525 μm, 550 μm, and 575 μm are depicted in Fig. 3.2 with different colors. The black color straight line corresponds to the light line. The dispersion curves initially monotonically increase with the wavenumber and later on, saturate at different frequencies at the boundary of the first Brillouin zone. At saturation frequency, the group velocity of fundamental guided mode is zero. The saturation value indicates the maximum allowed frequency for the excitation of surface plasmons in the proposed configuration and is also termed as cut-off frequency. The dispersion curves saturate at frequencies 0.30 THz, 0.285 THz, 0.27 THz, and 0.26 THz corresponding to apertures of lengths 500 μm, 525 μm, 550 μm, and 575 μm, respectively. The increase in aperture length (l) causes the dispersion curve to redshift and saturate to a lower cut-off.

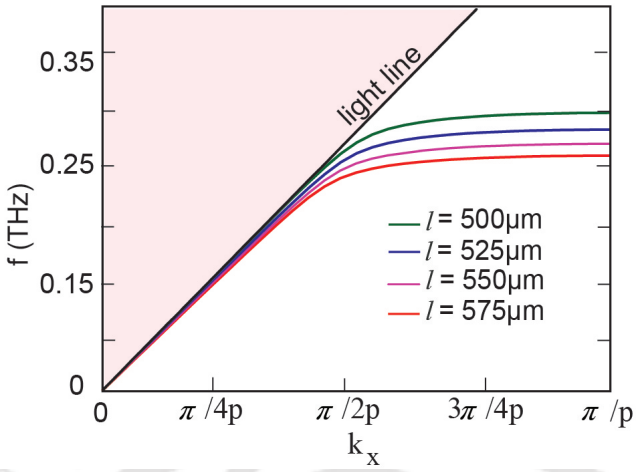

Figure 3.2: Numerically calculated dispersion properties of the fundamental guided mode in the proposed plasmonic waveguide for different length of single rectangular aperture i.e. l = 500 μm, 525 μm, 550 μm and 575 μm. The other parameters are: w = 150 μm, p = 250 μm, h = 500 μm.

3.4 Numerically simulated waveguide transmission

Next, we study the near field coupling of surface plasmons and the induced absorption window in the proposed waveguide configuration. To perform this numerical study and understand the related coupling, we designed three waveguides comprising an array of apertures with (i) AP1 only, (ii) AP2 only, and (iii) both AP1 and AP2 placed alongside in transverse direction with gap 'g'. We have considered the length of two rectangular apertures as l_1 = 500 μm and l_2 = 550 μm, and the gap between the two apertures g = 50 μm. In numerical simulations, we excited the plasmonic waveguide with a single cycle terahertz waveform. The signal coupled to the waveguide resonators propagate along with the corrugated pattern and detected at the other end of the waveguide in time domain form, which is transformed into frequency domain waveform using Fast Fourier Transform (FFT). The waveguide geometry is simulated for the z-polarized incident wave under open boundary conditions in all planes. First, we examine waveguide transmission amplitude of the proposed waveguide comprising of periodically arranged AP1 and then AP2 only. The transmission amplitudes of fundamental modes supported by the two plasmonic waveguides with only AP1 and then only AP2 are shown in Fig. 3.3(a) and (b) respectively. For the combined struc-

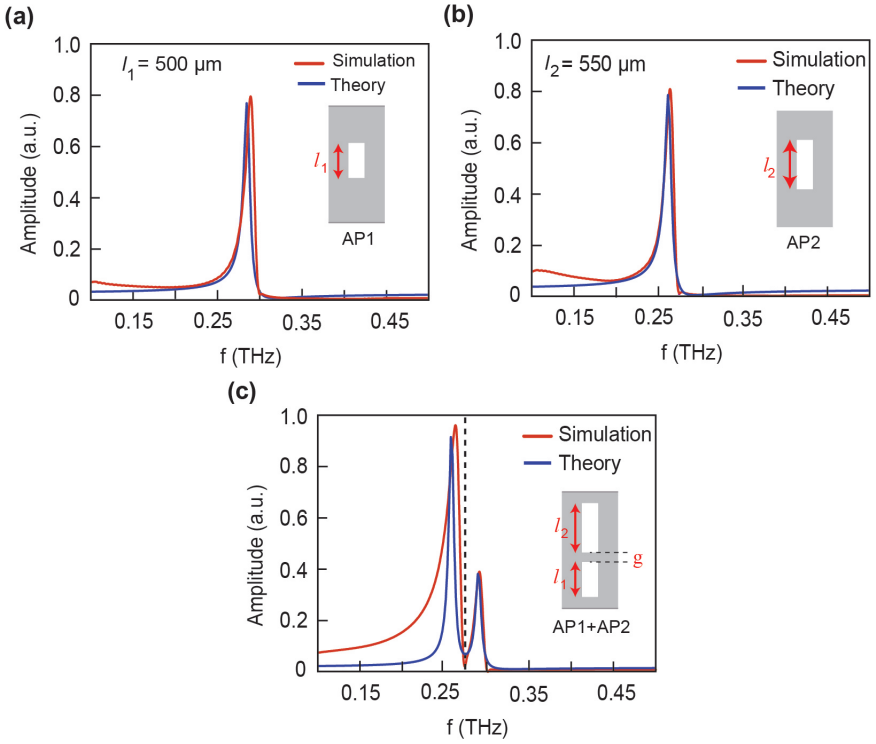

Figure 3.3: Transmission spectra of the plasmonic waveguide for different parameters $w = 150$ μm, $p = 250$ μm, $h = 500$ μm: (a), (b), (c) represent transmission amplitudes for periodically arranged AP1, AP2, and both AP1+AP2 with $g = 50$ μm, respectively.

tures i.e. AP1 and AP2, the results are shown in Fig. 3.3(c). The red traces represent the transmission amplitudes of the waveguide from numerical simulations while the blue traces correspond to the theoretical model [126].

We have used a theoretical model based upon the three-level plasmonic system, which we have discussed in detail in the next section. From Fig. 3.3(a) and (b), it may be noted that they exhibit single resonance frequency with anti-resonance frequencies at f = 0.3 THz and f = 0.27 THz corresponding to l_1 = 500 μm and l_2 = 550 μm, respectively. The frequencies can be verified from the Eigen frequency equations of the rectangular cavity given by, $\omega = [(m/l)^2 + (n/w)^2 + (p/h)^2]^{1/2}$, where l, w, and h are length, width and depth of the apertures. The m, n, and p are integer values. For m=1, n =0 and p =0, one can verify that frequencies of the modes corresponding to l_1 = 500 μm and l_2 = 550 μm are 0.3 THz and 0.27 THz, respectively. These values matched with the anti-resonant frequencies of the plasmonic modes appearing in Fig. 3.3(a) and (b).

It may be noted that the anti-resonance frequency is quite important in terahertz plasmonic waveguide transmission spectrum since it occurs due to the Fano-interference between the discrete spectrum and continuum spectrum [127]. When these resonators placed along the transverse direction (y-axis in the schematic), are brought in the near field configuration and excited with incident terahertz simultaneously, a narrow absorption window (dip at 0.275 THz) is introduced as shown in Fig. 3.3(c). This absorption window is believed to be caused by the destructive interference of the two bright resonators. In our case, both the resonators act as bright mode of frequencies (ω_1) and (ω_2), as they are directly excited with incident terahertz. In the coupling state, we also observe a slight shift in the resonance frequencies as compared to the transmission spectrum of the single aperture. It is due to the mode hybridization effect of the resonators. In numerical simulations, we have considered frequency resolution of 20 GHz to obtain transmission spectra. The corresponding temporal scanning range of 314 ps can be calculated by [128],

$$T = \frac{2\pi}{\delta\omega}$$

where, $\delta\omega$ is the frequency resolution.

In case of theoretical modelling, a frequency resolution of 10 GHz has been used to obtain transmission spectra, which corresponds to temporal scanning range of 628 ps. The values of frequency resolution and corresponding scanning range in numerical simulation and theoretical modelling are quite feasible experimentally by using available delay stages [129].

To understand the coupling state between the resonators in the plasmonic waveguide, we examined the electric field profiles in the coupled state at three different frequencies 0.30 THz, 0.27 THz, 0.275 THz. These frequencies correspond to the two cut-off frequencies of the resonances and the absorption dip in the spectrum of the coupled system as indicated in Fig. 3.4(a) - (c). The results are shown in Fig. 3.4(a) - (c). For 0.3 THz, only one resonator of length l_1 i.e. AP1 is excited as this frequency corresponds to the resonance frequency of AP1 resonator however, at 0.27 THz, the only resonator

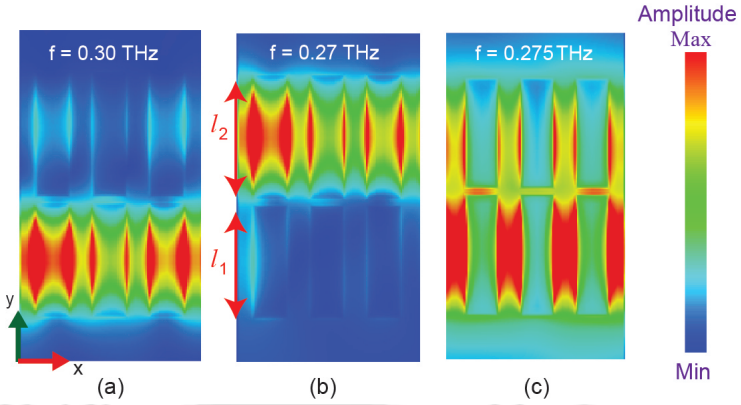

Figure 3.4: (a) – (c) represent electric field profiles of the waveguide in x-y plane at z = 10 μm at frequencies i.e. 0.3 THz, 0.27 THz, and 0.275 THz, supported by AP1, AP2, and both AP1 & AP2, respectively.

of length l_2 i.e. AP2 is excited. At 0.275 THz which is believed to appear from the coupling of two resonators, as both the resonators are excited, which is evident from Fig. 3.4(c).

3.5 Theory

To validate our numerical findings and get an insight into the physical mechanism involved in the surface plasmon-induced absorption via the coupling of resonators, we employ a three-level plasmonic model [126]. In our case, waveguide supports two plasmonic modes at slightly two different frequencies. They are coupled via a strong electric field profile in the near field configuration. Since the two resonators are simultaneously excited directly by the incident terahertz, they are termed as the bright resonators. Hence, both bright state, $\langle a| = \tilde{a}\exp^{i\omega t}$ and $\langle b| = \tilde{b}\exp^{i\omega t}$ strongly couples with the incident electric field, $E_0 = E_0\exp^{i\omega t}$. In this situation, the amplitude of two radiative resonant modes can be expressed in terms of coupled Lorentz oscillators as

$$\begin{pmatrix} \tilde{a} \\ \tilde{b} \end{pmatrix} = \frac{1}{(\delta + i\gamma_a)(\delta + i\gamma_b) - \kappa^2} \begin{pmatrix} (\delta + i\gamma_b) & -\kappa \\ -\kappa & (\delta + i\gamma_a) \end{pmatrix} \begin{pmatrix} -GE_0 \\ -GE_0 \end{pmatrix} \tag{3.1}$$

where $\tilde{a}$ and $\tilde{b}$ are induced THz field amplitude corresponding to the two resonators i.e. AP1 and AP2 respectively. The two modes have adjacent resonance frequencies

ω_1 and ω_2, such that $\delta = \omega - \omega_1 = \omega - \omega_2$ is very small in Eq. (3.1). γ_a and γ_b are assumed to be a damping factor of the modes, which is much smaller than the resonance frequencies; E_0 is the amplitude of the incident THz electric field and ω is the corresponding frequency of the incident THz signal; κ is the coupling coefficient between the two modes; G is a geometric parameter which describes the coupling of resonators with the incident THz electric field.

From Eq.(3.1), the field amplitude of the 1^{st} mode can be expressed as,

$$\tilde{a} = \frac{-GE_0\left(\delta + i\gamma_b\right) + \kappa GE_0}{\left(\delta + i\gamma_a\right)\left(\delta + i\gamma_b\right) - \kappa^2} = \frac{GE_0\left[\kappa - \left(\omega - \omega_2 + i\gamma_b\right)\right]}{\left(\omega - \omega_1 + i\gamma_a\right)\left(\omega - \omega_2 + i\gamma_b\right) - \kappa^2} \tag{3.2}$$

Similarly, for the 2^{nd} mode, it is given by,

$$\tilde{b} = \frac{GE_0\left[\kappa - \left(\omega - \omega_1 + i\gamma_a\right)\right]}{\left(\omega - \omega_1 + i\gamma_a\right)\left(\omega - \omega_2 + i\gamma_b\right) - \kappa^2} \tag{3.3}$$

The transmission coefficient of the plasmonic waveguide can be written as:

$$T = \left|\frac{\tilde{a}}{E_0}\right|^2 + \left|\frac{\tilde{b}}{E_0}\right|^2$$

$$T = |a|^2 + |b|^2 \tag{3.4}$$

It is important to mention that the resonance frequencies in the waveguide transmission appear because of Fano interference of the discrete and continuum spectra, which causes the resonances to be asymmetric. In order to account for the asymmetric nature of the resonances in the theoretical model, we introduce Fano-parameter (qF) in the transmission spectrum given in Eq.(3.4) [8]. It is added in such a way that if qF is zero, we can get the original transmission spectra from the analytical model. The Fano-parameter (qF) can be given by the following expression [130],

$$qF = \frac{2(\omega_0 - \omega_r)}{\Gamma} \tag{3.5}$$

where, ω_0 and ω_r are the anti-resonant and resonant frequencies respectively while Γ is the bandwidth of the transmission spectra. Therefore, Eq.(3.4) can be modified as

$$T = |a + qF|^2 + |b + qF|^2 \tag{3.6}$$

We use Eq.(3.6) to separately calculate the THz transmission coefficients for three different waveguide configurations comprising a one-dimensional array of apertures: AP1 only, AP2 only and the combined structures i.e. AP1+AP2. Theoretically calculated values of transmission amplitudes are found to best fit the corresponding numerically obtained transmission amplitudes for the parameters given in TABLE 3.1. The theoretical and simulation transmission spectra are shown together with blue and

Resonator type	G (THz)	κ (THz)	γ_a (THz)	γ_b (THz)	qF
AP1	0.15	0	0.52	0.027	1
AP2	0.15	0	0.52	0.027	1.2
AP1 & AP2	0.12	0.035	0.023	0.025	0.375

Table 3.1: Specific parameters for the theoretical modeling of near field coupling

red traces in Fig. 3.3(a)-(c). From the figure, it may be noticed that the numerically obtained resonant modes from simulations are narrower in case of a single aperture case (AP1 or AP2) as compared to the coupled system apertures (when both AP1 & AP2 are present). It is due to the fact that the terahertz surface plasma polaritons experience scattering, dispersion, and diffraction losses, which is believed to be more prominent in the case of double aperture than the single aperture. These losses contribute to the broadening of resonances in transmission spectra. In theoretical modelling, these losses are not present and therefore, the spectrum appears to be narrower as compared to the simulations. The primary focus in theoretical modelling has been observed the anti-resonance frequencies of the modes in conjunction with the numerical observations as they are caused by the Fano-interference of the discrete and continuum states in the proposed plasmonic waveguide. Further, in Table 3.1, one can notice that the value of the coupling coefficient parameter is zero for AP1 and AP2 separately, since

the resonators are excited separately i.e. in the absence of other aperture. Furthermore, it can be observed that the value of the geometric parameter decreases when both the resonators are present in the near field region. This occurs due to the coupling between the two bright resonators, which causes a decrease in the coupling of the incident field with mode-1 and mode-2.

3.6 Modulating the waveguide transmission

Further, we investigate the modulation of the absorption window by varying the coupling between the two resonators placed in the transverse direction of the plasmonic waveguide. This is accomplished by changing the gap 'g' between the two resonators. The numerical results of waveguide transmission spectra depicting the modulation with respect to the gap variation are shown in Fig. 3.5(a). To study this

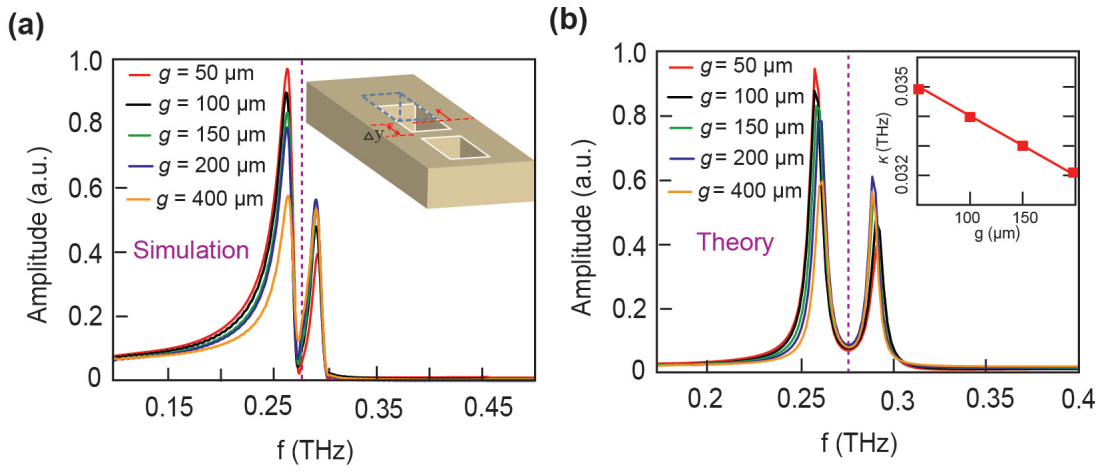

Figure 3.5: THz transmission spectra for different gap between two rectangular apertures with length of AP1 (l_1) = 500 μm and AP2 (l_2) = 550 μm to modulate surface plasmon induced absorption. The other parameters are as follows: w = 150 μm, p = 250 μm, h = 500 μm (a) From numerical simulation. Inset shows schematic of varying the gap between two apertures along the transverse direction. (b) From theoretical modeling. Inset shows the variation of coupling coefficient with increasing gap (g) value between two apertures.

variation, we assumed, l_1 = 500 μm, l_2 = 550 μm, w = 150 μm, p = 250 μm, h = 500 μm, while the gap is varied from 50 μm to 400 μm. For the case of g = 50 μm, we observe a narrow dip at f = 0.275 THz, indicating a change in the dispersion properties and an absorptive window in the spectrum. This is believed to be caused due to destruc-

tive interference between the two resonant modes. As the gap between the resonators is increased, the amplitude of 1^{st} resonance decreases and there is a corresponding increase in the amplitude of 2^{nd} resonance. This reflects a coupling between the two resonances. The transmission spectra for different values of gap (g) are represented by different colors in the plot.

To order to elucidate the numerical findings and understand the coupling mechanism, we employed theoretical modeling to calculate the transmission spectra as discussed in the above section. The transmission coefficient from the modeling is plotted in Fig. 3.5(b) for different gap (g) values between the resonators. For better view of modulation of absorption window, we are showing transmission spectra within small frequency range. Different color traces correspond to different values of gap (g). From the results, it is evident that the narrow absorption window peak at 0.275 THz for the case, g = 50 μm, and matches with the simulation results. The window in Fig. 3.5(b) can be modulated for a specific set of parameters shown in TABLE 3.2, corresponding to the given 'g' values.

Gap between AP1 & AP2 (μm)	γ_a (THz)	G (THz)	κ (THz)	γ_b (THz)	qF
50	0.12	0.035	0.023	0.025	0.375
100	0.17	0.034	0.024	0.023	0.375
150	0.22	0.033	0.025	0.022	0.375
200	0.27	0.032	0.026	0.021	0.375
400	0.37	0.028	0.027	0.02	0.375

Table 3.2: Parameters for the theoretical fit for various gap "g".

From the table, one can notice that as the gap g increases, the value of the geometric parameter (G) increases whereas, the coupling coefficient between the two resonators, and hence the modes decreases. It is apparent that with an increase in gap (g), the coupling strength between the two resonators of the combined system decreases. The variation of the coupling coefficient with the increasing gap (g) between resonators is plotted in the inset of Fig. 3.5(b). It shows a monotonic decrease in the coupling

coefficient (κ) with respect to the increase in the gap (g) value.

Next, we study modulation of the absorption window by varying the length of the AP2 (l_2) in the waveguide comprising both AP1 and AP2. The length is varied from 500 µm to 600 µm keeping the following parameters fixed: l_1 = 500 µm, gap (g) = 50 µm, depth (h) = 500 µm, width (w) = 150 µm, and periodicity (p) = 250 µm. The results are shown through the transmission spectra depicted in Fig. 3.6(a). The different color traces represent transmission spectra for different lengths, l_2. From the figure, it can be noticed that, when the length of AP2 is l_2 = 500 µm, we get only one resonance

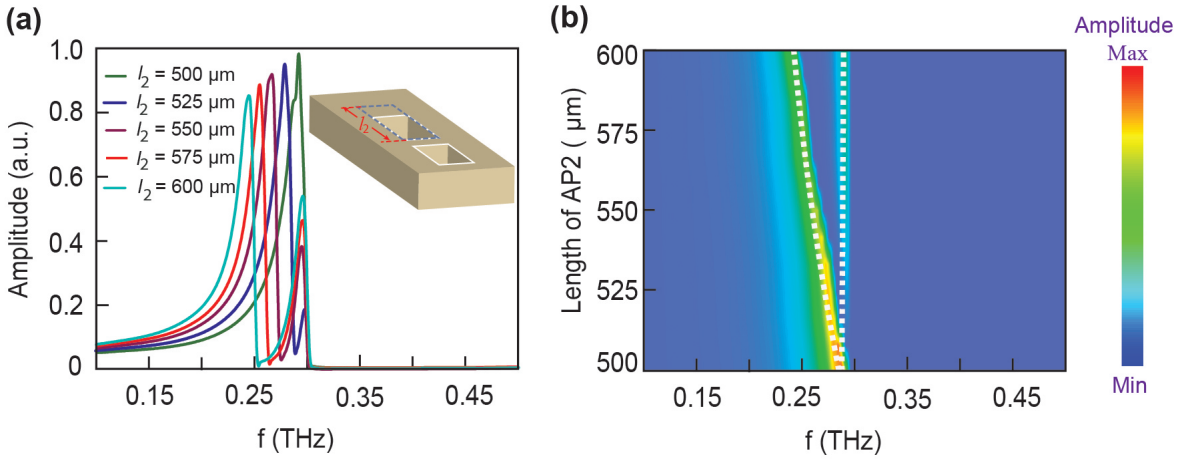

Figure 3.6: Modulation of absorption window for fixed parameters of plasmonic waveguide: w = 150 µm, p = 250 µm, h = 500 µm, g = 50 µm, l_1 = 500 µm.: (a) Numerically simulated transmission spectra for different length of AP2 (l_2). Inset shows schematic of varying length of AP2. (b) Contour plot of numerically simulated THz transmission results for different length of AP2 in Fig. 3.5(a). Color bar shows the amplitude of the transmission results.

mode with anti-resonance frequency at 0.3 THz. The frequency of the resonant mode can be calculated from the Eigen frequency equation of the rectangular cavity given by, $\omega = [(m/l)^2 + (n/w)^2 + (p/h)^2]^{1/2}$. When both l_1 and l_2 are the same, then we will get $\omega_1 = \omega_2$. As we increase l_2, then the absorption window gets wider as the corresponding frequency ω_2 gets red-shifted. In order to get a comprehensive picture of the dependence of the structural parameters on the absorption window of the waveguide transmission, we present a contour plot for the variation in the frequency with the aperture length of l_2. This is shown in Fig. 3.6(b). In this figure, the frequency and length 'l_2' are shown along the x and y-axis, respectively while the amplitude of

the transmission signal is indicated through the color bar. The white color dashed line indicates the position of resonant frequencies with maximum amplitude. It may be observed that for the same length of apertures, we get a single resonance frequency, however as the length of AP2 is varied, we get an absorption window as shown by the two white dashed lines. The effect is useful in the designing and construction of planar terahertz waveguide components, where one needs a desired frequency to propagate.

We further investigate the modulation of absorption window by varying width w_2 of AP2, while keeping the width of AP1 fixed for the coupled waveguide system. The following other parameters remain fixed: w_1 = 150 µm, p = 250 μm, g = 50 µm, l_1 = 500 µm, and l_2 = 550 µm. The width, w_2 is varied as 50 µm, 100 µm, 150 µm, 200

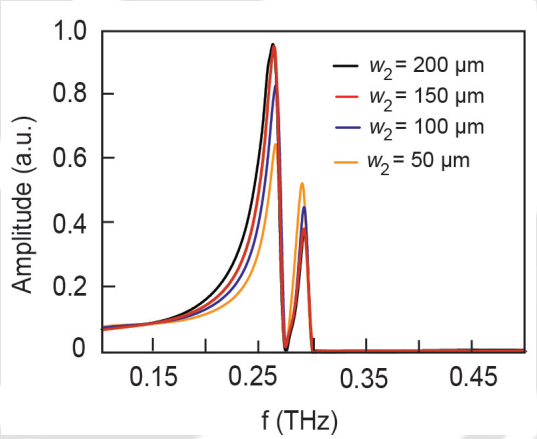

Figure 3.7: Numerically calculated waveguide transmission versus width w_2 of the proposed asymmetrically coupled resonators waveguide. The waveguide parameters are: l_1 = 500 µm, l_2 = 550 µm, w_1 = 150 µm, p = 250 µm, g = 50 µm, and h = 500 µm.

µm. The corresponding results of the waveguide transmission spectra are shown in Fig 3.7. One may note that as we decrease width, amplitude of first resonance on lower frequency side decreases while that of the other mode on higher frequency side, it increases. Therefore, the width of AP2 is crucial in modulating the transmission response.

3.7 Discussions

In summary, we present a terahertz plasmonic waveguide comprising sub-wavelength rectangular apertures of different sizes placed in the near field regime along the trans-

verse direction. To ensure the plasmonic response, we first examine the dispersion properties of the waveguide with the varying length of aperture arranged in one-dimensional array. We observe a red-shift in the resonance frequency of the plasmonic modes with an increase in the length of resonators. When the two resonators are placed closed to each other in the near field configuration, then an absorption window is introduced which can be tuned by structural parameters of the waveguide. The electric field profiles confirm the strong coupling between the resonators. The plasmonic waveguide modes move from coupled to uncoupled state when the gap between the resonators is increased. We employ theoretical modeling to elucidate the numerical findings as well as to draw a physical understanding of the propagation modes of the waveguide. The results are found to match numerical findings for a given set of parameters of the waveguide. Our study provides a thorough understanding of the role of asymmetric resonators in plasmonic waveguide transmission which could be significant in the construction of terahertz modulators, slow light devices, etc. Although this study is carried out in the terahertz regime, it can be pursued in other regions of the electromagnetic spectrum.

4

Plasmon induced transparency (PIT) in a double slot THz waveguide

Contents

This chapter discusses the PIT in a parallel double-slot waveguide configuration at terahertz frequency. The effort is made to actively controls this effect by filling one waveguide slot with dielectric material. A theoretical model has been discussed to understand the underlying mechanism.

4.1 Introduction

Several reports have been published on the Electromagnetically induced transparency (EIT) effect in past few year at frequencies across the entire electromagnetic spectrum. The concept has been explained via coupling between the bright – dark modes or the bright - bright modes from the incident field excitations [131, 132]. In the context of bright-dark modes coupling, Meng et al. have investigated this effect using a polarization independent metamaterial structure consisting a bright split-ring resonator (SRR) and a dark spiral resonator (SR) both experimentally and numerically [133]. They demonstrated the refractive index based sensing application corresponding to the EIT-effect of their proposed metamaterial structure. Additionally, the modulation of EIT effect can be achieved by displacing the resonators. Liu et al. proposed EIT phenomena in a planar plasmonic metamaterial with a pair of split ring resonators (SRRs) as the dark mode while a cut wire as the bright mode [134]. In the context of bright-bright modes coupling, recently Jin et al. theoretically demonstrated the EIT response at optical frequencies due to the coupling between two silver strips serving as the bright modes [135]. A number of other schemes such as optical electric dipole, nanoparticle array and waveguide systems have also been exploited which rely on bright-bright mode coupling. Recently, a lot of interest has been paid in exploring the EIT effect in the waveguide configurations. Xu et al. have experimentally observed a silicon micro-ring resonator coupled to parallel waveguide to realize transparency window by constructive interference [136]. Yannopapas et al. have shown that an array of nanoparticles on dielectric waveguide can be used to obtain the transparency window, which can lead to the reduction in the speed of light [137]. There is another phenomenon

called Plasmon induced transparency (PIT), which is analogous to the EIT-effect. This effect occurs due to the localized plasmons (usually a bright mode) on the metamaterial surface excited due to the incident electromagnetic radiation undergoing destructive interference with another mode of nearly same frequency (bright or dark mode) resulting from the metamaterial constituent placed in closed proximity. In both the effects, one can control the effect depending upon its constituents shape and size. In this context, several more studies on PIT effect in waveguide configuration have been reported using different schemes including multiple resonator and nano-cavities, etc. In order to tune the PIT response, the dimensions of the structures are varied, which is cumbersome process and also limits its potential for active device construction. In order to address this challenge, we use the dielectric material of certain refractive index in an appropriate parallel double slot waveguide configuration. The configuration allows one to modulate the response of PIT effect without change in physical dimensions of the structure.

In this work, we explore the PIT effect in a parallel double slot waveguide configuration which provides an active control of this effect with respect to the dielectric filled in one of the waveguide slots. The terahertz waveguide is composed of two identical rectangular slots in parallel metallic slabs in the transverse direction. One of the slot is filled with a dielectric material such that it supports a different resonant frequency with respect to the empty slot. The interference between the two resonances gives rise to the PIT effect which can be tuned by changing the dielectric material. The chapter is organized as follows: First, we describe the proposed waveguide geometry along with transmission spectra of parallel double slot terahertz waveguide. Next, we examine electric field profiles to ensure PIT-effect. After that, we employ a theoretical model based on coupled harmonic oscillator systems to justify our numerically obtained PIT effect. Then the refractive index of the dielectric material is varied to observe the tunable control of the PIT effect. A comprehensive picture of modulation of the effect with the refractive index is presented through the contour plot. Finally, we summarize the

results in conclusion section.

4.2 Schematic of Terahertz waveguide

The 3-D schematic of the proposed parallel slab terahertz waveguide is shown in Fig. 4.1. The waveguide is comprised of two slots in parallel slabs in the transverse direction. A certain gap is maintained between the slabs for terahertz TM mode propagation. One rectangular slot is filled with a dielectric material and the other one is empty. For simplicity, we have used the terms RS-1 and RS-2 for rectangular resonating slots without dielectric and with dielectric, respectively throughout the study. In the schematic, parameters 'l', 'w' and 'h' represent length, width, and depth of rectangular slots. The parameter 'g' is the gap between the two parallel metallic slabs.

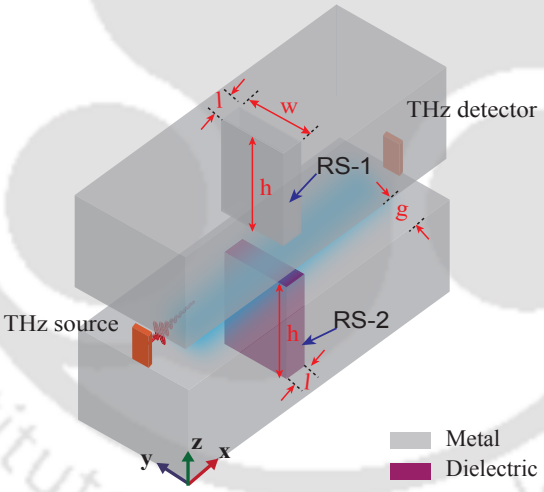

Figure 4.1: Schematic of parallel double slot terahertz waveguide geometry: 3-D view of proposed waveguide design consisting of two parallel metallic slabs which are comprised of identical rectangular slots (RS-1 and RS-2). The gap (g) between two slabs is fixed at 100 µm. The lower slot (RS-2) is filled with dielectric. The geometrical parameters of rectangular slots are as follows: length (l) = 50 µm, width (w) = 600 µm, depth (h) = 200 µm.

The following parameters remain fixed throughout the study: 'l' = 50µm, 'w' = 600µm, 'h' = 200µm, 'g' = 100µm. Terahertz broadband signal is incident at one end of the waveguide. The THz wave propagates along the gap between the two parallel slabs and couples to the rectangular slots configuration. Finally, it is detected at the other end of the waveguide.

4.3 Waveguide transmission

We used the technique of finite element time domain solver in a commercially available Computer Simulation Technology (CST) microwave studio software. In the simulation of the analyzed structure, we have used finite element time domain solver of the CST microwave studio software. We have considered two waveguide ports to obtain transmission spectra: one as the source of terahertz and another one as the terahertz detector. In the solver setting, the mesh size has been set to hexahedral and the accuracy level of the solver is set to – 40 dB, under open boundary condition. We have considered metal to be a perfect electrical conductor (PEC) due to its high conductivity at terahertz frequencies. Single cycle z-polarized incident terahertz beam is allowed to propagate along the gap between two parallel metallic slabs. While propagating it couples to RS-1 and RS-2 and finally, it is probed at the terahertz detector as shown in the schematic in time domain, which is converted into frequency domain using Fast Fourier Transform (FFT). Fig. 4.2 (a) depicts the results of numerically calculated transmission amplitudes of the proposed terahertz waveguide. In the figure, black trace cor-

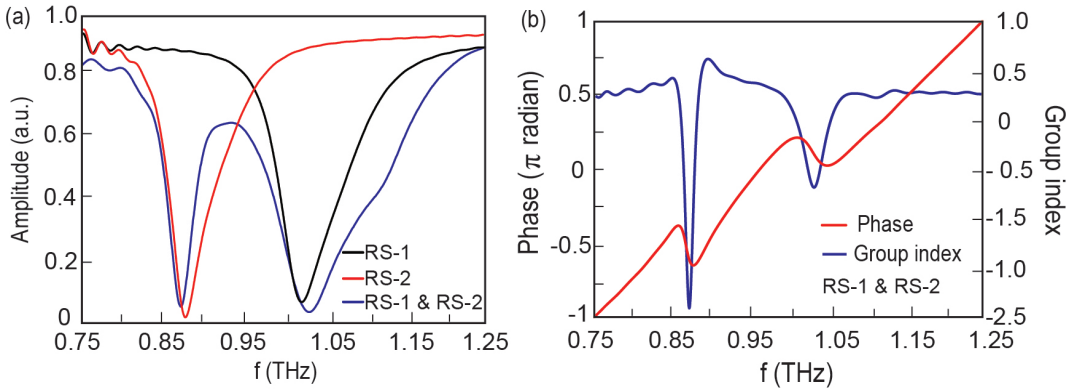

Figure 4.2: (a)Numerically calculated transmission amplitudes of proposed terahertz waveguide. (b) Depicts the phase and group index values of the transmitted terahertz versus frequency in the proposed waveguide geometry with dielectric material of n = 1.2 filled in RS-2.

responds to transmission amplitude of terahertz waveguide consisting of one metallic slab, which is comprised of RS-1, which indicate air medium of refractive index 'n' = 1. The transmission amplitude gives resonant mode at ω_1 = 1.02 THz, supported by

the waveguide for 'n' = 1, whereas, red trace corresponds to transmission properties of another waveguide configuration consisting of metallic slab comprising RS-2 for refractive index 'n' = 1.2. This gives another resonant or bright mode at ω_2 = 0.88 THz. One may notice that the bright mode gets red shifted while increasing the refractive index value of the dielectric material. Hence, we found two bright modes supported by terahertz waveguides at two distinct frequencies (ω_1 and ω_2) close to each other. In the next step, the two terahertz waveguides consisting of two metallic slabs comprising both RS-1 and RS-2 are placed parallel to each other maintaining a gap 'g' = 100 μm. The incident terahertz beam propagates through the gap and resulting resonances from the two slots are allowed to interfere. As a consequence, we observe an PIT-window at 0.93 THz, due to the destructive interference of the two bright modes. The corresponding transmission amplitude is indicated through blue trace in Fig. 4.2(a). After that, we examine the change of phase value of the transmitted terahertz signal. The numerically calculated phase value versus frequency is shown in Fig. 4.2(b) in red color trace. A dramatic change in the phase value further elucidate the PIT effect. Further, we have calculated group index value corresponding to the phase plot in the same figure which can be noticed in the blue color trace. The group index (n_g) is an important feature of the PIT effect and is associated with the phase by the following relation [138],

$$n_g = -\frac{c}{d}\frac{d\phi}{d\omega}$$

where, c is the velocity of light in free space, d is the total length of waveguide and ϕ is the phase of the transmitted terahertz. A sharp change in the group index signifies a highly dispersive character of the PIT effect which is important to several applications including slow light systems.

4.4 Electric field profiles

Next, we examine the electrical field profiles supported by the proposed parallel slabs terahertz waveguide in z-x plane at three distinct frequencies, 1.02 THz, 0.88 THz,

and 0.93 THz to check the PIT effect. The first two resonance frequencies i.e. 1.02 THz and 0.88 THz are supported by the two bright modes of RS-1 and RS-2, respectively. The PIT – window is observed at frequency 0.93 THz. These three frequencies can be

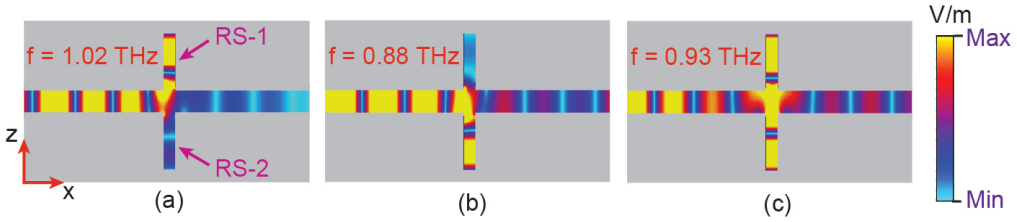

Figure 4.3: (a) – (c) represent electric field profiles in z-x plane supported by RS-1 and RS-2, individually and both RS-1 & RS-2 together at different frequencies i.e. 1.02 THz, 0.88 THz, and 0.93 THz, respectively. The different parameters of the proposed terahertz waveguide are kept fixed 'l' = 50 μm, 'w' = 600 μm, 'h' = 200 μm, 'g' = 100 μm.

verified from Fig. 4.2(a). The results of electric field profiles are shown in Fig. 4.3(a) – (c). From the figures, it can be observed that the rectangular slots without and with dielectric material are excited at their corresponding resonance frequencies 1.02 THz and 0.88 THz, respectively. At 0.93 THz, both the rectangular slots (RS-1 & RS-2) are excited since this frequency corresponds to the PIT window.

4.5 Theory

After that, we employed theoretical modelling based on coupled harmonic oscillators to validate our numerically obtained transmission results of the proposed terahertz waveguide configuration [139–141]. The transparency window can be theoretically analyzed by introducing a two-particle model -a particle (designated as particle m_1) represents the bright mode RS-1, and a particle (designated as particle m_2) represents another bright mode RS-2, both are driven by the incident electric field. The particles RS-1 and RS-2 both are supposed to have the same resonant frequency. Assuming that the coupling strength between the two particles is Ω, and the loss factors (γ_1 & γ_2) of the two particles is much less than the resonant frequency, then the displacements (x_1 & x_2) of the resonators RS-1 and RS-2 with respect to their respective equilibrium positions satisfy the these coupled differential equations. One can write

equations of motion for the coupled system where both the resonators are driven by the external force as

$$\begin{aligned} \ddot{x}_1(t) + \gamma_1 \dot{x}_1(t) + \omega_1^2 x_1(t) - \Omega^2 x_2(t) &= (F/m_1)\exp^{(-i\omega t)} \\ \ddot{x}_2(t) + \gamma_2 \dot{x}_2(t) + \omega_2^2 x_2(t) - \Omega^2 x_1(t) &= (F/m_2)\exp^{(-i\omega t)} \end{aligned} \tag{4.1}$$

where (m_1, m_2), (γ_1, γ_2), and (ω_1, ω_2) are the masses, damping factors and resonance frequencies of the two coupled resonators, Ω represents the coupling coefficient between the two resonators, and ω is the frequency of the incident terahertz wave. Here

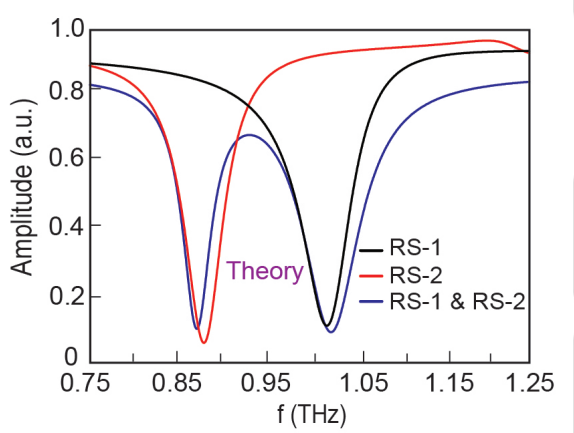

Figure 4.4: THz transmission spectra of proposed terahertz waveguide from theoretical modelling based on coupled harmonic oscillator. Black, red, and blue traces correspond to RS-1, RS-2 and the combined structure, RS-1 & RS-2, respectively.

incident terahertz wave acts as the driving forces for both the resonators and ω is the coupling coefficients between the resonators. Assuming the solution of equation (4.1) as $x_i = N_i \exp^{(-i\omega t)}$, where N_i being constants, we can obtain the following solutions of the x_i as

$$\begin{aligned} x_1 &= \frac{\frac{F}{m_1}D_2 + \frac{F}{m_2}\Omega^2}{D_1 D_2 - \Omega^4}\exp^{(-i\omega t)} \\ x_2 &= \frac{\frac{F}{m_2}D_1 + \frac{F}{m_1}\Omega^2}{D_1 D_2 - \Omega^4}\exp^{(-i\omega t)} \end{aligned} \tag{4.2}$$

where $D_1 = \omega_1^2 - \omega^2 - i\omega\gamma_1$ and $D_2 = \omega_2^2 - \omega^2 - i\omega\gamma_2$. The energy dissipated by RS-1 and RS-2 can be calculated as

$$\begin{aligned} P_1(\omega) &= \frac{\frac{D_2}{m_1} + \frac{\Omega^2}{m_2}}{D_1 D_2 - \Omega^4} \\ P_2(\omega) &= \frac{\frac{D_1}{m_2} + \frac{\Omega^2}{m_1}}{D_1 D_2 - \Omega^4} \end{aligned} \tag{4.3}$$

and the total energy dissipated by the proposed terahertz waveguide structure exhibiting PIT effect

$$P = P_1 + P_2 \tag{4.4}$$

The transmission amplitude for the system can be expressed as,

$$t(\omega) = 1 - ImP(\omega) \tag{4.5}$$

One can use Equations (4.3) and (4.5) to theoretical fit the numerically obtained transmission response of Fig. 4.2(a). In Fig. 4.4, theoretically fitted transmission spectra are depicted which indicates reasonably good agreement with the numerical simulations. The black and red traces illustrate individual transmission spectrum for RS-1 and RS-2 (having refractive index 'n' = 1.2), respectively. The blue traces represent the transmission spectrum of proposed waveguide comprising both RS-1 and RS-2. The spectrum exhibits PIT effect for the specific values of the different parameters, given in Table 4.1.

Type of RS	ω_1 (THz)	ω_2 (THz)	γ_1 (THz)	γ_2 (THz)	Ω (THz)
RS-1	1.03	1.023	0.22	0.12	0.006
RS-2	0.88	0.87	0.11	0.15	0.005
RS-1 & RS-2	1.03	0.873	0.054	0.078	0.18

Table 4.1: Parameters for the theoretical modelling for different types of RS.

From Table 4.1, one may notice that the damping factor values, γ_1 and γ_1 of the two oscillators in double slot waveguide configuration are lower as compared to the values of single slot waveguides. This signifies to the low absorption loss in double slot configuration due to the enhanced waveguide transmission of the terahertz in the cou-

pled system. On the other end, the value of coupling coefficient, Ω is negligibly small in case of the single slot waveguides owing to the uncoupled structures, however it is significantly higher i.e. 0.18 in double slot configuration because of strongly coupled resonators i.e. RS-1 and RS-2. The resonance frequencies corresponding to RS-1 and RS-2 have been obtained by fitting the parameters given in table to the numerically simulated results. For the given set of parameters, it is apparent that the theoretical predictions match well with the simulation results.

4.6 Tunable control of PIT window

Further, we investigate the tuning of the PIT-window by varying the refractive index (n) value of dielectric material of RS-2. The numerically obtained results of transmission spectra of the proposed terahertz waveguide is depicted in Fig. 4.5(a). Different color traces correspond to different 'n' value of the dielectric material. While examining the tuning of PIT – window, the following parameters are kept fixed, 'l' = 50 μm, 'w' = 600 μm, 'h' = 200 μm, 'g' = 100 μm. From the figure, it is evident that the PIT–window gets broadened while increasing the value of refractive index of the dielectric material. This is observed due to the red shifting of the resonant mode supported by RS-2. It is quite obvious that resonant mode gets shifted to lower frequency side while increasing the 'n' value of dielectric material. It can be noted that there is a minimal change in frequency of the resonant mode supported by RS-1, compared to the resonant mode supported by RS-2 with the increase of refractive index of dielectric, which clearly indicates the role of dielectric material to modulate the PIT–window.

In order to verify the numerical findings and understand the physics behind the tuning of the PIT–window based on refractive index of the dielectric material, we again employed theoretical modelling based on coupled harmonic oscillators as discussed in above section to calculate the transmission spectra for different 'n' value. The results are shown in Fig. 4.5(b). Different color traces correspond to different 'n' value of dielectric in RS-2. From the figure, it can be noticed that the transmission spectra from

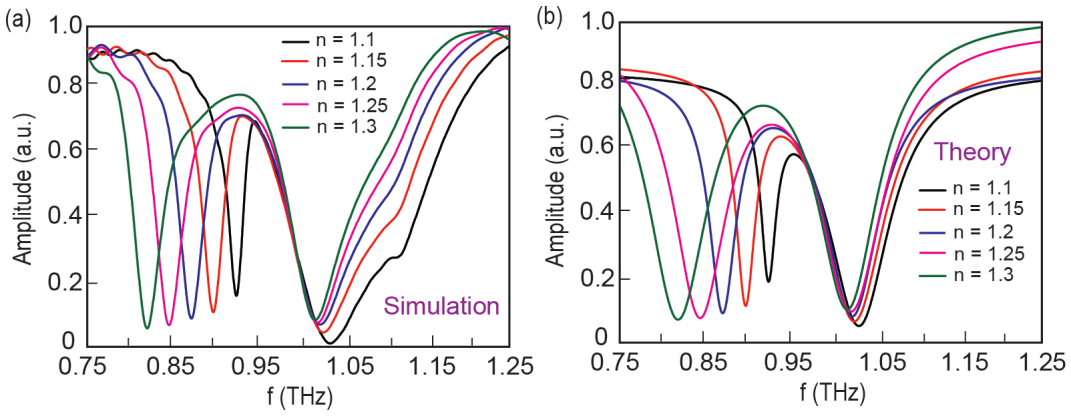

Figure 4.5: THz transmission spectra of the proposed terahertz waveguide for different refractive index (n) value of dielectric material in RS-2. Different color traces indicate different 'n' value of dielectric. The other parameters are: 'l' = 50 μm, 'w' = 600 μm, 'h' = 200 μm, 'g' = 100 μm. (a) represents numerical simulated results while (b) corresponds to theoretical modeling.

theoretical modelling for different 'n' value resemble quite well with the corresponding numerically obtained results as shown in Fig. 4.5(a).

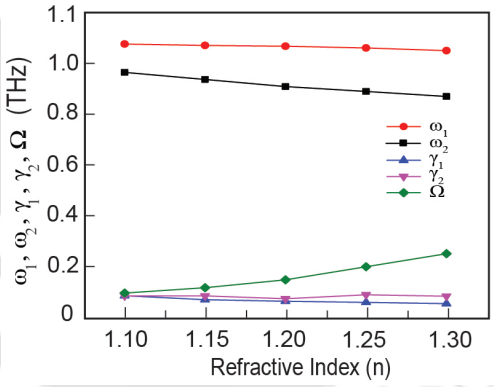

Figure 4.6: The variations of the fitting parameters with respect to the refractive index of dielectric in RS-2.

The modulation of PIT-window is associated with different values of specific parameters. To explain the shift of the dips of the resonant modes with the change of refractive index of dielectric, we have shown the variation of the fitting parameters ω_1, ω_2, γ_1, γ_2 and Ω versus refractive index (n) of dielectric. The results are shown in Fig. 4.6. It may be noted from the figure that the damping factor γ_1 decreases slightly which causes an increase in the amplitude of the resonant mode on lower frequency side and γ_2 remains almost constant. The resonance frequency ω_2 of RS-2 resonator changes

from 0.927 THz to 0.835 THz which causes blue shift of of the resonant mode on lower frequency side. Also, the coupling coefficient Ω increases with the change of refractive index, which increase the broadness of the transparency window. On the other hand, one can notice negligible change in the resonance frequency ω_1 on higher frequency side with the refractive index. This is because there is no dielectric in RS-1. Therefore, the blue shift of the resonant mode on lower frequency side occurs due to the change of resonance frequency ω_2. This study could have potential in refractive index-based sensing application at terahertz frequencies. Further, we calculate group index value

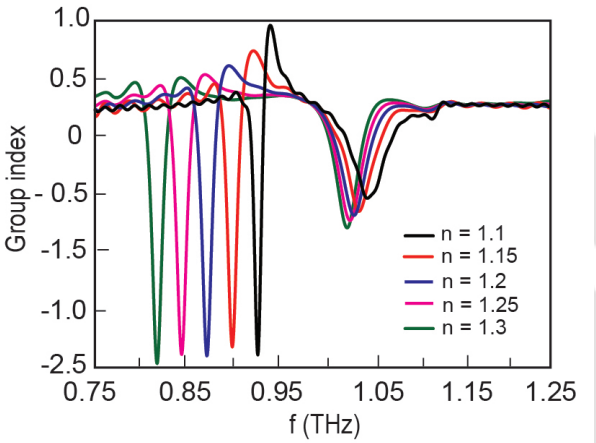

Figure 4.7: Numerically calculated group index as a function of frequency for different refractive index values of the material filled in RS-2.

from the transmitted phase information using the following formula [138],

$$n_g = -\frac{c}{d}\frac{d\phi}{d\omega}$$

where, c is the velocity of light in free space, d is the total length of waveguide and ϕ is the phase of the transmitted terahertz. We have plotted group index value versus frequency for the different values of refractive index of the dielectric material filled in RS-2 (Fig. 4.7). In all the traces, strong dispersion in the PIT window is evident. Also, we observed that the PIT-window can be tuned by varying the refractive index of the dielectric material.

Next, we present a contour plot of numerically obtained transmission results of the

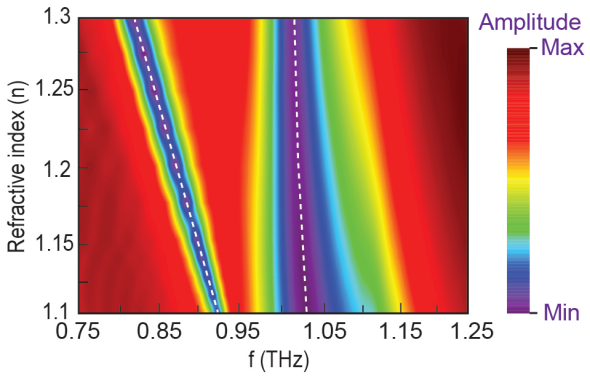

Figure 4.8: Modulation of PIT- window for fixed parameters of double parallel slot terahertz waveguide: 'l' = 50 μm, 'w' = 600 μm, 'h' = 200 μm, 'g' = 100 μm. Contour plot of numerically obtained transmission spectra of proposed terahertz waveguide for different refractive index (n) value of dielectric material of RS-2. Color bar shows the amplitude of transmission signal.

proposed terahertz parallel slots waveguide for the varying refractive index (n) of the dielectric material filled in one of the two rectangular slots. We have investigated the transmission output for eleven different 'n' values from 'n' = 1.1 to 'n' =1.3. The contour plot gives a comprehensive analysis of tuning of PIT – window depending upon the 'n' value of the dielectric. The plot is shown in Fig. 4.8. In the figure, the frequency and refractive index (n) of dielectric are shown along the x and y-axis, respectively while the color bar indicates the amplitudes of the transmission signals. The white color dashed lines indicate the position of resonant modes supported by RS-1 and RS-2 on higher and lower frequency sides, respectively. This resonant mode on lower frequency side gets red shifted while increasing the 'n' value of the dielectric and the PIT–window gets broadened, which can be observed from the contour plot. One may notice that there is substantial change in frequency of resonant mode supported by RS-2 due to the varying 'n' value of the filled dielectric material, whereas there is a negligible change in the frequency of resonant mode supported by RS-1.

4.7 Discussions

In summary, we proposed a double slot terahertz waveguide capable of exhibiting an PIT effect when one of the slot is filled with a dielectric material. We observed that the resonating slots acts as the two bright modes at two distinct frequencies ω_1

and ω_2 close to each other. The coupling of these two bright modes causes an PIT-window through a destructive interference. The electric field profiles are examined which further ensure the PIT effect. Additionally, a theoretical model based on coupled harmonic oscillator is employed to elucidate the numerically obtained results. The findings from the theory are found to be in good agreement with the simulation for the specific set of parameters. We further notice that the PIT-window can be broadened when dielectric material of higher refractive index value is filled in one of the resonating slots. Our study suggest that an PIT window can be realized and controlled using an appropriate dielectric material in the resonating slot, and provide an alternative where a change in physical dimensions is cumbersome talk. The study could be very significant where an active and tunable control of PIT effect is needed viz. ultra-slow light systems, terahertz buffers, refractive index sensors etc. The proposed concept of PIT effect can also be pursued in other regions of electromagnetic spectrum as well.

5

Tunable control of Plasmon Induced Transparency

Contents

In continuation to the previous work, this chapter describes the control of PIT effect in a metal-air-metal waveguide consisting of two pyramidal corrugations. We discuss how one can achieve PIT effect by filling one of the grooves with a dielectric material and then tune the transparency window by changing conducting of silicon film placed between two grooves.

5.1 Introduction

PIT, an analog of EIT, has drawn more attention due to its promising on-chip applications as discussed in the last chapter. In this context, Xu et al. have experimentally observed a Si micro-ring resonator coupled to a parallel waveguide to realize a transparency window by constructive interference [142]. Zhao et al. have demonstrated the PIT effect in a subwavelength metal structure waveguide consisting of metallic cut wires and double-gap split-ring resonators [143]. The waveguides with externally controllable PIT effect can be significant in building devices and components at the THz frequencies. Semiconductors are a good candidate in this regard, as their conductivity can be modified when external stimuli such as temperature, voltage bias, and photo-excitation are applied. Recently, silicon (Si) has been investigated by the scientific community for its ability to enable adjustable, flexible and practical devices. Silicon is a semiconductor material, having excellent physical and optical properties where the conductivity can be modulated by controlling the dopant concentration. This can be significant in modulating the absorption at terahertz frequencies. We investigate the modulation of PIT window by combining silicon this film with our geometry resulting in PIT effect. Modulation of the PIT effect, despite being significant, has not been examined much. Therefore for technological breakthrough and developments, there is a strong need to pursue research in this direction.

We propose a metal-air-metal waveguide comprising double pyramidal groove structures, which exhibits the plasmon induced transparency (PIT) effect through destructive interference of two bright resonators. To study the active modulation of plas-

mon induced transparency window, we varied refractive index of the dielectric in one of the pyramidal grooves. The chapter is organized as follows: first, we discuss the proposed waveguide geometry comprising two pyramidal grooves filled with air and dielectric. After that, we numerically examine the transmission spectra of the proposed waveguide for different cases viz. air and dielectric filled grooves only and both the grooves in parallel configuration. Next, we employ a theoretical model based on the three-level plasmonic model to understand and validate our numerically obtained transmission properties. After that, we examine electric field profiles to ensure PIT-effect is supported by the proposed waveguide. Further, we vary refractive index of the dielectric material to actively modulate the PIT window. Next, active modulation and switching of PIT effect are examined by placing a silicon sheet on the top of a groove and varying its conductivity. A comprehensive picture of active modulation of the PIT window with conductivity is presented through a contour plot. Finally, we summarize the results in the discussion section.

5.2 Schematic of THz waveguide

The schematic illustration of the proposed metal-air-metal waveguide is shown in Fig.5.1. The metal-air-metal structure consists of an air medium sandwiched between the two parallel metallic blocks. Two pyramidal groove structures are designed in the blocks along transverse direction. A gap of 100 um is maintained between the two blocks. One of the two pyramidal grooves is filled with a dielectric material of varying refractive index to study the active modulation of PIT window and the other one remains empty. We have used the terms PG-1 and PG-2 for pyramidal resonating grooves without and with dielectric, respectively, throughout the study. In the schematic, the different structure parameters of PG are denoted as: width (w), length (l_1 and l_2), depth (h), and gap between the two grooves (g). The following values of different parameters remain fixed throughout the study: w = 800 μm, l_1 = 50 μm, l_2 = 120 μm, h = 200 μm, g = 100 μm.

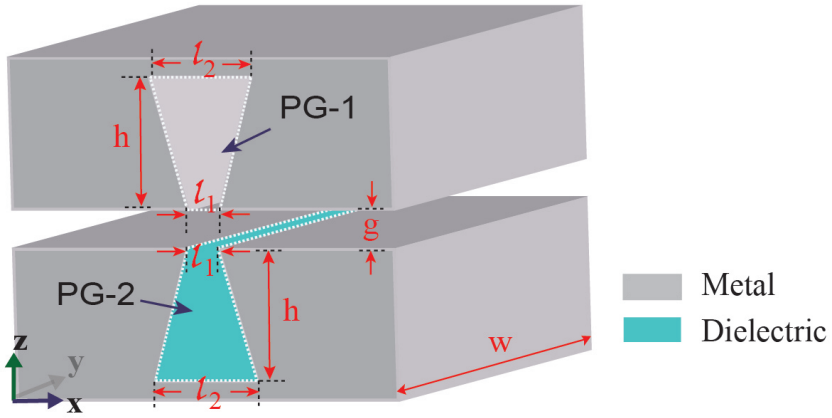

Figure 5.1: Schematic of proposed metal-air-metal waveguide geometry: 3-D view of proposed waveguide design consisting of two parallel metallic blocks. Two pyramidal groove structures are designed in the two metallic blocks i.e. PG-1 and PG-2. The gap (g) between two blocks is fixed at $g = 100$ µm. The lower groove (PG-2) is filled with dielectric. The geometrical parameters of the grooves are as follows: $l_1 = 50$ µm, $l_2 = 120$ µm, $w = 800$ µm, $h = 200$ µm.

In our designed metal-air-metal waveguide comprising pyramidal grooves, a terahertz broadband signal is coupled to the one end of the waveguide. While propagating along x-axis in the air medium between the two parallel metallic slabs, it further couples to the pyramidal groove structures. Finally, it is detected at the other end of the waveguide. It is important to highlight that the proposed waveguide can be fabricated via conventional photolithography technique by using a highly doped silicon substrate while taking advantage of its crystalline structure. It is important to highlight that the proposed waveguide can be fabricated via conventional photolithography technique by using a highly doped silicon substrate while taking advantage of its crystalline structure. The corrugations of the waveguide depend on the crystal orientation of the silicon substrate. To make pyramidal grooves, one can use a crystalline silicon wafer of (100) orientation with dopant concentration, $n \geq 10^{19} cm^{-3}$ which behaves like a perfect conductor at terahertz frequencies. Using low-pressure chemical vapor deposition (LPCVD) technique, the silicon dioxide layer can be grown on the silicon surface and further, patterns can be made via photolithography technique [118,119]. In the next step, appropriately patterned silicon can be etched in a mixture of potassium hydroxide, water, and isopropanol in the ratio of 60:30:10 to make inverted pyramidal

apertures [144]. For the fabrication of groove, a silicon wafer can be glued on the back of the pyramidal apertures using a conducting epoxy. For characterization, one can use the technique of terahertz time-domain spectroscopy (THz-TDS) [145].

5.3 Waveguide transmission and PIT effect: Simulation and Theory

We have performed the simulations with the help of finite element time domain solver in a commercially available Computer Simulation Technology (CST) microwave studio software to obtain the transmission properties. In simulations, open boundary conditions are assumed in all directions and metal is considered as a perfect electrical conductor (PEC) due to its high conductivity at terahertz frequencies. Single cycle z-polarized terahertz beam is incident at one end of the waveguide and allowed to propagate along the gap between two parallel metallic blocks. While propagating through the gap it couples to PG-1 & PG-2 and finally, it is probed at the receiver end of the waveguide in the form of time domain signal, which is converted into frequency domain using Fast Fourier Transform (FFT). First, we examine a waveguide design comprising PG-1 and PG-2 individually, which correspond to empty (air) and filled pyramidal groove of refractive index 'n' = 1 and 1.2, respectively. Next, we investigate the waveguide comprising both PG-1 and PG-2. Fig.5.2(a) depicts the results of numerically calculated transmission properties of the proposed terahertz waveguide for PG-1, PG-2 individually and for both PG-1 and PG-2. In the figure, black, green and red traces correspond to numerically obtained transmission amplitude of the terahertz waveguide for PG-1, PG-2 and both PG-1 and PG-2, respectively. It can be noticed from the figure that PG-1 supports bright mode with resonance frequency ω_1 = 1.04 THz, whereas PG-2 exhibits bright mode at ω_2 = 0.87 THz. Hence, the waveguide supports two terahertz bright modes from the resonators of the waveguide at two distinct frequencies (ω_1 and ω_2) close to each other. These two bright modes experience destructive interference while propagating through the gap between the two parallel blocks of waveguide comprising both PG-1 and PG-2 and thereby exhibit plasmon induced

transparency window at 0.92 THz.

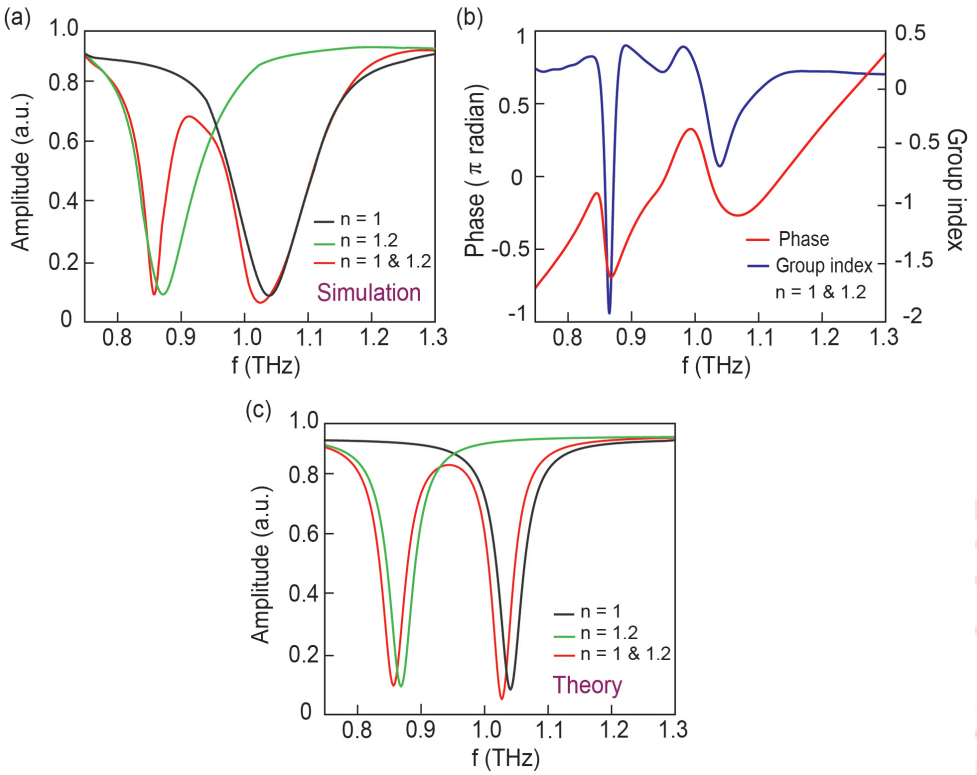

Figure 5.2: (a) THz transmission spectra of proposed terahertz waveguide from simulation. Black, red, and blue traces correspond to PG-1, PG-2 and the combined structure, PG-1 & PG-2, respectively. (b) Transmission characteristics from theoretical modelling based on three level plasmonic system. The different parameters of the proposed terahertz waveguide are kept fixed: $l_1 = 50$ µm, $l_2 = 120$ µm, $w = 800$ µm, $h = 200$ µm.

In order to validate our numerically obtained transmission properties and get a physical insight into the coupling mechanism of two bright modes involved in the plasmon-induced transparency, we employ a three-level plasmonic model [126], which already has been discussed in chapter 3. In our case, waveguide supports two modes from the resonators of the waveguide at two different nearby frequencies. These modes are coupled via a strong electric field in near field configuration. The two resonant modes are termed as bright modes due to simultaneous excitation under the effect of incident terahertz beam. The amplitudes of these two radiative resonant modes can be

expressed in terms of coupled Lorentz oscillators as

$$\begin{pmatrix} \tilde{a} \\ \tilde{b} \end{pmatrix} = \frac{1}{(\delta + i\gamma_a)(\delta + i\gamma_b) - \kappa^2} \begin{pmatrix} (\delta + i\gamma_b) & -\kappa \\ -\kappa & (\delta + i\gamma_a) \end{pmatrix} \begin{pmatrix} -GE_0 \\ -GE_0 \end{pmatrix} \tag{5.1}$$

where $\tilde{a}$ and $\tilde{b}$ are induced THz field amplitude corresponding to the two resonators i.e. PG-1 and PG-2 respectively. The two modes have adjacent resonance frequencies ω_1 and ω_2, such that $\delta = \omega - \omega_1 = \omega - \omega_2$ is very small in Eq.(5.1). γ_a and γ_b are the damping factor of the resonant modes, which are much smaller than the resonance frequencies. E_0 is the amplitude of the incident THz electric field whereas is the corresponding frequency of the incident THz signal; κ is the coupling coefficient between the two bright modes; G is a geometric parameter which represents the coupling between the resonators and the incident THz electric field.

From Eq.(5.1), the field amplitude of the 1^{st} mode can be expressed as,

$$\tilde{a} = \frac{-GE_0(\delta + i\gamma_b) + \kappa GE_0}{(\delta + i\gamma_a)(\delta + i\gamma_b) - \kappa^2} = \frac{GE_0[\kappa - (\omega - \omega_2 + i\gamma_b)]}{(\omega - \omega_1 + i\gamma_a)(\omega - \omega_2 + i\gamma_b) - \kappa^2} \tag{5.2}$$

Similarly, for the 2^{nd} mode, it is given by,

$$\tilde{b} = \frac{GE_0[\kappa - (\omega - \omega_1 + i\gamma_a)]}{(\omega - \omega_1 + i\gamma_a)(\omega - \omega_2 + i\gamma_b) - \kappa^2} \tag{5.3}$$

The transmission coefficient of the plasmonic waveguide can be written as:

$$T = \left|\frac{\tilde{a}}{E_0}\right|^2 + \left|\frac{\tilde{b}}{E_0}\right|^2$$

$$T = |a|^2 + |b|^2 \tag{5.4}$$

We use Eq.(5.4) to calculate the terahertz transmission coefficients separately for three different waveguide configurations comprising PG-1 only, PG-2 only and the combined structure of PG-1 & PG-2. The results of corresponding transmission spectra are shown in Fig.5.2(b). Different color traces indicate transmission for the corresponding refractive index 'n' value of different waveguide configurations. Theoretical modeling gives rise to synonymous transmission spectrum as obtained through numerical

simulations for a specific set of values of the modeling parameters given in Table-5.1. From the figures, it can be noticed that theoretically obtained dip frequencies of two resonant modes along with the plasmon induced window match with the numerically obtained results. From Table-5.1, one can observe that the value of the coupling coeffi-

Resonator type	G (THz)	κ (THz)	γ_a (THz)	γ_b (THz)
PG-1	0.23	0	0.127	0.127
PG-2	0.23	0	0.131	0.131
PG-1 & PG-2	0.3	0.04	0.112	0.125

Table 5.1: Specific values of parameters for the theoretical modeling of PIT effect

cient parameter is zero for PG-1 and PG-2 individually, since the resonators are excited separately i.e. in the absence of any other aperture resonator. Furthermore, it can be observed that the value of the geometric parameter increases when waveguide configuration is comprised of both the resonators PG-1 and PG-2 rather than a waveguide comprising of either of two resonators. This is due to the strong coupling of the two resonant modes supported by the combined structure of both PG-1 and PG-2 with the incident terahertz beam rather than the coupling of either of two resonant modes supported by either PG-1 or PG-2 in the proposed waveguide configurations.

5.4 Electric field profiles

To get more insight into the PIT-effect through coupling between the two radiative modes supported by PG-1 and PG-2, we examined electric field profiles supported by the waveguide at three different frequencies 1.04 THz, 0.87 THz, and 0.92 THz. From Fig.5.2(a) we have confirmed that PG-1 and PG-2 exhibit resonant modes with resonance frequencies 1.04 THz and 0.87 THz, respectively, whereas combined structure of PG-1 and PG-2 exhibit PIT-effect at 0.92 THz. The results of electric field profiles supported by the waveguide configuration in z-x plane are depicted in Fig.5.3(a) – (c). From the figures Fig.5.3(a) and (b), it can be observed that PG-1 and PG-2 are excited at their corresponding resonant frequencies. In Fig.5.3(c), it can be noticed that both

pyramidal grooves PG-1 and PG-2 are excited at 0.92 THz, which corresponds to the frequency of PIT-effect.

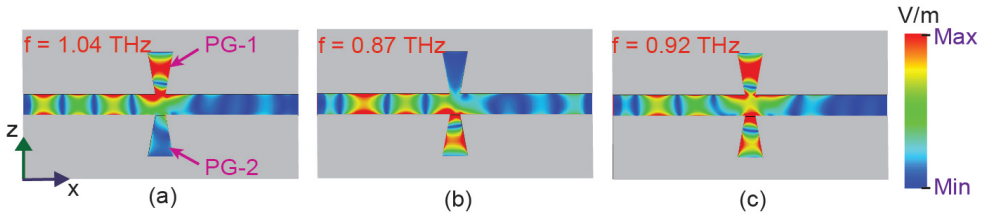

Figure 5.3: (a) – (c) represent electric field profiles in z-x plane supported by PG-1 and PG-2, individually and both PG-1 & PG-2 together at different frequencies i.e. 1.04 THz, 0.87 THz, and 0.92 THz, respectively. The different parameters of the proposed terahertz waveguide are kept fixed: $l_1 = 50$ µm, $l_2 = 120$ µm, $w = 800$ µm, $h = 200$ µm.

5.5 Active modulation of PIT window

Next, we investigate the active modulation of the PIT-effect. In order to do so, we varied the refractive index value of the dielectric material in PG-2 from n = 1.1 to 1.3, whereas PG-1 remains empty. The other physical parameters of the waveguide remain fixed: l_1 = 50 µm, l_2 = 120 µm, w = 800 µm, h = 200 µm. The corresponding numerically obtained transmission spectra for varying $'n'$ values are shown in Fig.5.4(a). It can be observed from the figure that there is a minimal change in the frequency of the resonant mode supported by PG-1, but we observe substantial red shifting in resonance frequency of the mode supported by PG-2. The change in refractive index value causes a red shift along with the broadening of the PIT-window. Hence, we found that the active modulation of PIT-effect can be accomplished with the varying the refractive index of the dielectric material, without causing a change in the physical dimensions of the structures.

Next, we again employ the three level plasmonic model to validate numerical findings and understand the coupling mechanism between the two radiative resonant modes supported by PG-1 & PG-2. The transmission coefficients obtained using theoretical modeling are plotted in Fig.5.4(b) for different refractive index values (n) of the dielectric material in PG-2. Different color traces correspond to different values of refrac-

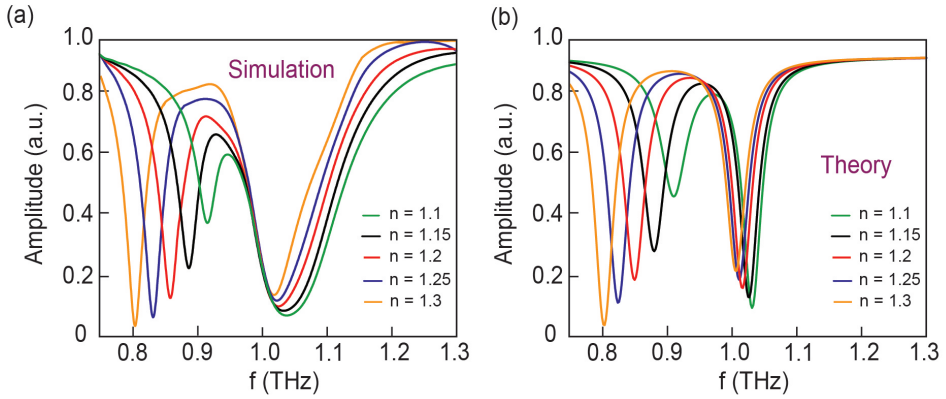

Figure 5.4: Modulation of the PIT window of the proposed terahertz waveguide for different refractive index (n) value of dielectric material in PG-2. Different color traces indicate different 'n' values of dielectric. The other parameters are: l_1 = 50 µm, l_2 = 120 µm, w = 800 µm, h = 200 µm. (a) Represents numerically simulated results while (b) corresponds to theoretical modeling.

tive index (n). Theoretical modeling gives rise to synonymous transmission spectrum as obtained through numerical simulations. The modeling results in same resonance frequencies of the resonant modes along with the PIT-window for varying refractive indices for specific set of fitting parameters given in Table-5.2. From the table, one can notice that as we increase the refractive index value of dielectric material in PG-2, the coupling coefficient value increases. It is due to the fact that the propagating terahertz surface waves along the gap undergo more interaction as we increase the refractive index value of dielectric material.

R.I. (n) of dielectric material of PG-2	G (THz)	κ (THz)	γ_a (THz)	γ_b (THz)
1.1	0.3	0.03	0.108	0.155
1.15	0.3	0.035	0.11	0.13
1.2	0.3	0.04	0.0112	0.125
1.25	0.3	0.045	0.114	0.12
1.3	0.3	0.05	0.116	0.115

Table 5.2: Parameters for the theoretical fit for various refractive index (n).

5.6 Tunability of transparency window using silicon sheet

In order to get a better understanding of switching and tunability of the plasmon induced transparency window, we have placed a sheet of semiconducting material like silicon (Si) just above the PG-2 in the gap of the waveguide configuration as shown in the inset of Fig.5.5(a). The silicon material properties are chosen from the experimental data [121]. In the terahertz region, the frequency dependent complex dielectric constant of silicon can be given by the simple Drude model approximation,

$$\varepsilon = \varepsilon_\infty + \frac{i\sigma}{\omega_0 \varepsilon_0} = \varepsilon_\infty - \frac{\omega_p^2}{\omega(\omega + i\Gamma)} \tag{5.5}$$

where, ε_∞ is the contribution of the bound electrons, $\Gamma = \frac{1}{\tau}$ is the damping rate, and τ is the average collision time. ω_p plasma angular frequency which is dependent on the number density of carriers in silicon material.

We have varied the electrical conductivity of the silicon (Si) sheet from 0 S/m to 5000 S/m. The corresponding transmission spectra are plotted in Fig.5.5(a) for different values of conductivity. Different color traces indicate transmission spectra corresponding to different values of electrical conductivity of silicon sheet. From the plot, it is evident that there is a substantial decrease in the amplitude of the resonant mode supported by PG-2 when conductivity value of silicon sheet is increased. On the other hand, the amplitude of the resonance mode supported by PG-1 remains almost unchanged. It is found that the resonant mode supported by PG-2 completely vanishes at a conductivity value of 5000 S/m. This is owing to the fact that the silicon sheet over PG-2 becomes highly conducting in nature which forbids the propagating terahertz wave to interact with the pyramidal groove, PG-2. Hence, the resonant mode supported by PG-2 is not observed at high conductivity value.

Next, we present a comprehensive analysis of switching and tunability of PIT–window through a contour plot of the numerically obtained transmission results for the varying conductivity value of silicon. We have investigated the transmission spectra for forty

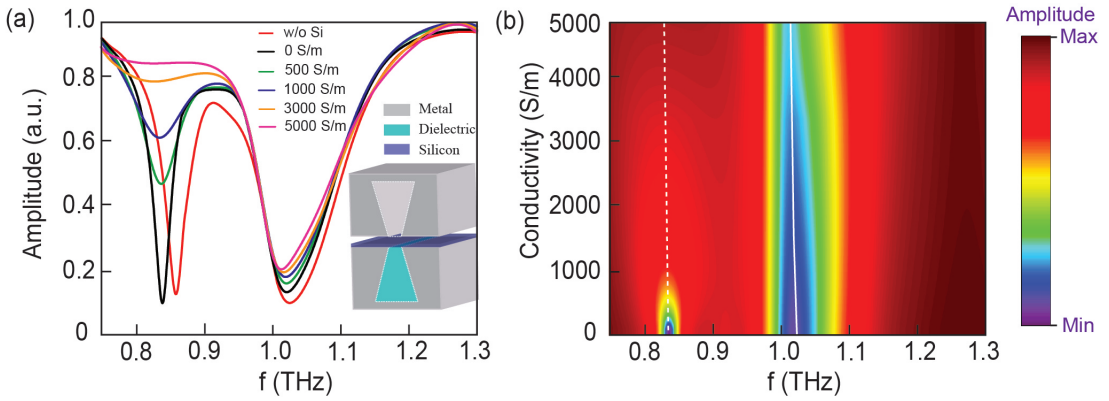

Figure 5.5: (a) Switching and tunability of transparency window for fixed parameters of double parallel groove terahertz waveguide: $l_1 = 50$ µm, $l_2 = 120$ µm, $w = 800$ µm, $h = 200$ µm. Numerically obtained transmission spectra of proposed terahertz waveguide for different conductivity of silicon layer placed on the top of PG-2. (b) Contour plot for different conductivity of the silicon layer. Color bar shows the amplitude of transmission signal.

different electrical conductivity values from 0 S/m to 5000 S/m. The contour plot is depicted in Fig.5.5(b). In the figure, the frequency and electrical conductivity values of silicon are shown along the x and y-axis, respectively while the color bar indicates the amplitudes of the transmission spectrum. The solid and dotted white lines the positions of resonant modes supported by PG-1 and PG-2, respectively. The resonant mode supported by PG-2 vanishes as electrical conductivity value of silicon increases, which can be observed from the contour plot.

5.7 Discussions

In summary, we demonstrate actively tunable and switchable plasmon induced transparency effect in a parallel plate terahertz waveguide configuration comprising of air-dielectric grooves. The two pyramidal grooves support resonant modes at two different frequencies adjacent to each other. The strong coupling between modes causes the plasmon induced transparency (PIT) effect in the proposed configuration. A three level plasmonic theoretical model is employed to confirm the PIT-effect. The electric field profiles examined at different frequencies in the PIT window clearly depict the PIT-effect. In order to achieve active modulation of the PIT-effect, the refractive index of dielectric material filled in one of the grooves is varied. We observe that the PIT-

window gets broadened when the refractive index increases. We have further demonstrated that the PIT effect can be tuned and resonance can be turned ON and OFF by varying the conductivity of silicon sheet placed between the grooves. The proposed study is highly significant wherever an active modulation of PIT effect and resonance switching is required. The information can ultimately be helpful in the construction of active components operating at terahertz frequencies. The proposed concept of active modulation of PIT effect in the terahertz regime can also be pursued in other regions of the electromagnetic spectrum.

6

Modulation in Graphene Nanoribbons assisted Dielectric Metamaterial

Contents

This chapter examines the broadband terahertz modulation in a dielectric metamaterial combined with graphene nanoribbons. Our design is tunable and polarization-sensitive an hence useful for the development of polarization optics at terahertz frequencies. The broadband response further makes it attractive for hight speed and broadband communication applications.

6.1 Introduction

Several applications in terahertz photonics require the development of devices sensitive to a particular polarization. The graphene ribbon structures can be important to achieve polarization sensitive absorption properties very limited efforts have been made in this direction. Chen et al. have numerically examined a tunable broadband absorber consisting of multiple layers of graphene ribbons [146]. Their study reveals that the absorption spectrum can be shifted by changing the Fermi energy associated with the graphene ribbons. In addition, researchers have demonstrated designs of metamaterial absorbers with absorption up to 90% by controlling the chemical potential of graphene [5, 146]. The realization of a polarization sensitive nearly-perfect tunable broadband absorption and a deep understanding of the underlying physics are challenging tasks at terahertz frequencies. Some reports have used transmission line theory to design and understand the narrow or broadband THz absorptions [148]. However, fulfilling impedance matching conditions using transmission line method have some constraint. For example, the center frequency cannot be selected randomly in the THz regime [149]. In our study, we have come up with a scheme for polarization-dependent broadband terahertz absorption and modulation and explained the underlying physics by proposing an alternative theoretical and analytical approach.

We propose a metamaterial absorber comprising a stack of frustum-shaped dielectric on the top of a periodic array of graphene nanoribbons (GNRs) deposited over the ultrathin metal-backed dielectric. The structure is polarization sensitive and exhibits broadband absorption response with over 90% absorptivity from 0.6 THz to 1.2 THz

with 72.7% fractional bandwidth. The chapter is organized as follows: first, we describe the proposed geometry and show the absorption and reflection characteristics for transverse magnetic (TM) and transverse electric (TE) modes. Next, we examined the fundamental effect of free-standing graphene nanoribbons to tune the absorption response by varying the Fermi energy. Further, we examined the absorption by incorporating dielectric (SiO_2) spacer and gold metallic ground plane. The addition of a frustum-shaped dielectric geometry on the top of GNRs-SiO_2-Au structure gives a broadband absorption response which has been discussed in the next section. Furthermore, we employed a theoretical model based on effective medium theory (EMT) and transfer matrix method (TMM) to verify our numerically obtained absorption spectrum. In the end, the effect of structural parameters like dielectric thickness and Fermi energy on the absorption spectrum has been investigated. Finally, we summarize the results in the discussion section.

6.2 Schematic of Terahertz Metamaterial Absorber

The 3-D schematic and a unit cell of the proposed graphene based metamaterial absorber are shown in Fig. 6.1. The unit cell of the metamaterial absorber is composed with a stack of four layers. From top to bottom, they are: SiO_2 layer of frustum shaped geometry, a periodic array of graphene nanoribbons, the SiO_2 spacer layer, and a layer of a gold metallic reflector, respectively. All the layers stacked together form a unit cell of the metamaterial absorber. The geometrical parameters of the unit cell are calculated after performing manual optimization through EM simulation. In the schematic, the lower radius (r_1) and upper radius (r_2) of the frustum geometry are 21 μm and 15 μm, respectively. The height (h) of the frustum shaped SiO_2 layer is 60 μm. The width (w_g) and period (Δ) of the periodic array of graphene nanoribbons are 2 μm and 4 μm. The length (l_g) of graphene ribbon is equal to the period (p) of the square unit cell, which is 46 μm. The thicknesses of the SiO_2 spacer layer (t_s) and the ground plane (t_g) are 45 μm and 0.2 μm, respectively. The thickness of the gold layer is chosen to have

thickness greater than the skin depth in the terahertz regime so that the incident wave cannot transmit through this layer. The spacer SiO_2 is chosen as an interlayer dielectric between graphene nanoribbon and ground gold plane. The absorption response can be tuned by adjusting the Fermi energy or electrochemical potential with the help of bias gate voltage.

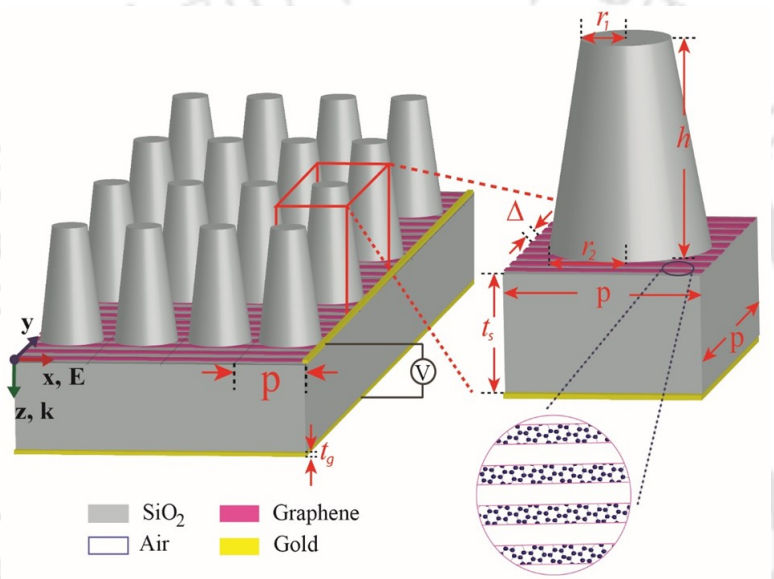

Figure 6.1: Schematic of frustum-shaped graphene-based terahertz absorber geometry: 3-D view of proposed metamaterial absorber design comprising of unit cells. The unit cell of the absorber consists of multiple layer, including dielectric (SiO_2), graphene nano-ribbons (GNRs) and metallic gold plane. The geometrical parameters of unit cell are as follows: r_1= 21 μm, r_2=15 μm, h= 60 μm, t_g= 0.2 μm, t_s= 45 μm, E_F = 1 eV, w_g = 2 μm, Δ = 4 μm and p = 46 μm.

6.3 Numerical Simulations

The absorption characteristics of the proposed structure are investigated using a finite element method based frequency domain solver in a commercially available CST microwave studio suite software. The metamaterial absorber structure is simulated under the unit cell boundary condition in x-y plane. We use adaptive meshing with the maximum mesh element size of the order $\lambda_{max}/10$, where λ_{max} denotes the maximum wavelength of the incident radiation over the considered spectral range. Open boundary conditions are set along the direction of light propagation. It may be noted

that the proposed design can be fabricated in a cleanroom ambiance with an e-beam lithography (EBL)for graphene nanoribbons followed by deep reactive ion etching of SiO_2 to form the frustum shaped dielectric metamaterial. At first, the gold (Au) film is deposited on the top of Si wafer using EBL step [150]. By using chemical vapour deposition (CVD) method, the dielectric SiO_2 spacer layer and graphene monolayer can be deposited. Further, the patterned graphene ribbon can be realized via standard lift-off process [151]. Then, the same dielectric with different thickness is formed on the graphene-dielectric (SiO_2)-Au-Si. Finally, the frustum shaped geometry can be realized by reactive ion etching or lithography method [152]. In this work, the four-layered unit cell is designed in CST by proper assignment of materials using the Drude model. To design graphene layer, we incorporate complex conductivity with a small thickness of δ = 0.5 nm defined as,

$$\varepsilon_g = 1 + \frac{i\sigma_g}{\omega\varepsilon_0\,\delta} \tag{6.1}$$

where, ε_0 is the free space permittivity. In the terahertz regime, the complex surface conductivity of graphene at the room temperature T = 300 K can be derived by the Kubo formula as

$$\sigma_g(\omega) = \frac{e^2 E_F}{\hbar^2\pi}\frac{i}{\omega - i\tau^{-1}} \tag{6.2}$$

where $\tau = (\mu E_F)/(ev_f^2)$ is the carrier relaxation time and E_F is the Fermi energy of graphene. As evident from Eq. (2), the surface conductivity of the graphene is related to Fermi energy or chemical potential, which can be regulated by applying a gate voltage or chemical doping. In our design, the metallic gold ground plane can be used as a reference to apply the bias voltage. As a natural consequence, the graphene nanoribbon's electromagnetic response can be controlled by varying Fermi energy (E_F). The relative permittivity of dielectric material is ε_r= 3.9 and the gold conductivity is assumed to be σ= 4.561 $\times 10^7 S/m$. The bottom gold plate is thick enough to block the incident terahertz wave. In the absence of transmission, the absorption can be eval-

uated from A=1-R, where A is the absorption and R is the reflection obtained from scattering (S) parameter using: R= $|S_{11}|^2$, numerically calculated by the CST software. The proposed structure shown in Fig. 6.1 is simulated for the normal incidence of the

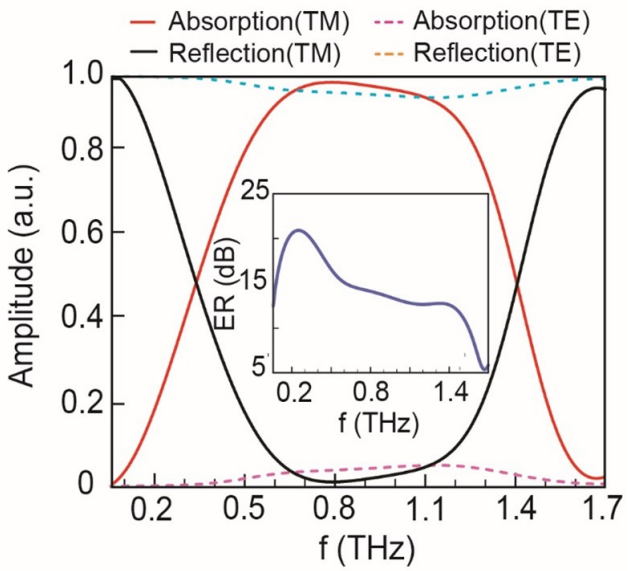

Figure 6.2: Numerically calculated absorption and reflection spectral characteristics for both transverse magnetic (TM) and transverse electric (TE) modes. The solid red and black line depicts the absorption and reflection spectrum of the proposed broadband metamaterial absorber for TM mode, while the dotted magenta and cyan colored lines represent the absorption and reflection response for TE mode, respectively. The inset plot represents the extinction ratio (ER) shown using blue solid trace.

electromagnetic wave. For Fermi energy E_F= 1 eV, the numerically evaluated reflection and absorption curves for both transverse magnetic (TM) and transverse electric (TE) modes are represented in Fig. 6.2. For TM mode, there is maximum absorption of 99% in the range of 0.72 THz to 0.9 THz. In contrast, we get only 5% peak absorptivity for TE mode, indicating that the proposed absorber is highly polarization sensitive. Meanwhile, the transmission is close to zero in the entire frequency band. For analyzing the polarization sensitivity of the metamaterial absorber, extinction ratio (ER) is one of the important parameters. The ER is defined as the ratio of absorption for TM and TE polarized waves. The numerically calculated ER is shown in the inset of Fig. 6.2. It can be clearly seen that ER can be electrically modulated from 5 dB to as high as 20.5 dB. Thus, our proposed metamaterial absorber can function as a tunable dual

THz polarizer with an extinction ratio of up to 20.5 dB.

6.4 Role of graphene nanoribbons and dielectric spacer in broadband absorption

In order to understand the effect of each layer on the performance of the proposed metamaterial absorber, we first investigate the role of graphene nanoribbons. Using effective medium approach, we assumed the periodic array of GNRs as a homogenized effective medium having the same thickness (δ= 0.5 nm). Using EMT, the effective permittivity of graphene-air homogenized medium can be calculated by the mixing formulae [153]:

$$\varepsilon_{\perp} = f\varepsilon_g + (1-f)\varepsilon_d \tag{6.3}$$

$$\varepsilon_{\parallel} = (f\varepsilon_g^{-1} + (1-f)\varepsilon_d^{-1})^{-1} \tag{6.4}$$

where $\varepsilon_{\parallel}$ and $\varepsilon_{\perp}$ represent permittivities for the electric field components perpendicular and parallel to the optical axis, respectively; $f = w_g/\Delta$ is the graphene filling fraction; ε_d is the permittivity of dielectric (air); and ε_g is the permittivity of graphene. For our design, we consider a filling ratio of 0.5 (w_g= 2 μm and Δ= 4 μm). The parallel and perpendicular components of effective permittivity of graphene-air homogenized medium for different Fermi energies are shown in Figs. 6.3(a) 6.3(c). Note that parallel component of graphene-air effective medium is considered along the length of nanoribbons while perpendicular component is taken along the width of nanoribbons (as shown in Fig. 6.3). In Figs. 6.3(a) and 6.3(b), it is evident that the parallel component of permittivity ($\varepsilon_{\parallel}$) changes with frequency, while in Fig. 6.3(c), the perpendicular component of permittivity ($\varepsilon_{\perp}$) almost remains constant. In Eq.(6.3), we found that frequency-dependent graphene permittivity (ε_g) plays a major role in calculating the parallel component of effective permittivity ($\varepsilon_{\parallel}$). Whereas, in Eq.(6.4), constant dielectric permittivity (ε_d) plays a dominant role in determining the perpendicular component of effective permittivity ($\varepsilon_{\perp}$). Therefore, the variation of $\varepsilon_{\parallel}$ with frequency for

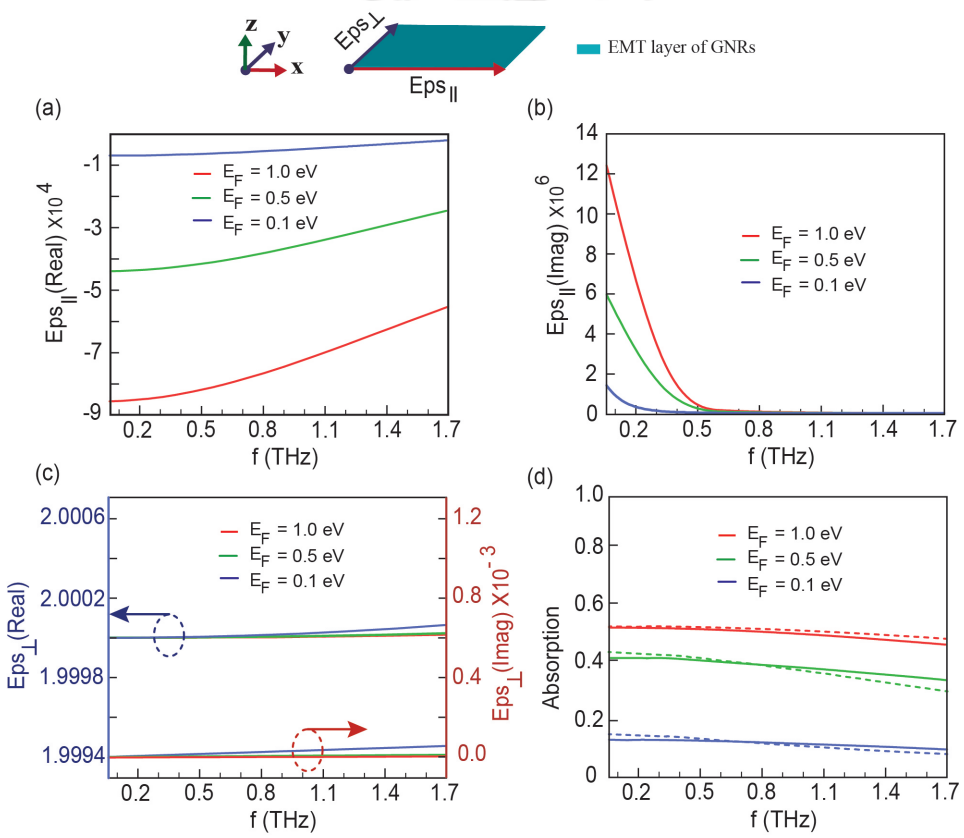

Figure 6.3: Effective medium approximation for graphene-air homogenized medium showing (a) real and (b) imaginary parts of parallel component of effective permittivity and (c) perpendicular component of effective permittivity, for different Fermi energies. (d) Theoretically and numerically calculated absorption characteristics of graphene-air homogenized medium and free-standing nanoribbons, respectively, for different Fermi energies. Red, green, and blue traces correspond to graphene Fermi energy, $E_F = 1\ eV$, $E_F = 0.5\ eV$ and $E_F = 0.1\ eV$, respectively. Note that the solid line indicates numerical results while dashed line depicts the theoretical findings.

a given Fermi Energy can result in tunable absorption. Based on the above understanding, we theoretically calculated the absorption characteristics of graphene-air homogenized medium and compared those with the numerically computed absorption response of free-standing nanoribbons for different Fermi energies. We use the transfer matrix method (TMM) to evaluate the absorption response by assuming the homogenized medium as linear and non-magnetic [154]. Detailed calculations of absorption spectra are provided in the appendix section. The solid and dashed lines in Fig. 6.3(d) indicate numerically and theoretically calculated absorption spectra, respectively. The blue and green solid curves indicate the graphene permittivity for Fermi energy 0.1 eV and 0.5 eV, respectively, while red colored solid line represents the graphene permittivity for 1 eV. It is clear that for all three Fermi energies, the absorption spectra match well the theoretical findings. For E_F = 1 eV, the absorption of the graphene ribbon is nearly 50%, and it gradually decreases for higher frequencies. In order to enhance ab-

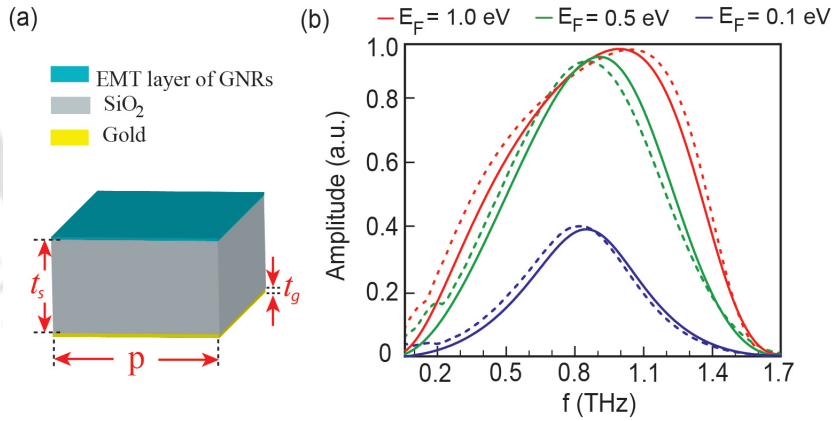

Figure 6.4: (a) A 3D view of our GNRs-SiO_2-Au unit cell structure depicting equivalent theoretical model based on effective medium theory (EMT), and (b) the numerically and theoretically obtained absorption spectra at three different fermi energies: E_F= 1 eV (red), E_F= 0.5 eV (green), and E_F= 0.1 eV (blue). The solid and dashed lines indicate numerically and theoretically calculated absorption spectra, respectively. Note that in (a) t_s= 45 µm, t_g= 0.2 µm, and p = 46 µm.

sorption obtained from free-standing graphene nanoribbons, we combined GNRs with SiO_2 dielectric and gold metallic ground plane. In Fig. 6.4(a), GNRs-SiO_2-Au assembly can be considered a partially reflecting mirror at the top, a dielectric resonator cavity at the center, and a fully reflecting metallic mirror at the bottom. The arrangement

forms a lossy Fabry-Perot (FP) cavity giving the FP resonance induced broadband absorption [11, 155]. The numerically and theoretically calculated absorption spectra for GNRs-SiO_2-Au configuration are shown in Fig. 6.4(b) using solid and dashed lines, respectively. The theoretical absorption has been calculated from the Eq. $(A.14)$ by considering GNRs-SiO_2-Au configuration as stack of four boundaries. From the figures, it may be noted that theoretical and numerical findings follow a similar trend. Further, it is apparent from the figure that an increase in the Fermi energy of the GNRs enhances the absorption amplitude along with a slight lateral shift in resonance frequencies. This shift appears due to the increased conductivity of GNRs when Fermi energy is increased.

6.5 Tunable broadband absorption with dielectric metamaterial structures

We introduced frustum-shaped dielectric (SiO_2) at the top to further broaden the absorption response, as shown in Fig. 6.1. We numerically evaluated the effect of different values of Fermi energy, E_F= 0.1 eV, 0.5 eV, and 1 eV on the absorption characteristics, as depicted in Fig. 6.5. The absorption is less than 30% for Fermi energy E_F= 0.1 eV but for E_F= 1 eV, absorption increases up to 99%. The increase in the Fermi energy causes the absorption amplitude to increase and enhances the width of the absorption band. We now examine the absorption characteristics of our proposed design through EMT and TMM. As per our previous discussion in the case of graphene nanoribbons, the absorption depends upon the direction of polarization of the incident terahertz as it varies with $\varepsilon_{\parallel}$ changes with frequency, however, $\varepsilon_{\perp}$ remains the same. Therefore, in EMT approximation, we assume graphene nanoribbons to be a homogeneous layer with effective permittivity given by Eq.(6.3). The top layer in our geometry comprises of a 2D period array of frustum-shaped SiO_2 structures surrounded by air medium. Hence, it is approximated as a 2D period array of alternative high and low permittivity anisotropic medium with effective permittivity given by Eq.(6.4) [157]. Here, the

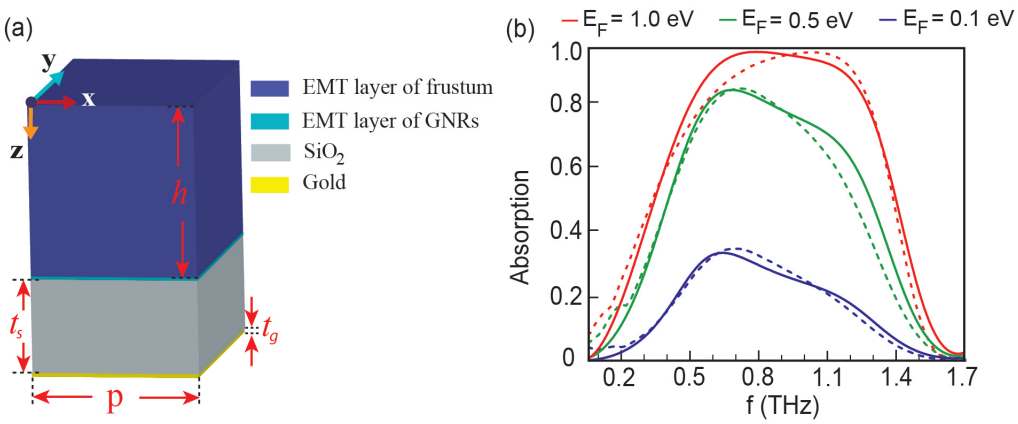

Figure 6.5: Three-dimensional views of our proposed metamaterial absorber depicting a unit cell (a) equivalent theoretical model based on effective medium theory (EMT), and (b) the numerically and theoretically obtained absorption spectra at three different fermi energies: E_F= 1 eV (red), E_F= 0.5 eV (green), and E_F= 0.1 eV (blue). The solid and dashed lines indicate numerically and theoretically calculated absorption spectra, respectively. Note that in (a) the parameter of the proposed metamaterial absorber is: h= 60 μm, t_s= 45 μm, t_g= 0.2 μm, and p = 46 μm. The thicknesses of EMT layer of frustum and GNRs are same as that of top SiO_2 layer and GNRs in the proposed structure.

filling ratio (f) is given as: f = volume of frustum / (volume of frustum + volume of air medium) = 0.48. Now we apply TMM by assuming our design as a stack of four layers (EMT layer of frustum-EMT layer of GNRs-SiO_2-Au), as shown in Fig. 6.5(a) [154]. We consider a plane wave of linear polarization incident on top of our four-layer stack. We have calculated the theoretical absorption from the Eq. (A.14) by considering full structure as stack of five boundaries. The theoretically calculated absorption spectra obtained using EMT and TMM for E_F= 0.1 eV, 0.5 eV and 1 eV are shown in Fig. 6.5(b) with different coloured dashed lines. We can see that absorption spectra obtained using theory are in good agreement with the simulation results.

To understand the role of frustum shaped structures, we numerically examined electric field distribution using color arrow plots at eight different frequencies between 0.5 THz and 1.2 THz, as shown in Fig. 6.6. From 0.6 to 1.1 THz, the anti-clockwise whirling of electric field arrows reveal that the incident electromagnetic radiation is harvested at different parts of the top SiO_2 layer. At 0.6 THz, these electric modes are formed at the base of the top SiO_2 layer, which gradually shifts upward and finally reaches the top at 1.1 THz. At 0.5 THz, we could see strong electric field localization in

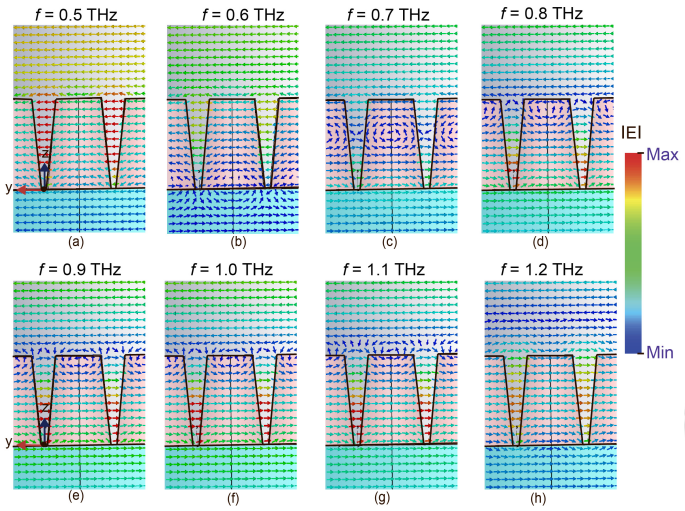

Figure 6.6: Numerically calculated normalized electric field distribution of our frustum-shaped terahertz metamaterial absorber in x-z plane at eight arbitrarily chosen frequencies at (a) f = 0.5 THz (b) f = 0.6 THz, (c) f = 0.7 THz (d) f = 0.8 THz, (e) f = 0.9 THz (f) f = 1.0 THz, (g) f = 1.1 THz, and (h) f = 1.2 THz.

the air gap between the adjacent frustum-shaped top SiO_2 blocks. This indicates that only the top SiO_2 layer plays a significant role in the broadband absorption at lower frequencies. Whereas at 1.2 THz, these electric fields are mainly localized at the interface of top and bottom SiO_2 layers, indicating that both these layers contribute to the broadband absorption at higher frequencies. Thus, the formation of overlapping electric modes results in a continuous broadband absorption from 0.5 to 1.2 THz frequency band. Next, we examine the role of dielectric (SiO_2) spacer thickness on the absorption response. In Fig. 6.7(a), we present a contour plot of the numerically calculated absorption for varying SiO_2 spacer thickness (t_s). We varied the spacer thickness between 40 µm and 50 µm for fixed parameters of metamaterial absorber as, r_1= 21 µm, r_2= 15 µm, h= 60 µm, E_F= 1 eV, and p= 46 µm. In Fig. 6.7(a), one may notice the narrowing of the absorption spectra and shift in the absorption peak towards a lower frequency side with increased spacer thickness, satisfying the Fabry-Perot resonance condition [158]. For an optimal design with broadband response, we chose dielectric spacer thickness as 45 µm, which gives more than 90% absorption from 0.6 to 1.2 THz, indicated by a black horizontal arrow in Fig. 6.7(a). To further demonstrate the tunability in absorp-

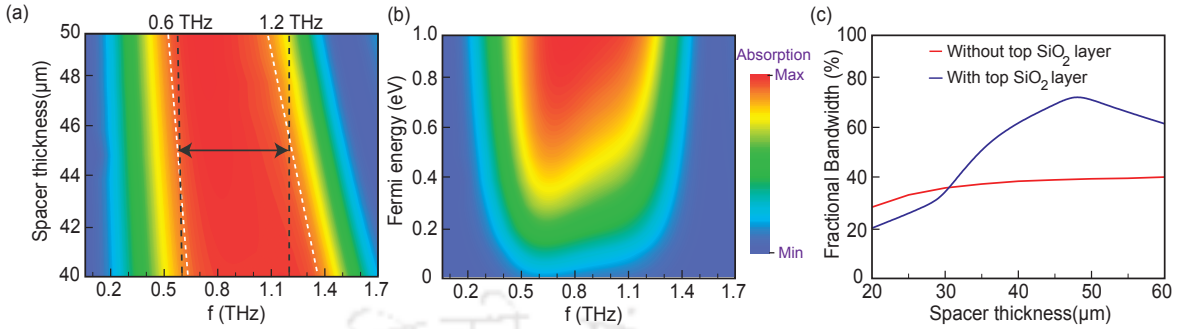

Figure 6.7: Modulation of absorption bandwidth for fixed parameters of proposed terahertz metamaterial absorber: r_1= 21 μm, r_2=15 μm, h= 60 μm, t_g= 0.2 μm, and p = 46 μm. (a) Contour plot for different dielectric spacer thicknesses (t_s) of the dielectric (SiO_2) material. (b) Contour plot for different Fermi energy (E_F) of the graphene. (c) Fractional bandwidth versus spacer thickness: with and without top SiO_2 frustum layer. Note that the color bar shows the amplitude of the absorption signal. In (a), the black horizontal arrow represents 0.6 – 1.2 THz frequency band over which absorption is above 90% for an optimal dielectric spacer thickness of 45 μm.

tion modulation, we varied the Fermi energy of the graphene (E_F) from 0 eV to 1 eV taking t_s= 45 μm and keeping the other parameters as mentioned above. Fig. 6.7(b) reveals that the absorption spectra can be modulated by varying the Fermi energy in the dielectric-GNRs-dielectric-metal structure. It is observed that the absorption amplitude decreases significantly when E_F varies from 0.3 to 0 eV. For E_F= 0 eV, there is no absorption in the entire frequency band. At E_F= 0.6 eV, the absorption peak reaches up to 90% over 0.6 - 1.2 THz frequency band. This significant increment in the absorption with an increase in the Fermi energy can be attributed to the decrease in the real part of graphene permittivity, which makes it behave more like a metal. With a further increase in the Fermi energy up to 1 eV, a near-unity absorption can be achieved in the 0.72 - 0.9 THz band.

To evaluate the performance of our proposed structure, we introduce fractional bandwidth, which is defined as the ratio of absorption bandwidth with more than 90% absorptivity and the peak absorption frequency (f_p). In this work, absorptivity is over 90% between 0.6 THz and 1.2 THz. Further, the peak absorption frequency (f_p) is the frequency at which the absorption amplitude is maximum [159]. Here, the maximum absorption came out to be 99.9% at 0.825 THz. Therefore, we have chosen 0.825 THz

as the peak absorption frequency. Thus, keeping in view the absorption bandwidth and the peak absorption frequency, we could achieve a fractional bandwidth of 72.7%. Further, to understand the role of top SiO_2 frustum layer, we compare fractional bandwidth with (blue curve) and without (red curve) the top layer as shown in Fig. 6.7(c). It can be inferred from the red curve that with an increase in spacer thickness, the absorption bandwidth first increases and then saturates to some extent, which follows the thickness-bandwidth limit [160]. However, the fractional bandwidth is quite low. For instance, a spacer thickness of 20 μm gives 90% absorptivity over 1.96 – 2.57 THz band with a fractional bandwidth of 26.05 %. Whereas, 60 μm thick spacer layer provides the same absorptivity over 0.56 – 0.84 THz band with a fractional bandwidth of 38.75 %. Now, with the addition of the top layer, we observed that the fractional bandwidth first increases, reaches a maximum, and then gradually decreases (see the blue curve). This observation does not comply with the general rule of thickness-bandwidth limit [160]. For example, a spacer thickness of 20 μm gives a fractional bandwidth of 20.24 %. Whereas, 60 μm thick spacer layer provides a fractional bandwidth of 64.57 %. These results reveal that the addition of top SiO_2 frustum layer significantly improves the fractional bandwidth. To achieve high fractional bandwidth, we have chosen a 45 μm thick spacer layer which gives 90 % absorptivity over 0.60 – 1.20 THz band with a fractional bandwidth of 72.72 %.

Next, we compare the performance of our proposed structure with other studies on graphene-assisted broadband THz absorbers reported in the literature (see Table.6.1). The comparison table indicates that our design offers much higher fractional bandwidth and provides a nearly perfect absorption over the considered spectral window. Here fractional bandwidth is defined as the ratio of absorption bandwidth with more than 90% absorptivity and the center frequency (f_c). In our case, absorptivity is over 90% between 0.6 THz and 1.2 THz, and the center frequency is 0.825 THz which results in 72.7% fractional bandwidth. In addition, we could achieve an extinction ratio up to 20.5 dB, which is higher than the values recently reported in the literature [166, 167].

Ref.	Absorption Band (THz)	Absorptivity	Fractional Bandwidth (%)	Structure
[161]	1.3 – 2.2	> 90%	48	Periodic arrays of dielectric bricks
[162]	1.57 – 3.07	> 90%	65	Graphene incorporated alongside arrays of elliptic dielectric cylinders
[163]	4.4 – 14	> 95%	20	Periodic gold disks with graphene sheet
[164]	1.05 – 1.6	99%	37.41	Pair of graphene square rings with VO_2
[165]	1.10 – 1.86	90%	51	Graphene concentric rings and cross shaped geometry
This work	0.72 – 0.9	**99%**	**72.7**	Frustum shaped dielectric with a periodic array of graphene nanoribbons

Table 6.1: Comparison table of the proposed absorber with a few recently reported metamaterial absorbers in terahertz regime.

Further, our tunable and broadband design provides a polarization sensitive terahertz metamaterial absorber.

6.6 Discussions

We presented a tunable polarization sensitive metamaterial absorber based on an array of graphene nanoribbons through theory and simulations. The design comprises frustum-shaped periodic dielectric pillars with graphene nanoribbons deposited over an ultrathin metal-backed dielectric spacer. Our design offers a broadband response with over 90% absorptivity from 0.6 THz to 1.2 THz and 72.7% fractional bandwidth for TM polarization. In contrast, a negligible absorption for TE polarization is observed. Our observation indicates a very high extinction ratio of 20.5 dB for the orthogonal polarization direction of incident terahertz. We examined the effect of each layer on the performance of the proposed configuration. We have first investigated the role of free-standing graphene nanoribbons on broadband absorption and found nearly 50% absorbance for Fermi energy, $E_F = 1\ eV$. When combined with the SiO_2 dielectric space

and gold metallic ground plane, the absorption gets enhanced to nearly perfect value. It is observed that the addition of a frustum-shaped dielectric (SiO_2) on the top broadens the absorption response. The addition of a frustum shaped dielectric geometry on the top of graphene ribbons structure gives a broadband absorption response from 0.6 THz to 1.2 THz. The proposed structure gives near unity absorption in the range of 0.72 THz to 0.9 THz. Further, we have shown that the absorption can be tuned by changing the Fermi energy of graphene nanoribbons. Our theoretical results based on effective medium theory and transfer matrix method match well with the numerical findings. Electric field distribution has also been studied to understand the role of both dielectric layers, which reveals their importance in broadband absorption. The proposed broadband absorption modulator and important findings reported in this chapter could be crucial for developing terahertz broadband optical components.

7

Conclusion and Future aspects

Contents

This chapter summarizes the work of the thesis, highlighting important findings and contributions in designing of plasmonic metamaterials based sensors and modulators. Section 7.1 provides a summary of contributions and discussions. Section 7.2 concludes the chapter by listing possible directions for future research.

7.1 Summary of contributions

The motive of thesis work has been to explore the possibility of utilising plasmonic metamaterials for designing and building the sensors and modulators for next generation. This chapter presents contributions from thesis work as follows:

In chapter 1, we introduced the outline of the thesis discussing the motivation, scope of this work, major contribution of this thesis and its organization.

In chapter 2, we examined the refractive index sensor ability of the terahertz surface plasmon modes supported by a planar plasmonic terahertz (THz) waveguide. The waveguide comprising of one-dimensional array of periodically arranged subwavelength scale pyramidal corrugations was designed. It was found to support highly confined modes along with the corrugated pattern. We have analyzed the dispersion property and quality factor of the fundamental as well as higher-order modes of the waveguide. In order to examine sensor capability, we used analytes of different refractive indices and observed a corresponding frequency shift. We further analyze the sensitivity of all the modes for the given volume of analyte and compared their sensing performance. We have employed the semi-analytical model to understand the numerical observations. The proposed waveguide approach has the potential to build highly sensitive refractive index sensors at terahertz frequencies.

In chapter 3, we investigated terahertz surface plasmons propagation in a planar waveguide comprising asymmetric resonators placed in close proximity. The waveguide is designed to support surface plasmon polaritons (SPPs) at two distinct terahertz frequencies, ω_1 and ω_2, which are near to each other. This is accomplished by carefully designing the unit cell comprising of two resonators with slightly different sizes.

The resonators in the form of rectangular apertures are placed along the transverse direction in the near field regime. We observe an absorption window surrounded by two transmission resonances which are coupled to each other. As the resonators are moved apart, we observe a switching from the coupled to an uncoupled resonance state. The absorption window can be tuned by changing the resonance frequency of the resonators, which depends upon its structural parameters. We have employed a theoretical model to understand the coupling mechanism between the resonators and the dispersive behavior resulting in absorption window. The proposed study is significant in the construction of planar terahertz components such as slow lights systems, buffers, etc. where steep dispersion plays a vital role.

In chapter 4, we investigated double slot waveguide configuration to explore the actively tunable plasmon induced transparency (PIT) effect in the terahertz regime. One of the slot structures is filled with a dielectric material of certain refractive index which causes a slight shift in the its resonance frequency as compared to the unfilled slot. The two frequencies say, ω_1 and ω_2 from the unfilled and filled slots, respectively act as the bright resonators. The PIT effect is observed due to the destructive interference of these two modes. The electric field profiles clearly indicate the emergence of the PIT effect. We observe that the transparency effect can be tuned by varying the refractive index of the dielectric material, which promises an active and tunable control of the effect without changing the physical dimensions. We have employed an analytical model based upon the coupled harmonic oscillators to understand the coupling mechanism between the two resonators resulting in PIT effect and validate numerical findings. The proposed study has significance in the construction of tunable terahertz components such as slow light systems, buffers, etc. where an active control of optical properties is desirable.

In chapter 5, we examine PIT effect in a parallel plate waveguide (PPWG) comprising of two similar pyramidal shaped grooves. One of the grooves is filled with air, while the other is filled with a dielectric material whose refractive index can be var-

ied. The resonant frequencies corresponding to the air and dielectric grooves in the proposed configuration results in the transparency window which can be modulated with the refractive index of the dielectric material. The approach provides flexibility to control transparency effect in a waveguide configuration without changing physical dimensions. We examined field profiles in the transparency region to clearly depict the PIT effect. We have employed an analytical model based upon the three-level plasmonic model to validate our numerical findings. Further, we examined the switching and tunability of transparency effect by including silicon layers between the grooves whose conductivity can be varied. Tunable response in plasmon induced transparency effect in terahertz waveguides are of great significance in the construction of active terahertz waveguide components.

In chapter 6, we report a theoretical approach for designing a tunable broadband metamaterial absorber in terahertz regime. The design comprises frustum shaped dielectric (SiO_2) metamaterial structures on top of a one-dimensional period array of graphene nanoribbons deposited over the ultrathin metal-backed dielectric. For TM polarization, our design offers a near-perfect absorption in the range of 0.72 THz to 0.9 THz with 72.7% fractional bandwidth. On the contrary, we get a negligible absorption for the TE polarization of the incident light, thereby giving an extinction ratio up to 20.5 dB. The excitation of plasmons in graphene nanoribbons combined with resonance induced by the graphene-dielectric-metal cavity leads to nearly perfect broadband absorption for the TM polarized radiation. Further, modulation of the absorption spectrum has been achieved by changing graphene conductivity with the help of its Fermi energy. A theoretical model based on effective medium theory and transfer matrix method has been presented to validate absorption response for various Fermi energy values of the graphene. The figure of merit of our design can outperform some of the recently reported tunable metamaterial absorbers.

7.2 Future Aspects

Terahertz plasmonics and metamaterials are currently considered the best prospects for creating efficient terahertz devices, including modulators and sensors. In order to develop more efficient and reliable terahertz devices, here we suggest some possible directions to extend this work.

• In the direction of the plasmonic waveguide, we have mainly focused on the first (fundamental) mode and the second-order mode. However, plasmon waveguides can be explored for the excitation of higher-order modes. In our study, we found that the second-order mode shows better sensitivity than the fundamental mode so, therefore detailed investigations of all the modes supported by plasmonic waveguide can be examined for their potential in sensing. One can also perform a detailed dispersion analysis to understand the propagation characteristics of higher order modes. Technological developments based upon the proposed research designs can be made for label free sensing.

• From the point of view of near-field coupling, a strong coupling between the resonators was observed in our study. One can use the near field coupled effect to study various phenomena, including electromagnetically induced transparency, electromagnetically induced absorption, where dispersion properties can be tuned by varying the near-field coupling between the resonators. The research in this direction can be helpful in developing devices such as modulators, slow light devices, and switches.

• Furthermore, in the context of our study on plasmon induced transparency in double slot waveguide, one can use this approach to construct a plasmonic waveguide by designing an array of slot resonators in a parallel plate waveguide. This approach can result in more prominent effects. A similar strategy can be adopted to actively tune the transparency window by filling the array of slots with the dielectric material which can be significant in building active photonic components.

• The actively tunable spectral response can also be achieved by introducing the graphene sheet in close proximity to the resonators of a plasmonic terahertz waveguide. The graphene sheet has been shown to exhibit plasmon frequency at the terahertz frequencies and this can potentially tune the resonances of plasmonic corrugated waveguides under near field effect.

• The higher carrier frequency and greater bandwidth are desirable to meet the increasing demand in data transfer. Terahertz dielectric metamaterial could be significant in this direction. Our study can be extended to design the unique dielectric metamaterial broadband modulators for the desired bandwidth where one can actively tune the frequency window as well. The use of 2D materials and exotic materials can pave the way for building tunable broadband terahertz photonic components.

A

Appendix

A.1 Transfer Matrix Method

Transfer matrix method solves electric field and magnetic field equations at the boundary. Any wave that is incident on the top of any multilayer structure undergoes multiple transmission, reflection and absorption at different interface and finally gets transmitted or reflected and that can be determined using the TMM. It basically solves the Maxwell and Fresnel equations at the boundary across the multilayer stack. The field at the boundaries of graphene air homogenized layer can be understand by the Fig. A.1. Each wave E_{rI}, E'_{rII}, E_{tII}, etc. represents the result of all waves that may move in that direction at that point in the medium. According to the boundary conditions, the tangential components of both the electric field (E) and the magnetic field (H) must be continuous across the boundaries. At boundary I,

$$E_I = E_{iI} + E_{rI} = E_{tI} + E_{rII} \tag{A.1}$$

and

$$H_I = \sqrt{\varepsilon_0/\mu_0}(E_{iI} - E_{rI} n_0 \cos\theta_{iI}) = \sqrt{\varepsilon_0/\mu_0}(E'_t - E'_{rII} n_1 \cos\theta_{iII}) \tag{A.2}$$

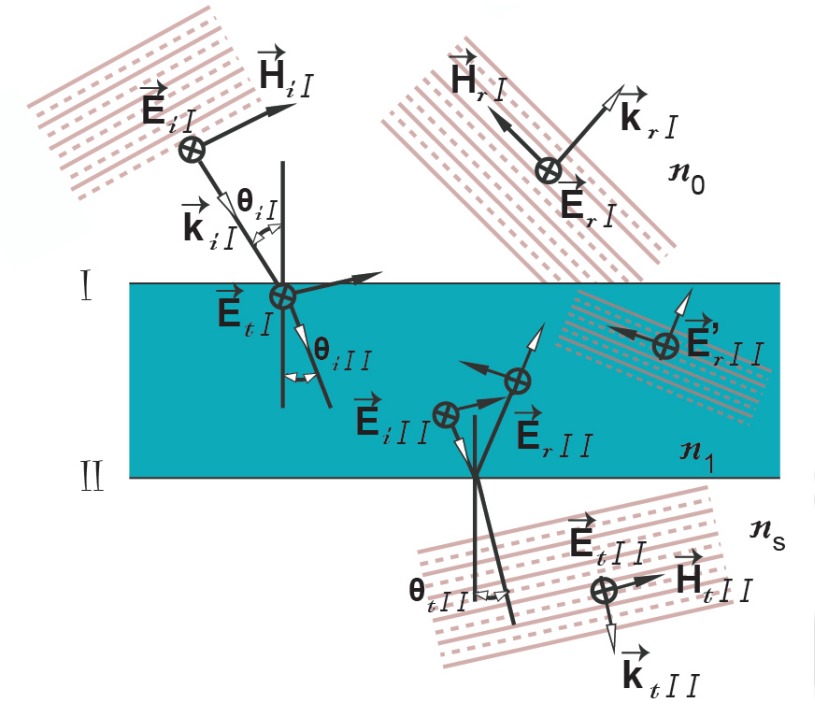

Figure A.1: Field schematic at the two boundaries

Similarly, at II boundary,

$$E_{II} = E_{iII} + E_{rII} = E_{tII} \tag{A.3}$$

and

$$H_{II} = \sqrt{\varepsilon_0/\mu_0}(E_{iII} - E_{rII} n_1 \cos\theta_{iII}) = \sqrt{\varepsilon_0/\mu_0}(E_{tII} - E'_{rII}) n_s \cos\theta_{tII} \tag{A.4}$$

Given that the wave across the film experiences a phase shift of $k_0(2n_1 d cos\theta_{iII})/2$, which will be represented by $k_0 h$, so Eq.(A.3) and Eq.(A.4) can be described as,

$$E_{II} = E_{tI} exp^{-ik_0 h} + E'_{rII} exp^{ik_0 h} \tag{A.5}$$

and

$$H_{II} = (E_{tI} exp^{-ik_0 h} - E'_{rII} exp^{ik_0 h}) \sqrt{\varepsilon_0/\mu_0} n_1 \cos\theta_{iII} \tag{A.6}$$

After substituting above values in Eq.(A.1) and (A.2), it gives

$$E_I = E_{II} cosk_0 h + H_{II}(isink_0 h)/\gamma_1 \tag{A.7}$$

and

$$H_I = E_{II}\gamma_1(isink_0h) + H_{II}cosk_0h \tag{A.8}$$

where,

$$\gamma_1 = \sqrt{\varepsilon_0/\mu_0}n_1cos\theta_{iI}$$

In matrix notation, above equation can be written as,

$$\begin{pmatrix} E_I \\ H_I \end{pmatrix} = \begin{pmatrix} cosk_0h & (isink_0h)/\gamma_1 \\ \gamma_1 isink_0h & cosk_0h \end{pmatrix} \begin{pmatrix} E_{II} \\ H_{II} \end{pmatrix} \tag{A.9}$$

$$\begin{pmatrix} E_I \\ H_I \end{pmatrix} = M_1 \begin{pmatrix} E_{II} \\ H_{II} \end{pmatrix} \tag{A.10}$$

Here, M_1 is the characteristics matrix related to fields at the adjacent two boundaries. In general, if "l" is the number of layers, each with a particular value of n and h, then the first and the last boundaries are related by

$$\begin{pmatrix} E_I \\ H_I \end{pmatrix} = M_1M_{II}.....M_l \begin{pmatrix} E_{l+1} \\ H_{l+1} \end{pmatrix} \tag{A.11}$$

After expanding the matrices, we have calculated the reflection and transmission coefficient by the given relation

$$r = \frac{E_{rI}}{E_{iI}} = \frac{\gamma_0m_{11} + \gamma_0\gamma_sm_{12} - m_{21} - \gamma_sm_{22}}{\gamma_0m_{11} + \gamma_0\gamma_sm_{12} + m_{21} + \gamma_sm_{22}} \tag{A.12}$$

and

$$t = \frac{E_{tII}}{E_{iI}} = \frac{2\gamma_0}{\gamma_0m_{11} + \gamma_0\gamma_sm_{12} + m_{21} + \gamma_sm_{22}} \tag{A.13}$$

where γ_0 and γ_s, are the admittance for initial and final boundaries, can be written as

$$\gamma_1 = \sqrt{\varepsilon_0/\mu_0}n_0cos\theta_{iI}$$

and

$$\gamma_s = \sqrt{\varepsilon_0/\mu_0}n_scos\theta_{tII}$$

. The theoretical absorption can be calculated by

$$a = 1 - |r|^2 - |t|^2 \tag{A.14}$$

For graphene-air homogenized layer, we have calculated the characteristic matrix then substitute the resulting matrix elements into the above Eq.(A.12) and Eq.(A.13). Using Eq. (A.14), one can calculate the absorption for graphene-air homogenized layer.

Bibliography

[1] De Lucia, Frank C., Douglas T. Petkie, and Henry O. Everitt. "A double resonance approach to submillimeter/terahertz remote sensing at atmospheric pressure." IEEE journal of quantum electronics 45.2 (2008): 163-170.

[2] Liu, Jingle, et al. "Broadband terahertz wave remote sensing using coherent manipulation of fluorescence from asymmetrically ionized gases." Nature Photonics 4.9 (2010): 627-631.

[3] Xin, Feifei, Hongyan Su, and Yong Xiao. "Terahertz imaging system for remote sensing and security applications." Proceedings of 2014 3rd Asia-Pacific Conference on Antennas and Propagation. IEEE, 2014.

[4] Chan, W.L., J. Deibel, and D.M. Mittleman, Imaging with terahertz radiation. Reports on progress in physics, 2007. 70(8): p. 1325.

[5] Ogawa, Y., et al., Terahertz sensing for ensuring the safety and security. PIERS online, 2008. 4(3): p. 396-400.

[6] Song, Q., et al., Fast continuous terahertz wave imaging system for security. Optics Communications, 2009. 282(10): p. 2019-2022.

[7] Markelz, A., A. Roitberg, and E.J. Heilweil, Pulsed terahertz spectroscopy of DNA, bovine serum albumin and collagen between 0.1 and 2.0 THz. Chemical Physics Letters, 2000. 320(1-2): p. 42-48.

[8] Jansen, C., et al., Terahertz imaging: applications and perspectives.

[9] Jepsen, P.U., D.G. Cooke, and M. Koch, Terahertz spectroscopy and imaging–Modern techniques and applications. Laser & Photonics Reviews, 2011. 5(1): p. 124-166.

[10] Pickwell, E. and V. Wallace, Biomedical applications of terahertz technology. Journal of Physics D: Applied Physics, 2006. 39(17): p. R301.

[11] Yang, X., et al., Biomedical applications of terahertz spectroscopy and imaging. Trends in biotechnology, 2016. 34(10): p. 810-824.

[12] Davies, A., E.H. Linfield, and M.B. Johnston, The development of terahertz sources and their applications. Physics in Medicine & Biology, 2002. 47(21): p. 3679.

[13] Tonouchi, M., Cutting-edge terahertz technology. Nature photonics, 2007. 1(2): p. 97-105.

[14] Mukherjee, P. and B. Gupta, Terahertz (THz) frequency sources and antennas-A brief review. International Journal of Infrared and Millimeter Waves, 2008. 29(12): p. 1091-1102.

[15] Lewen, F., et al., Terahertz laser sideband spectroscopy with backward wave oscillators. Journal of Molecular Spectroscopy, 1997. 183(1): p. 207-209.

[16] Toreev, A., V. Fedorov, and E. Patrusheva, Millimeter-wave extended interaction klystron. Journal of Communications Technology and Electronics, 2009. 54(8): p. 952-958.

[17] Bhattacharjee, S., et al., Folded waveguide traveling-wave tube sources for terahertz radiation. IEEE transactions on plasma science, 2004. 32(3): p. 1002-1014.

[18] Booske, J.H., et al., Vacuum electronic high power terahertz sources. IEEE Transactions on Terahertz Science and Technology, 2011. 1(1): p. 54-75.

[19] Yang, L.-A., et al., Improved negative differential mobility model of GaN and AlGaN for a terahertz Gunn diode. IEEE Transactions on Electron Devices, 2011. 58(4): p. 1076-1083.

[20] Knap, W., et al., Terahertz emission by plasma waves in 60 nm gate high electron mobility transistors. Applied Physics Letters, 2004. 84(13): p. 2331-2333.

[21] Maestrini, A., et al., A frequency-multiplied source with more than 1 mW of power across the 840–900-GHz band. IEEE transactions on microwave theory and techniques, 2010. 58(7): p. 1925-1932.

[22] Suzuki, S., et al., Fundamental oscillation of resonant tunneling diodes above 1 THz at room temperature. Applied Physics Letters, 2010. 97(24): p. 242102.

[23] Walther, C., et al., Quantum cascade lasers operating from 1.2 to 1.6 THz. Applied Physics Letters, 2007. 91(13): p. 131122.

[24] Tomasino, A., et al., Wideband THz time domain spectroscopy based on optical rectification and electro-optic sampling. Scientific reports, 2013. 3(1): p. 1-8.

[25] Lewis, R.A., A review of terahertz sources. Journal of Physics D: Applied Physics, 2014. 47(37): p. 374001.

[26] Sizov, F. and A. Rogalski, THz detectors. Progress in quantum electronics, 2010. 34(5): p. 278-347.

[27] van der Valk, N.C., T. Wenckebach, and P.C. Planken, Full mathematical description of electro-optic detection in optically isotropic crystals. JOSA B, 2004. 21(3): p. 622-631.

[28] Shen, Y.-C. and P.F. Taday, Development and application of terahertz pulsed imaging for nondestructive inspection of pharmaceutical tablet. IEEE Journal of Selected Topics in Quantum Electronics, 2008. 14(2): p. 407-415.

[29] Lin, H., et al., Measurement of the intertablet coating uniformity of a pharmaceutical pan coating process with combined terahertz and optical coherence tomography in-line sensing. Journal of pharmaceutical sciences, 2017. 106(4): p. 1075-1084.

[30] May, R.K., et al., Hardness and density distributions of pharmaceutical tablets measured by terahertz pulsed imaging. Journal of pharmaceutical sciences, 2013. 102(7): p. 2179-2186.

[31] Ho, L., et al., Investigating dissolution performance critical areas on coated tablets: a case study using terahertz pulsed imaging. Journal of pharmaceutical sciences, 2010. 99(1): p. 392-402.

[32] Taday, P.F., et al., Using terahertz pulse spectroscopy to study the crystalline structure of a drug: A case study of the polymorphs of ranitidine hydrochloride. Journal of pharmaceutical sciences, 2003. 92(4): p. 831-838.

[33] Tribe, W.R., et al. Hidden object detection: security applications of terahertz technology. in Terahertz and Gigahertz Electronics and Photonics III. 2004. International Society for Optics and Photonics.

[34] Siegel, P.H., Terahertz technology in biology and medicine. IEEE transactions on microwave theory and techniques, 2004. 52(10): p. 2438-2447.

[35] Löffler, T., et al., Terahertz dark-field imaging of biomedical tissue. Optics express, 2001. 9(12): p. 616-621.

[36] Zaytsev, K.I., et al., Highly accurate in vivo terahertz spectroscopy of healthy skin: variation of refractive index and absorption coefficient along the human body. IEEE Transactions on Terahertz science and Technology, 2015. 5(5): p. 817-827.

[37] Stringer, M., et al., The analysis of human cortical bone by terahertz time-domain spectroscopy. Physics in Medicine & Biology, 2005. 50(14): p. 3211.

[38] Dobroiu, A., et al., THz-wave spectroscopy applied to the detection of illicit drugs in mail. Proceedings of the IEEE, 2007. 95(8): p. 1566-1575.

[39] Song, H.-J. and T. Nagatsuma, Present and future of terahertz communications. IEEE transactions on terahertz science and technology, 2011. 1(1): p. 256-263.

[40] Nagatsuma, T., G. Ducournau, and C.C. Renaud, Advances in terahertz communications accelerated by photonics. Nature Photonics, 2016. 10(6): p. 371-379.

[41] Masson, J.-B., A. Podzorov, and G. Gallot, Anomalies in the disappearance of the extraordinary electromagnetic transmission in subwavelength hole arrays. Optics express, 2008. 16(7): p. 4719-4730.

[42] Wang, K. and D.M. Mittleman, Metal wires for terahertz wave guiding. Nature, 2004. 432(7015): p. 376-379.

[43] Van der Valk, N.C. and P.C. Planken, Effect of a dielectric coating on terahertz surface plasmon polaritons on metal wires. Applied Physics Letters, 2005. 87(7): p. 071106.

[44] Akalin, T., A. Treizebré, and B. Bocquet, Single-wire transmission lines at terahertz frequencies. IEEE Transactions on Microwave Theory and Techniques, 2006. 54(6): p. 2762-2767.

[45] Williams, C.R., et al., Highly confined guiding of terahertz surface plasmon polaritons on structured metal surfaces. Nature Photonics, 2008. 2(3): p. 175-179.

[46] Rivas, J.G., et al., Propagation of surface plasmon polaritons on semiconductor gratings. Physical review letters, 2004. 93(25): p. 256804.

[47] Gan, C.H., H.S. Chu, and E.P. Li, Synthesis of highly confined surface plasmon modes with doped graphene sheets in the midinfrared and terahertz frequencies. Physical Review B, 2012. 85(12): p. 125431.

[48] Ishimaru, A., Electromagnetic wave propagation, radiation, and scattering: from fundamentals to applications. 2017: John Wiley & Sons.

[49] Pendry, J., L. Martin-Moreno, and F. Garcia-Vidal, Mimicking surface plasmons with structured surfaces. science, 2004. 305(5685): p. 847-848.

[50] Martín-Cano, D., et al., Domino plasmons for subwavelength terahertz circuitry. Optics Express, 2010. 18(2): p. 754-764.

[51] Kong, L.-B., et al., Enhancing spoof surface-plasmons with gradient metasurfaces. Scientific reports, 2015. 5(1): p. 1-5.

[52] Duan, J., et al., High-efficiency chirality-modulated spoof surface plasmon meta-coupler. Scientific reports, 2017. 7(1): p. 1-9.

[53] Hu, B., Q.J. Wang, and Y. Zhang, Broadly tunable one-way terahertz plasmonic waveguide based on nonreciprocal surface magneto plasmons. Optics letters, 2012. 37(11): p. 1895-1897.

[54] You, B., et al., Terahertz plasmonic waveguide based on metal rod arrays for nanofilm sensing. Optics express, 2014. 22(9): p. 11340-11350.

[55] Su, Y., et al., Enhanced confinement of terahertz surface plasmon polaritons in bulk dirac semimetal-insulator-metal waveguides. Nanoscale research letters, 2018. 13(1): p. 1-7.

[56] Ye, L., et al., Plasmonic waveguide with folded stubs for highly confined terahertz propagation and concentration. Optics express, 2017. 25(2): p. 898-906.

[57] Guo, Y.J., K. Da Xu, and X. Tang, Spoof plasmonic waveguide developed from coplanar stripline for strongly confined terahertz propagation and its application in microwave filters. Optics express, 2018. 26(8): p. 10589-10598.

[58] Yuan, M., et al., Curved terahertz surface plasmonic waveguide devices. Optics express, 2020. 28(2): p. 1987-1998.

[59] Deng, X., et al., Continuously frequency-tuneable plasmonic structures for terahertz biosensing and spectroscopy. Scientific reports, 2019. 9(1): p.

[60] Alipour, A.H. and A. Mir, Design and simulation of a high-selective plasmon-induced reflectance in coupled dielectric-metal-dielectric nano-structure for senor devices and slow light propagation. Plasmonics, 2019. 14(2): p. 511-521.

[61] Unutmaz, M.A. and M. Unlu, Terahertz spoof surface plasmon polariton waveguides: a comprehensive model with experimental verification. Scientific reports, 2019. 9(1): p. 1-8.

[62] Ma, Z., et al., Terahertz particle-in-liquid sensing with spoof surface plasmon polariton waveguides. APL Photonics, 2017. 2(11): p. 116102.

[63] Ferraro, A., et al., Guided-mode resonant narrowband terahertz filtering by periodic metallic stripe and patch arrays on cyclo-olefin substrates. Scientific reports, 2018. 8(1): p. 1-8.

[64] Guo, Y., et al., Spoof plasmonic metasurfaces with catenary dispersion for two-dimensional wide-angle focusing and imaging. Iscience, 2019. 21: p. 145-156.

[65] Huang, T.-J., et al., Far-field subwavelength resolution imaging by spatial spectrum sampling. Physical Review Applied, 2019. 12(3): p. 034046.

[66] Kumar, G., et al., Planar plasmonic terahertz waveguides based on periodically corrugated metal films. New Journal of Physics, 2011. 13(3): p. 033024.

[67] Li, S., et al., Terahertz surface plasmon polaritons on a semiconductor surface structured with periodic V-grooves. Optics express, 2013. 21(6): p. 7041-7049.

[68] Kumar, G., et al., Terahertz surface plasmon waveguide based on a one-dimensional array of silicon pillars. New Journal of Physics, 2013. 15(8): p. 085031.

[69] Kumar, G., Controlling terahertz surface plasmon properties on a periodically structured silicon surface. Journal of Spectroscopy, 2015.

[70] Li, S., et al., Plasmonic terahertz waveguide based on anisotropically etched silicon substrate. IEEE Transactions on Terahertz Science and Technology, 2014. 4(4): p. 454-458.

[71] Yang, Y., et al., Terahertz topological photonics for on-chip communication. Nature Photonics, 2020. 14(7): p. 446-451.

[72] Ren, Z., et al., Leveraging of MEMS technologies for optical metamaterials applications. Advanced Optical Materials, 2020. 8(3): p. 1900653.

[73] Dong, B., et al., Recent progress in nanoplasmonics-based integrated optical micro/nanosystems. Journal of Physics D: Applied Physics, 2020. 53(21): p. 213001.

[74] Hanham, S., et al. Exploiting plasmonics for THz and infrared sensing. in Terahertz Physics, Devices, and Systems VIII: Advanced Applications in Industry and Defense. 2014. International Society for Optics and Photonics.

[75] You, B., et al., Hybrid terahertz plasmonic waveguide for sensing applications. Optics express, 2013. 21(18): p. 21087-21096.

[76] Islam, M., et al., Terahertz plasmonic waveguide based thin film sensor. Journal of Lightwave Technology, 2017. 35(23): p. 5215-5221.

[77] Qi, J., et al., Independently tunable double Fano resonances in asymmetric MIM waveguide structure. Optics express, 2014. 22(12): p. 14688-14695.

[78] Zhan, S., et al., Tunable nanoplasmonic sensor based on the asymmetric degree of Fano resonance in MDM waveguide. Scientific reports, 2016. 6(1): p. 1-8.

[79] Zhang, Y., et al., High-sensitivity refractive index sensors based on Fano resonance in the plasmonic system of splitting ring cavity-coupled MIM waveguide with tooth cavity. Applied Physics A, 2019. 125(1): p. 1-5.

[80] Gu, L., et al., Fano resonance lineshapes in a waveguide-microring structure enabled by an air-hole. APL Photonics, 2020. 5(1): p. 016108.

[81] Wang, T., et al., Tunable polarization-nonsensitive electromagnetically induced transparency in Dirac semimetal metamaterial at terahertz frequencies. Optical Materials Express, 2019. 9(4): p. 1562-1576.

[82] Wei, B., et al., Graphene based silicon–air grating structure to realize electromagnetically-induced-transparency and slow light effect. Physics Letters A, 2017. 381(3): p. 160-165.

[83] Tao, L., et al., Gate-tunable plasmon-induced transparency modulator based on stub-resonator waveguide with epsilon-near-zero materials. Scientific reports, 2019. 9(1): p. 1-8.

[84] Xu, Q., et al., Experimental realization of an on-chip all-optical analogue to electromagnetically induced transparency. Physical review letters, 2006. 96(12): p. 123901.

[85] Zhao, W., et al., On-chip plasmon-induced transparency in THz metamaterial on a LiNbO 3 subwavelength planar waveguide. Optics express, 2019. 27(5): p. 7373-7383.

[86] Pendry, John B., et al. "Extremely low frequency plasmons in metallic mesostructures." Physical review letters 76.25 (1996): 4773.

[87] Shelby, Richard A., David R. Smith, and Seldon Schultz. "Experimental verification of a negative index of refraction." science 292.5514 (2001): 77-79.

[88] Padilla, W. J., et al. "Electrically resonant terahertz metamaterials: Theoretical and experimental investigations." Physical Review B 75.4 (2007): 041102.

[89] West, Paul R., et al. "All-dielectric subwavelength metasurface focusing lens." Optics express 22.21 (2014): 26212-26221.

[90] Yang, Yuping, et al. "Terahertz magnetic and electric Mie resonances of an all-dielectric one-dimensional grating." Applied Physics Letters 106.11 (2015): 111106.

[91] Jahani, Saman, and Zubin Jacob. "All-dielectric metamaterials." Nature nanotechnology 11.1 (2016): 23-36.

[92] Yang, Yuping, et al. "Terahertz magnetic and electric Mie resonances of an all-dielectric one-dimensional grating." Applied Physics Letters 106.11 (2015): 111106.

[93] Fan, Kebin, et al. "All-dielectric metasurface absorbers for uncooled terahertz imaging." Optica 4.6 (2017): 601-604.

[94] Wang, Yue, et al. "All-dielectric terahertz plasmonic metamaterial absorbers and high-sensitivity sensing." ACS omega 4.20 (2019): 18645-18652.

[95] Chen, H.-T., et al., A metamaterial solid-state terahertz phase modulator. Nature photonics, 2009. 3(3): p. 148-151.

[96] Savo, S., D. Shrekenhamer, and W.J. Padilla, Liquid crystal metamaterial absorber spatial light modulator for THz applications. Advanced Optical Materials, 2014. 2(3): p. 275-279.

[97] Bakır, M., et al., Microwave metamaterial absorber for sensing applications. Opto-Electronics Review, 2017. 25(4): p. 318-325.

[98] Hasan, D. and C. Lee, Hybrid metamaterial absorber platform for sensing of CO2 gas at Mid-IR. Advanced Science, 2018. 5(5): p. 1700581.

[99] Koenig, Swen, et al. "Wireless sub-THz communication system with high data rate." Nature photonics 7.12 (2013): 977-981.

[100] Rahm, Marco, Jiu-Sheng Li, and Willie J. Padilla. "THz wave modulators: a brief review on different modulation techniques." Journal of Infrared, Millimeter, and Terahertz Waves 34.1 (2013): 1-27.

[101] Nagatsuma, Tadao, Guillaume Ducournau, and Cyril C. Renaud. "Advances in terahertz communications accelerated by photonics." Nature Photonics 10.6 (2016): 371-379.

[102] Shen, Nian-Hai, et al. "Optically implemented broadband blueshift switch in the terahertz regime." Physical Review Letters 106.3 (2011): 037403.

[103] Ju, Long, et al. "Graphene plasmonics for tunable terahertz metamaterials." Nature nanotechnology 6.10 (2011): 630-634.

[104] Zhu, W. M., et al. "Microelectromechanical Maltese-cross metamaterial with tunable terahertz anisotropy." Nature communications 3.1 (2012): 1-6.

[105] Watts, Claire M., et al. "Terahertz compressive imaging with metamaterial spatial light modulators." Nature Photonics 8.8 (2014): 605-609.

[106] Zhu, J., et al., Ultra-broadband terahertz metamaterial absorber. Applied Physics Letters, 2014. 105(2): p. 021102.

[107] Wang, B.-X., et al., Six-band terahertz metamaterial absorber based on the combination of multiple-order responses of metallic patches in a dual-layer stacked resonance structure. Scientific reports, 2017. 7(1): p. 1-9.

[108] He, X., et al., Investigation of phonon scattering on the tunable mechanisms of terahertz graphene metamaterials. Nanomaterials, 2020. 10(1): p. 39.

[109] Xu, B.-z., et al., A novel structure for tunable terahertz absorber based on graphene. Optics express, 2013. 21(20): p. 23803-23811

[110] Ng, Binghao, et al. "Broadband terahertz sensing on spoof plasmon surfaces." Acs Photonics 1.10 (2014): 1059-1067.

[111] Huang, Yi, et al. "Terahertz plasmonic phase-jump manipulator for liquid sensing." Nanophotonics 9.9 (2020): 3011-3021.

[112] Ye, Longfang, et al. "Plasmonic waveguide with folded stubs for highly confined terahertz propagation and concentration." Optics Express 25.2 (2017): 898-906.

[113] Yuan, Mingrui, et al. "High-performance and compact broadband terahertz plasmonic waveguide intersection." Nanophotonics 8.10 (2019): 1811-1819.

[114] Wang, Zhihui, et al. "A Windmill-Shaped SSPP Waveguide for High-Efficiency Microwave and Terahertz Propagation." Electronics 11.9 (2022): 1293.

[115] Bowei Dong et al. “Recent progress in nanoplasmonics-based integrated optical micro/nano-systems.” J. Physics D: Applied Physics, vol. 53, 213001, 2020.

[116] Islam Maidul, et al. "Terahertz plasmonic waveguide based thin film sensor" Journal of Lightwave Technology 35.23 (2017): 5215-5221.

[117] Tian, Lili, et al. "Investigation of mechanism: spoof SPPs on periodically textured metal surface with pyramidal grooves." Scientific reports 6 (2016): 32008.

[118] Kumar, Gagan, et al. "Planar plasmonic terahertz waveguides based on periodically corrugated metal films." New Journal of Physics 13.3 (2011): 033024.

[119] Li, Shanshan, et al. "Terahertz surface plasmon polaritons on a semiconductor surface structured with periodic V-grooves." Optics express 21.6 (2013): 7041-7049.

[120] Sriram, S., and E. P. Supertzi. "Novel V-groove structures on silicon." Applied optics 24.12 (1985): 1784-1787.

[121] Kumar, Gagan, et al. "Terahertz surface plasmon waveguide based on a one-dimensional array of silicon pillars." New Journal of Physics 15.8 (2013): 085031.

[122] Pozar, David M. Microwave engineering. John Wiley & Sons, 2009.

[123] Agrawal, Amit, et al. "Terahertz transmission properties of quasiperiodic and aperiodic aperture arrays." JOSA B 24.9 (2007): 2545-2555.

[124] Agrawal, Amit, Z. Valy Vardeny, and Ajay Nahata. "Engineering the dielectric function of plasmonic lattices." Optics express 16.13 (2008): 9601-9613.

[125] Zhu, Wenqi, and Ajay Nahata. "Electric field vector characterization of terahertz surface plasmons." Optics express 15.9 (2007): 5616-5624.

[126] S. Zhang, D.A. Genov, Y. Wang, M. Liu, X. Zhang, Plasmon-induced transparency in metamaterials, Physical review letters 101(4) (2008) 047401.

[127] U. Fano, Effects of configuration interaction on intensities and phase shifts, Physical Review 124(6) (1961) 1866.

[128] Zhang, Xi-Cheng, and Jingzhou Xu. Introduction to THz wave photonics. Vol. 29. New York: Springer, 2010.

[129] Neu, Jens, and Charles A. Schmuttenmaer. "Tutorial: An introduction to terahertz time domain spectroscopy (THz-TDS)." Journal of Applied Physics 124.23 (2018): 231101.

[130] X. Xiao, J. Wu, F. Miyamaru, M. Zhang, S. Li, M.W. Takeda, W. Wen, P. Sheng, Fano effect of metamaterial resonance in terahertz extraordinary transmission, Applied Physics Letters 98(1) (2011) 011911.

[131] Z. Liao, S. Liu, H.F. Ma, C. Li, B. Jin, T.J. Cui, Electromagnetically induced transparency metamaterial based on spoof localized surface plasmons at terahertz frequencies, Scientific reports 6 (2016) 27596.

[132] P. Tassin, L. Zhang, R. Zhao, A. Jain, T. Koschny, C.M. Soukoulis, Electromagnetically induced transparency and absorption in metamaterials: the radiating two-oscillator model and its experimental confirmation, Physical review letters 109(18) (2012) 187401.

[133] F.-Y. Meng, Q. Wu, D. Erni, K. Wu, J.-C. Lee, Polarization-independent metamaterial analog of electromagnetically induced transparency for a refractive-index-based sensor, IEEE transactions on microwave theory and techniques 60(10) (2012) 3013-3022.

[134] X. Liu, J. Gu, R. Singh, Y. Ma, J. Zhu, Z. Tian, M. He, J. Han, W. Zhang, Electromagnetically induced transparency in terahertz plasmonic metamaterials via dual excitation pathways of the dark mode, Applied Physics Letters 100(13) (2012) 131101.

[135] X.-R. Jin, J. Park, H. Zheng, S. Lee, Y. Lee, J.Y. Rhee, K.W. Kim, H. Cheong, W.H. Jang, Highly-dispersive transparency at optical frequencies in planar metamaterials based on two-bright-mode coupling, Optics Express 19(22) (2011) 21652-21657.

[136] Q. Xu, S. Sandhu, M.L. Povinelli, J. Shakya, S. Fan, M. Lipson, Experimental realization of an on-chip all-optical analogue to electromagnetically induced transparency, Physical review letters 96(12) (2006) 123901.

[137] V. Yannopapas, E. Paspalakis, N.V. Vitanov, Electromagnetically induced transparency and slow light in an array of metallic nanoparticles, Physical Review B 80(3) (2009) 035104.

[138] Li, Hai-ming, and Feng Xue. "Tailoring polarization of electromagnetically induced transparency based on non-centrosymmetric metasurfaces." Physics Letters A 381.35 (2017): 3000-3004.

[139] Z. Bai, C. Hang, G. Huang, Classical analogs of double electromagnetically induced transparency, Optics Communications 291 (2013) 253-258.

[140] Zhu, Lei, et al. "Tunable electromagnetically induced transparency in hybrid graphene/all-dielectric metamaterial." Applied Physics A 123.3 (2017): 192.

[141] Zhu, Lei, et al. "Polarization-independent and angle-insensitive electromagnetically induced transparent (EIT) metamaterial based on bi-air-hole dielectric resonators." RSC advances 8.48 (2018): 27342-27348.

[142] Q. Xu, S. Sandhu, M. L. Povinelli, J. Shakya, S. Fan, and M. Lipson, "Experimental realization of an on-chip all-optical analogue to electromagnetically induced transparency," Phys. Rev. Lett. 96, 123901 (2006).

[143] W. Zhao, J. Qi, Y. Lu, R. Wang, Q. Zhang, H. Xiong, Y. Zhang, Q. Wu, J. Xu, On-chip plasmon-induced transparency in THz metamaterial on a LiNbO 3 subwavelength planar waveguide, Optics express 27(5) (2019) 7373-7383.

[144] Sriram, S., and E. P. Supertzi. "Novel V-groove structures on silicon." Applied optics 24.12 (1985): 1784-1787.

[145] Zhu, Wenqi, and Ajay Nahata. "Electric field vector characterization of terahertz surface plasmons." Optics express 15.9 (2007): 5616-5624.

[146] Chen D, Yang J, Zhang J, Huang J, Zhang Z. Section 1Tunable broadband terahertz absorbers based on multiple layers of graphene ribbons. Scientific reports 2017;7:1-8.

[147] Daraei OM, Goudarzi K, Bemani M. A tunable ultra-broadband terahertz absorber based on two layers of graphene ribbons. Optics & Laser Technology 2020;122:105853.

[148] Arsanjani A, Biabanifard M, Abrishamian MS. A novel analytical method for designing a multi-band, polarization-insensitive and wide angle graphene-based THz absorber. Superlattices and Microstructures 2019;128:157-69.

[149] Khavasi A. Design of ultra-broadband graphene absorber using circuit theory. JOSA B 2015;32:1941-6.

[150] Jiang, Yannan, et al. "Design and performance of a terahertz absorber based on patterned graphene." Optics letters 43.17 (2018): 4296-4299.

[151] Lin, Han, et al. "A 90-nm-thick graphene metamaterial for strong and extremely broadband absorption of unpolarized light." Nature Photonics 13.4 (2019): 270-276.

[152] Tasolamprou, Anna C., et al. "Experimental demonstration of ultrafast THz modulation in a graphene-based thin film absorber through negative photoinduced conductivity." ACS photonics 6.3 (2019): 720-727.

[153] Choy TC. Effective medium theory: principles and applications: Oxford University Press; 2015.

[154] Hecht E. Optics, 5e: Pearson Education India; 2002.

[155] Hecht E, Zajac A. Optics, chapter 9. Addison-Wesley 2002;3:384-441.

[156] Li H, Yu J. Bifunctional terahertz absorber with a tunable and switchable property between broadband and dual-band. Optics Express 2020;28:25225-37.

[157] Liu J, Chen W, Ma W-Z, Chen Y-S, Deng X-C, Zhuang P-P, et al. Biaxial hyperbolic metamaterial THz broadband absorber utilizing anisotropic two-dimensional materials. Results in Physics 2021;22:103818.

[158] Liu, Wenwen, and Zhengyong Song. "Terahertz absorption modulator with largely tunable bandwidth and intensity." Carbon 174 (2021): 617-624.

[159] Rahmanshahi, Mahdi, et al. "A tunable perfect THz metamaterial absorber with three absorption peaks based on nonstructured graphene." Plasmonics 16.5 (2021): 1665-1676.

[160] Rozanov, Konstantin N. "Ultimate thickness to bandwidth ratio of radar absorbers." IEEE Transactions on Antennas and Propagation 48.8 (2000): 1230-1234.

[161] Xu Z, Wu D, Liu Y, Liu C, Yu Z, Yu L, et al. Design of a tunable ultra-broadband terahertz absorber based on multiple layers of graphene ribbons. Nanoscale research letters 2018;13:1-8.

[162] Yang J, Zhu Z, Zhang J, Guo C, Xu W, Liu K, et al. Broadband terahertz absorber based on multi-band continuous plasmon resonances in geometrically gradient dielectric-loaded graphene plasmon structure. Scientific reports 2018;8:1-8.

[163] Cheng R, Zhou Y, Liu H, Liu J, Sun G, Zhou X, et al. Tunable graphene-based terahertz absorber via an external magnetic field. Optical Materials Express 2020;10:501-12.

[164] Wang T, Zhang Y, Zhang H, Cao M. Dual-controlled switchable broadband terahertz absorber based on a graphene-vanadium dioxide metamaterial. Optical Materials Express 2020;10:369-86.

[165] Feng H, Xu Z, Li K, Wang M, Xie W, Luo Q, et al. Tunable polarization-independent and angle-insensitive broadband terahertz absorber with graphene metamaterials. Optics Express 2021;29:7158-67.

[166] Nejat M, Nozhat N. Sensing and switching capabilities of a graphene-based perfect dual-band metamaterial absorber with analytical methods. JOSA B 2020;37:1359-66.

[167] Moradiani F, Seifouri M, Abedi K, Gharakhili FG. High extinction ratio all-optical modulator using a vanadium-dioxide integrated hybrid plasmonic waveguide. Plasmonics 2021;16:189-98.